Journal of Space Science and Technology

JSST

Vol.17, Special Issue, 2024

Print ISSN: 2008-4560
Online ISSN: 2423-4516

JSST
Journal of Space Science and Technology

Journal of
Space Science and Technology

Vol. 17, Special Issue, 2024

Indexed in:
DOAJ, ISC, EBSCO, …

Publisher: IAS

Director-in-Charge: M. Navabi, PhD.
Editor-in-Chief: R. Ebrahimi, PhD.
Deputy Editor: M. Azimi, PhD

Address: No. 1, Mohandes St., Darya Blv.
Tehran, I.R. Iran

Tel: +98(21) 88366030
Website: https://jsstpub.com
E-Mail: jsst@jsstpub.com
International E-Mail: info1@jsstpub.com

Print ISSN: 2008 - 4560 **Online ISSN: 2423 - 4516**

Table of Contents

JSST
Journal of Space Science and Technology

P-ISSN: 2008-4560
E-ISSN: 2423-4516

Journal of Space Science and Technology

Vol. 17, Special Issue, pp. 1-14, 2024
https://doi.org/10.22034/jsst.2024.1478
Journal Homepage: https://jsstpub.com

Review Paper

Research Trends in Utilizing Artificial Intelligence in Satellite-Based Internet of Things: A Scientometric Analysis

Pedram Hajipour[1*], Hassan Yeganeh[2], Hossein Eftekhari[3], and Houman Zarrabi[4]

1,4. Satellite Communication Group, Faculty of Communications Technology, ICT Research Institute, Tehran, Iran
2. Faculty of Communications Technology, ICT Research Institute, Tehran, Iran
3. Science and Technology Watch Company, Tehran, Iran

ARTICLE INFO

Article History:

Received 22 February 2024
Revised 19 April 2024
Accepted 01 May 2024
Available Online 01 June 2024

Keywords:

Scientometrics
Internet of things
Artificial intelligence
Satellite-based
Communication technologies

ABSTRACT

Today, according to the development of satellite-based hybrid networks that are able to provide diverse and new services to most parts of the planet, the designers of such networks are encouraged to use new communication technologies such as the Internet of Things and artificial intelligence to improve the performance of such classes of networks. In this article, using scientometric tools, the status of scientific publications in the field of "utilizing AI in satellite-based IoT" has been investigated. For this purpose, more than 475 research documents published from 2013 to 2023 have been extracted from the Scopus database and accordingly evaluated and analyzed using software tools such as Bibexcel and VOSviewer. Based on the statistical results, China, India and North America are among the top performing countries in this field. In addition, based on our findings, the schemes namely machine learning, deep learning, reinforcement learning, neural networks and convolutional neural networks have been used the most, in this research domain.

*Corresponding Author's E-mail: hajipour@itrc.ac.ir

How to Cite this Article:
P. Hajipour, H. Yeganeh, H. Eftekhari, and H. Zarrabi, "Research trends in utilizing artificial intelligence in satellite-based internet of things: A scientometric analysis," *Journal of Space Science and Technology*, Vol. 17, Special Issue, pp. 1-14, 2024, https://doi.org/10.22034/jsst.2024.1478.

1. INTRODUCTION

The rapid proliferation of satellite technology and the advance of the Internet of things (IoT) have laid the groundwork for an interconnected world, where satellites act as pivotal facilitators for seamless communication and data exchange.

Deploying IoT devices in remote and inaccessible areas is often challenging due to limited infrastructure. Satellite-based IoT addresses this challenge by providing ubiquitous connectivity, enabling real-time data transmission across diverse environments.

Artificial Intelligence (AI), with its ability to process vast volumes of data and extract meaningful patterns, emerges as a critical enabler in enhancing the efficiency and effectiveness of satellite-based IoT systems.

Machine learning (ML) algorithms empower such systems to analyze and interpret data and optimize decisions for applications in precision agriculture, environmental monitoring, and disaster response.

Researchers such as in [1], emphasize the high potential of using deep neural networks (DNN) in handling complex data representations, aligning with the requirements of diverse satellite-based IoT applications. In [2], provide foundational insights into the principles of AI, laying the theoretical groundwork for its application in the context of satellite-based IoT.

As the synergy between AI and satellite-based IoT gains momentum, it becomes imperative to assess the current state of research and identify emerging trends. S.Bi and et.al in [3], examine three broad approaches including intelligent services, brilliant stability, and smart security in communication networks that use these two types of technology.

Today, due to satellite-based communication networks that are able to cover many people in different regions of the globe, it has become possible to expand communication networks based on IoT technology. The development process of its communication protocols has always faced a challenge that has been addressed in reference [4].

In addition, in order to create scalability in this type of communication network, it is recommended to use deep learning (DL) algorithms. In addition, the combination of two AI technologies and the IoT in satellite-based communication networks adds two special characteristics to the communication network. In such a way; AI leads to the ability of devices to learn, while IoT will lead to the interaction of devices with each other using the Internet. Of course, challenges such as the creation of space debris and their collision with each other are discussed in [5].

In [6], a solution has been proposed that improves the communication quality in a satellite network based on extended extreme learning machine (ELM) algorithms. To use this type of algorithm, IoT sensors have also been used to collect weather data. Notable contributions by scholars like [7] have significantly influenced the development of AI methodologies, fostering their integration into satellite-based IoT frameworks. Concurrently, research papers such as [8-11] offer a comprehensive survey of the existing literature, highlighting the evolving landscape and identifying gaps that warrant further investigation.

As the main contribution of our work, this paper aims to conduct a scientometric analysis to systematically review and synthesize the existing literature on the integration of AI in satellite-based IoT. By employing quantitative and qualitative methods, we seek to identify influential research clusters, key contributors, and evolving thematic trends.

Through this analysis, we aim to contribute to a deeper understanding of the intellectual landscape, offering insights that can guide future research directions and inform policy decisions. Therefore, the convergence of AI and satellite-based IoT presents a fertile ground for future innovations and explorations. This scientometric analysis sheds light on the intricate web of research endeavors in this domain, offering a nuanced understanding of the current state of knowledge and paving the way for future advancements in this transformative intersection of technology.

Scientometric analysis offers a systematic approach to mapping the intellectual structure of this multidisciplinary field, providing a comprehensive overview of research patterns, influential authors, and key thematic areas. Scientometrics is a tool that can measure some of the most important indicators of any research field, such as the trend of published scientific productions, leading countries, leading authors, leading institutions and universities and the frequency of key words or scientific concepts in a specific subject. In addition software tools such as

VOS viewer and Bibexcel can draw some relational networks such as co-words, co-countries, co-authorships and density of the used words.

In addition, it is possible to outline the way of cooperation between the leading countries in the field [8-10].

The rest of this paper is organized as follows. Section 2 describes the research background, data sources and methods used for the scientometric analysis. Section 3 presents the employed research methodologies. Section 4 presents the results and discussions of the given analysis, including publication trends, research networks, and research topics. Section 5 concludes the paper and recommends possible future research directions.

2. RESEARCH BACKGROUND

Due to the fact that in this domain, no scientometric work has been specifically examined or published, this idea has been thoroughly discussed in this article. The concept of IoT refers to objects that communicate and share data without human intervention.

Today, with the introduction of the concept of smart urban development based on the IoT, the need to create systems with the ability to measure and process processes automatically is felt more than in the past. In this regard, a scientific analysis from 2012 to 2021 based on the SCOPUS database has been presented in [12], all kinds of smart solutions for farmers and other influential factors investigated. The results of this research show that China, India and South Korea are the leading countries. The most scientific productions are presented in the form of conference articles by 49.6 % and magazines by 33.1%, and the fields of computer science and engineering have the highest share in this field with the frequency of 30.4% and 24.6%, respectively. Prieto, J. is also the best author in this field of knowledge.

In [13], studies the impact of IoT technology based scientometrics in countries in East Asia are covered. Based on the method required in scientometrics, the period from 2016 to 2020 was selected based on the Scopus database. The results obtained in this field indicate that China is ahead. In addition, concepts such as smart factories, machine learning and smart cities were prioritized in this research field in terms of frequency. Electronics journal (Switzerland) in this field is leading in terms of the number of published related research topics.

One of the technologies required to improve data exchange in the field of IoT is the use of the semantic web, which has received serious attention today. In this regard, the review and analysis of this field of knowledge based on scientometrics based on the Web of Science database has been investigated and analyzed in the reference. The results of this analysis in the period from 2011 to 2020 indicate that China, America and Spain are the leading countries. Most research productions in this field are related to computer science with 477 research documents, engineering with 325 research documents and telecommunication with 203 research documents. The top author in this field is Blanco-F,Y. with 17 research articles. The two top universities in this field from the point of view of scientific production are University of Vigo and Campus University from Spain [14].

With the introduction of IoT technology in the fourth industrial revolution, the possibility of interaction and knowledge sharing between humans and objects became possible [15]. One of the types of objects in this field is smart appliances that lead to the creation of smart cities. Research based on scientometrics in the field of using IoT and smart cities based on the Web of Science (WoS) database has been conducted from 2011 to 2021 [16].

In this research, few research papers have focused on both IoT and smart cities. Visualization of Similarities viewer (VOSviewer) software is used in the mentioned reference. The trend of published documents shows that the most scientific productions were produced in 2020. In addition, in the mentioned article, the countries and authors who published the most documents were analyzed.

In [17] with using scientometrics analysis, the effects of the emergence of IoT technology in a wide range of objects, processes and environments with living or non-living elements investigated. This study focuses on the scientific map of the IoT based on the Web of Science (WoS) database from 1989 to 2019. In this analysis, 14469 research documents were processed and evaluated using VOSviewer software.

The main focus of this research document is on authors, countries, journals, institutions, etc. The analysis shows that Joel J.P.C Rodrigues was the most prolific author, China was the most prolific

country, IEEE Access was the most influential journal, and Luigi Atzori was the most cited author. The main keywords that were more frequent in the documents were IoT, internet and security, respectively. In another study, using scientometrics, the evolution of blockchain technology is investigated for decision-making processes in the fields related to the IoT and ML.

As presented in [18], blockchain technology can store data and prevent them from being hacked or edited. In this research, the SCOPUS database is used from 2015 to 2023, and 1332 articles is retrieved in the field of digital currency based on blockchain-enabled IoT. The analyses presented in this research show that America is the leading country in this field, wherein the scientific productions are pulished in 2018. Based on this paper, IEEE Access has the most scientific productions in this research field.

Another study in the field of scientometrics refers to the concept of resource management in IoT networks, as described in [19]. In this research, a comprehensive review of research documents between 2012 and 2022 has been conducted using the SCOPUS database to determine the current status of the mentioned field and examine the challenges and opportunities of research in this field. The results of these surveys showed that limited resources will make it challenging to create networks based on the IoT. The results of the analysis show conventional methods such as AI, optimization methods, and game theory approaches are widely used in this field. Of course, in this research, one of the standard methods of AI called DL is also investigated, which will be one of the solutions for allocating resources with low complexity in real time.

In [20], the importance of IoT technology in an Arab countries such as Algeria, Bahrain, Comoro and so on were investigated. For this purpose, the Scopus database was used between 2010 and 2017. The most scientific productions in this field related to 2017 are 607 research documents and the highest amount of referencing is 2002 in 2017. Leading countries in this field are Saudi Arabia, the United Arab Emirates and Tunisia. The top two authors in this field in the names of Jararweh, y. and Al-Ayyoub, M. are from the Jordan University of Science and Technology. Two IEEE Access and Computer Networks journals are the leading journals in the scientific productions of this field. Three fields of computer science, engineering and mathematics are leading in this field.

In [21], the application of IoT technology to the executive management based on scientometrics is investigated using two databases including SCOPUS and WOS from 2010 to 2022. As a result of this research, 1623 published research documents were examined. The study results in the synonym network show frequent topics such as digitization, digital operation, monitoring systems, tracking and intelligence. The leading countries in this field were China, America, and India. The leading journal in this field is IEEE Access. The most cited article domain has 1041 references. Nowadays, the creation of a smart city has been seriously deployed by developed and developing countries. One type of technology that can be used in modern smart cities is the IoT.

In this regard, in the reference research [22], which is based on scientometrics, research documents were reviewed from 2012 to 2021 based on WoS, SCOPUS, and IEEE Xplore databases, and approximately 1019 documents were found. The research results show five frequently used words including IoT, IoT architecture, energy, security and privacy. In addition, the leading countries in this field include India, America, and China. The leading research institute in this field is the National Institute of Technology Nit System. The IEEE IoT journal published most of the documents in this field. Zaslavsky is the best author in this field who has published the most research documents. The article "Internet of Things for Smart Cities" published in the IEEE Internet of Things journal has the most references in the three WoS databases with 2170 references, SCOPUS with 2940 references, and IEEE Xplore with 2694 references.

In [23], wireless transmission methods in the IoT based on scientometrics are investigated. This statistical analysis method was performed based on the WoS database. The results of this evaluation were based on 15102 authors from 3843 organizations in 87 countries, including China, the United States, South Korea, and India, and 6105 articles in 551 publications. The analysis results show that in terms of quantity, China is the most powerful country in the world, which published 1912 articles and accounted for approximately 31.3% of the total number of articles published in this field. In addition, seven Chinese organizations are among the top 10 organizations, and some Chinese researchers have

published articles with high citation frequency in the fields of machinery, computer science, and telecommunications. IoT technology includes devices with limited resources regarding battery power, processing capacity, memory, bandwidth, etc. One of the processes carried out in low-power and low-loss communication networks based on IoT.

In [24], the protocols used from the aspects of reliability, robustness, energy efficiency, and flexibility in low-power and low-loss communication networks based on scientometrics are investigated. For this purpose, the results of the research from 2010 to 2021 are conducted on the use cases of this field, and intelligent networks, smart cities, and smart homes are the most commonly used ones in this field. Today, the challenges of city creation and migration to cities have drawn attention to the sustainable management of land and water resources for productivity in modern agriculture based on the combination of AI and IoT technologies.

In [25], research based on scientometrics in the field of water and land management with the help of AI and IoT is presented. The results of this analysis are based on 436 research articles between 1991 and 2021. The most frequent words include artificial neural networks (ANN), adaptive neural fuzzy inference systems (ANFIS), support vector regression (SVR), random forest (RF), and multilayer perceptron networks artificial neural network (MLP-ANN). In addition, the countries of China, India, Iran, Australia, and the United States of America were recognized as pioneers in this field. While the countries of Italy, Spain, and Saudi Arabia, considered as emerging countries but with low cooperation links, started their initial activities in this field.

In another research, the importance of using IoT in the field of health based on scientometrics is mentioned [26]. In this research, 778 research articles from the WoS database were reviewed from 1998 to 2016. Based on the results obtained, the growth of scientific production in this field has accelerated since 2010. The most important topic of interest in this field is systems and services design and implementation, and people with scientific affiliations from China, America, and England had the most scientific productions.

In another study, as in [27], the situation of using IoT technology between China and the United States based on scientometrics from 2009 to 2018 has been investigated. The results of the analysis show that although China has more research publications in this field but China should try to develop basic and essential technologies based on property rights for more effective competition.

In another study, the role of IoT technology in the field of wireless sensor networks is investigated. For this purpose, between 2002 and 2016, 19035 published documents in WoS and SCOPUS databases were analyzed. In this regard, a software package based on the Python program named ScientoPy was used to analyze the data extracted from the research documents. The results of the analysis show that the countries of China, America and India had the largest share in the publications of this field with 1561, 4822 and 1089 published documents, respectively, based on the affiliation of the authors declared in the documents. In 2016, an author named Y. Zhang was the leader in this field with more than 35 published documents. Of course, an author named L. Atzori from Italy had the highest number of references (3239 reference), in the publication of his research activity in the computer network magazine in 2010.

The most frequent keywords in the articles in this field in 2016 indicated the abundance of wireless sensor networks, cloud computing, and security. In addition, the three most frequent applications in 2016 included smart city, smart home and intelligent network, respectively. The most frequent communication protocol in this field is for the Radio Frequency Identification (RFID) host layer and the Constrained Application Protocol (CoAP) medium layer in 2016 [28].

The most frequent processing methods in this field are ML, data mining and complex event processing. One of the areas where IoT technology can improve its management and services is food security. For this purpose, in the research conducted in [29], the effect of IoT technology on this area, based on scientometrics was investigated. In this research, which was conducted between 2011 and 2018, three databases including SCOPUS (41 related research documents), Science Direct (1 related research document), and Google Scholar (48 related research documents) were used. The top authors of this field of knowledge are L. Zheng, Y. Zhang, J. Wang and W. Han, respectively.

A significant part of the studies and research conducted in this field by Chinese universities is to monitor food products and product quality. The most widely used communication technologies in this field were RFID and wireless sensor

networks. Nowadays, the use of AI techniques such as ML for global navigation satellite systems (GNSS) based on IoT to monitor and predict the ionosphere layer, which leads to cost reduction-, is receiving serious attention. In [30], a ground navigation system based on machine-to-machine (M2M) communication is proposed, which can provide navigation information and services required by users.

In [31], the authors focused on providing an educational framework based on federated learning (FL) in IoT edge computing, which can be used to manage natural resources such as forest areas. The proposed method can reduce the time required for data processing in the system by increasing privacy.

3. RESEARCH METHODOLOGY

The results presented in this article include a review of documents (including articles published in journals, conference articles, books, reports, etc.) published worldwide in the field of AI in satellite-based IoT using scientometric tools.

For this purpose, it is necessary to extract published documents in this domain and perform relevant analysis. As for the first step, in the SCOPUS citation database, the domain was searched as follows:

(TITLE-ABS-KEY ("Satellite" AND ("internet of thing*" OR "IOT")) AND TITLE-ABS-KEY (("Artificial Intelligence" OR "Neuro scale algorithm" OR "weighted fuzzy scoring" OR "support vector machine" OR "Pattern Recognition" OR "Machine Learning" OR "Machine Vision" OR "Image Processing" OR "Data mining" OR "Fuzzy Reasoning" OR "Deep learning" OR "Fuzzy Inference Systems" OR "Genetic algorithm*" OR "Evolutionary Algorithm*" OR "Random Forest" OR "Decision tree" OR "Neural network*" OR "k-nearest neighbors algorithm*" OR "Federated Learning" OR "Reinforcement Learning" OR "Soft computing" OR "Unsupervised learning" OR "SVM-based spectrum sensing" OR "Markov model" OR "Extreme learning machine" OR "Neural Turing machine" OR "Generative Learning" OR "Deep Convolutional Network" OR "fuzzy logic" OR "fuzzy system*" OR "supervised learning" OR " statistical learning")) AND NOT TITLE-ABS-KEY ("IOT (In-Orbit Test)").

The search strategy was carried out in the title, abstract and keywords of the documents indexed in the Scopus database. The number of results obtained on 2023.12.10 equals 475 documents (including articles, books, etc.). The documents were downloaded in the RIS format.

In the second step, Excel and Bibexcel software were used to create the co-occurrence matrices (for Co-words network and Co-country network). Before creating of co-occurrence matrices, the necessary actions were taken to remove unrelated and meaningless keywords, and the singular and plural words were also standardized. However, according to experts, words that were conceptually synonymous were also merged into one word. The threshold limit considered in Bibexcel software for the frequency of words in the documents was set as 3. Finally, using the VOSviewer software, this area was visualized.

4. RESEARCH FINDINGS

The number of published documents worldwide and the number of citations for published documents versus year in this domain field and its trends are shown in Figure 1 and Figure 2, respectively. As can be seen in the Figure 1, the scientific growth of this domain field from the year 2018 with the total publications of 18 research documents increased significantly compared to the beginning in 2013.

The number of published documents worldwide in 2023 has not been finalized yet. Also, most citation published documents are 2633 for 2023. The status of the types of published documents (conference articles, journal articles, books, book chapters, etc.) in this field is shown in Figure 3.

As it depicts, the total articles published during 2013-2023 with the value of 42% has the highest weight among the published documents, and, book chapters with about 7% has the lowest weight in the total number of publications. The authors, with the highest number of published documents, are also shown in Table 1.

In Table 1, TP is the total papers in the SCOPUS database wherein TC is the total number of citations for each publications and CPP is the total number of received citations count divided by the total number of publications in the SCOPUS database. In addition, the top journals of the world, which have the most scientific productions in this field, are listed in Table 2.

The frequency of the type of AI mechanism used is presented in Table 3. The ranking status of the countries with the most degrees published is also shown in Figure 4. As it is observed, the countries of China, India and America are at the top of this ranking. The status and the total number of published documents in different subject areas are shown in Fig. 5.

As it is apparent in the above figure, the fields of "Computer Science" and "Engineering" have the highest number of documents in this field. The collaboration network of the top authors in this field is shown in Fig. 6.

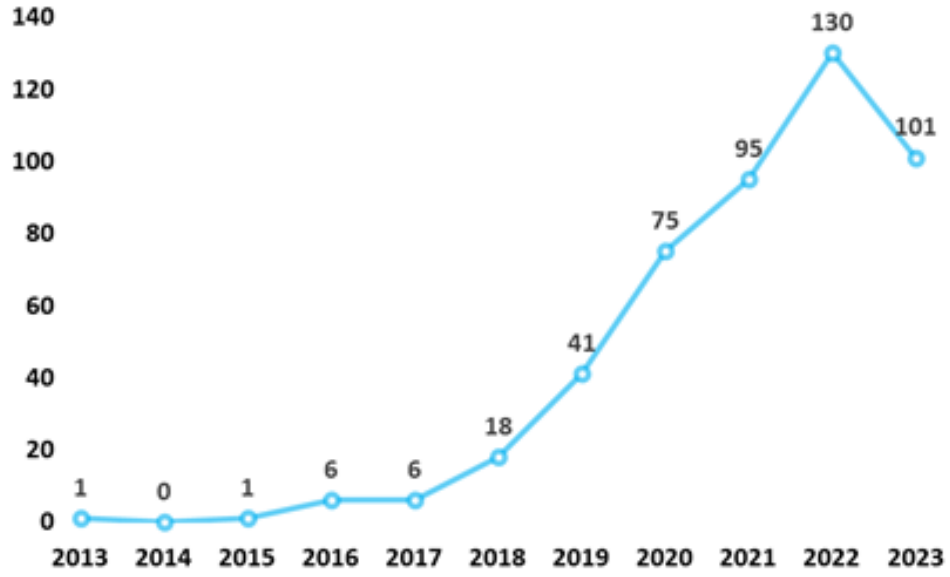

Fig. 1. Number of published documents in the field of "utilizing AI in satellite-based IoT".

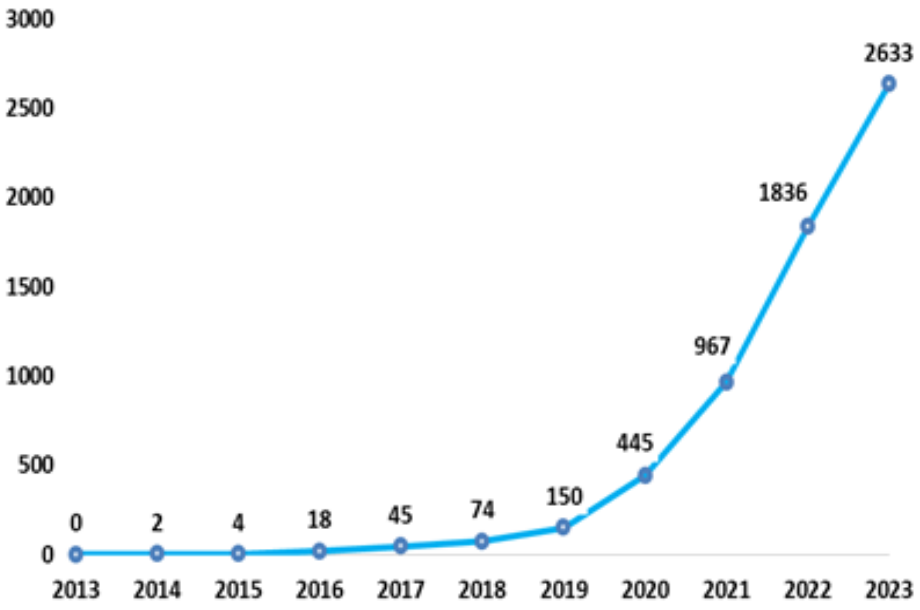

Fig. 2. Number of citations for published documents in "utilizing AI in satellite-based IoT".

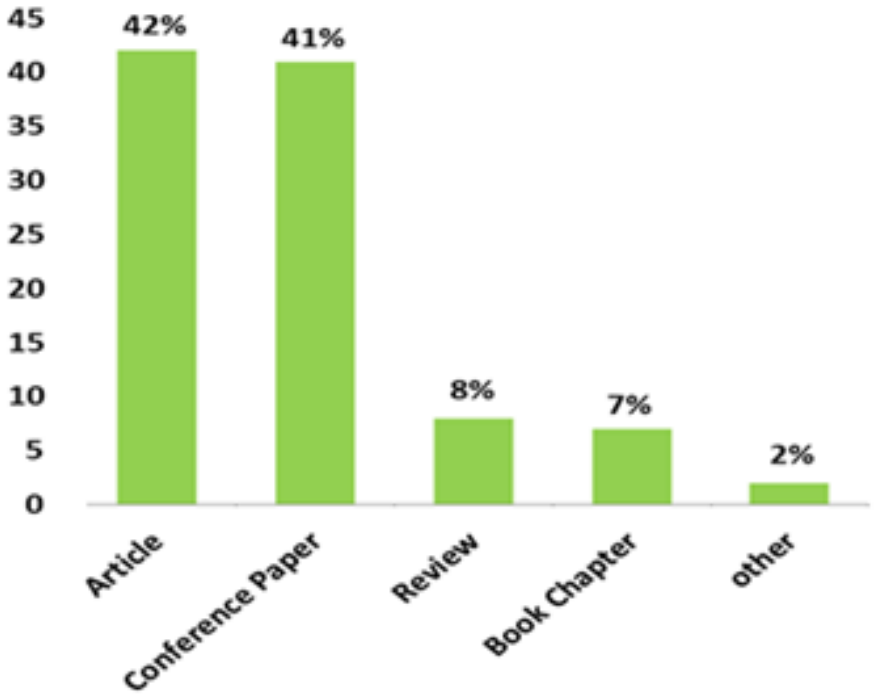

Fig. 3. The types of published documents in "utilizing AI in satellite-based IoT".

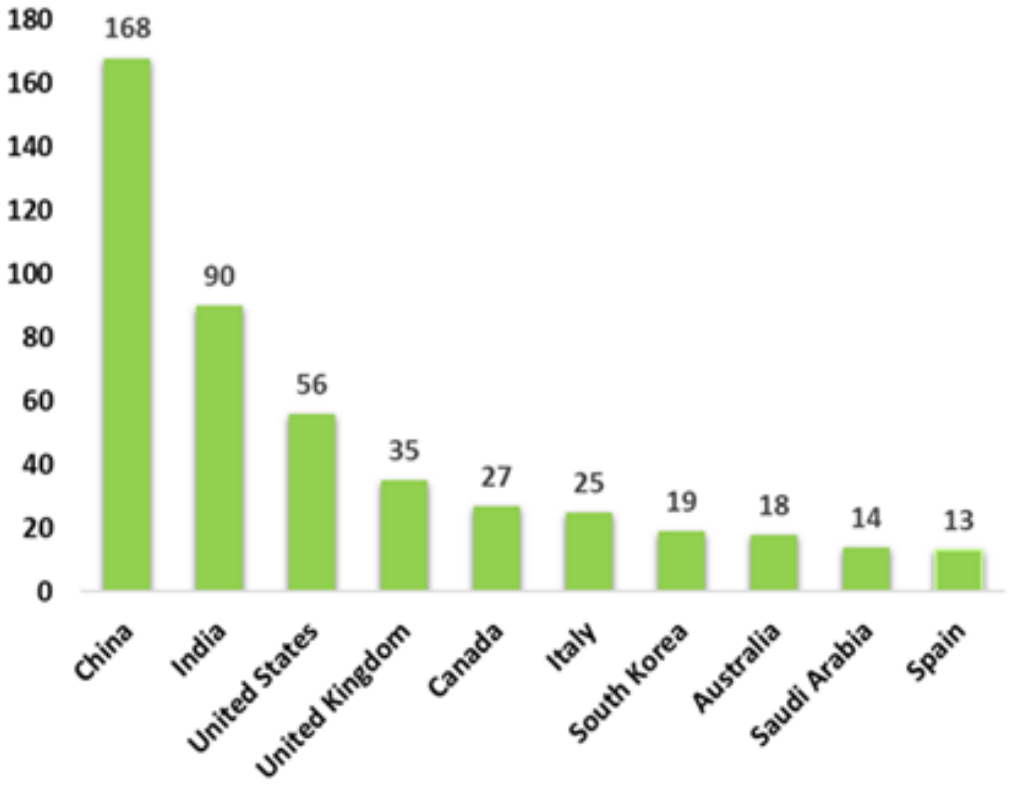

Fig. 4. Leading countries in the field of "utilizing AI in satellite-based IoT".

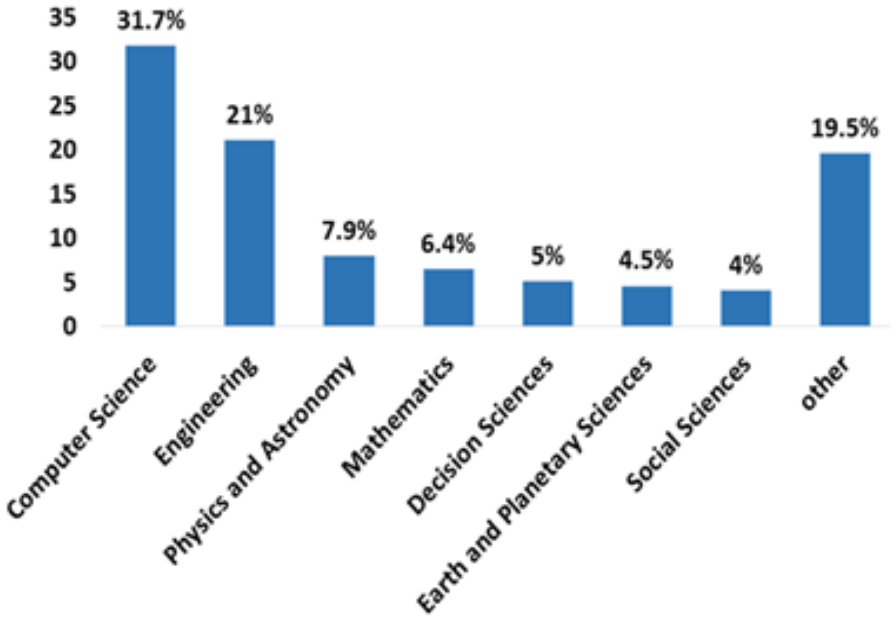

Fig. 5. The percentage of published documents in different subject areas in "utilizing AI in satellite-based IoT".

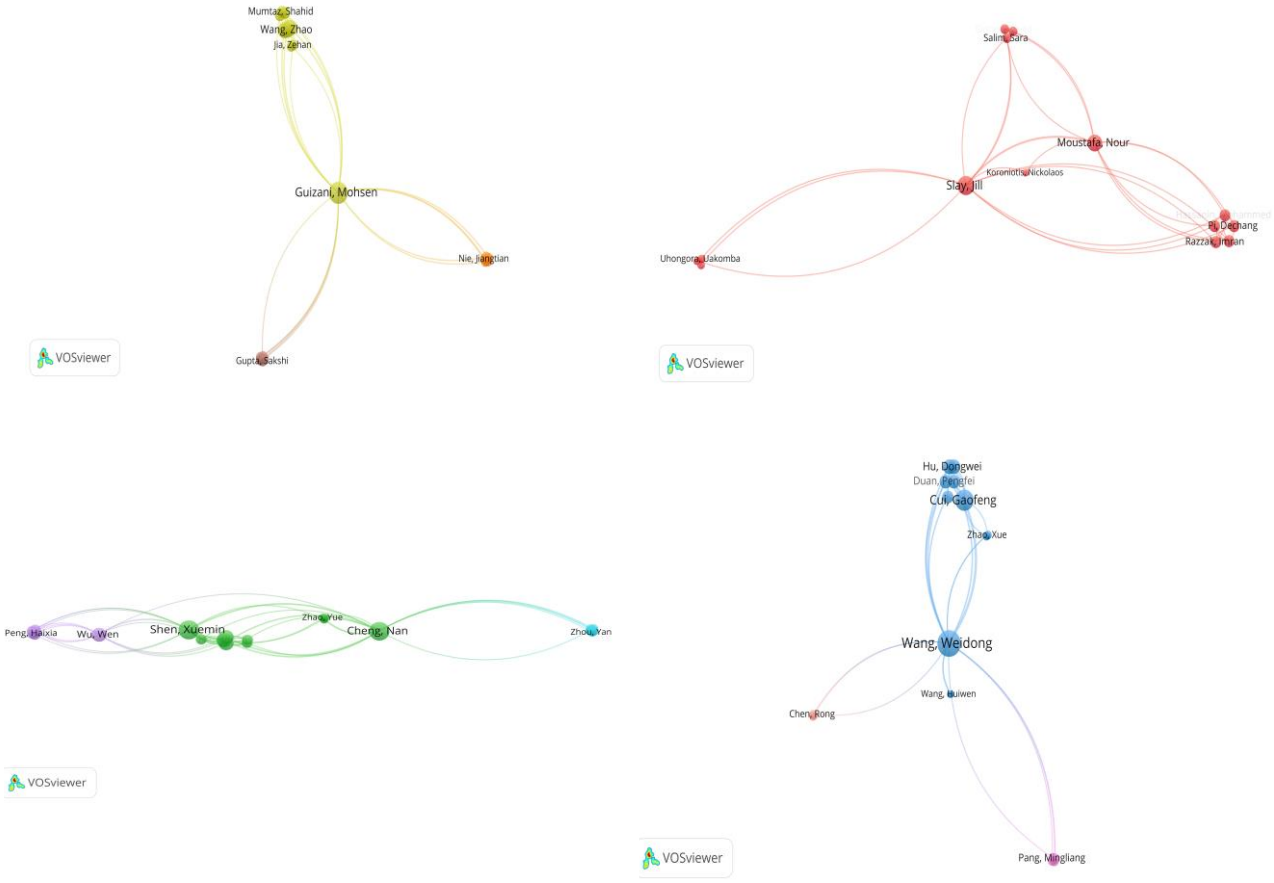

Fig. 6. Co-authorship network based on table 1 in the field of "utilizing AI in satellite-based IoT".

Table 1. Top authors in "utilizing AI in satellite-based IoT".

Author name	TP	TC	CPP
Wang, W.	8	121	15.13
Cui, G.	5	98	19.6
Shen, X.	4	654	163.5
Cheng, N.	4	654	163.5
Guizani, M.	4	139	34.75
Slay, J.	4	11	2.75

Table 2. Top journals on "utilizing AI in satellite-based IoT".

Source Title	Count
IEEE Internet of Things Journal	27
IEEE Access	12
MDPI Sensors	11
MDPI Electronics	7
Proceedings of The International Astronautical Congress	7
ACM International Conference Proceeding Series	7

Table 3. Frequency of "AI algorithms in satellite-based IoT".

Keyword	The frequency of use
Machine Learning (ML)	115
Deep Learning (DL)	99
Reinforcement Learning (RL)	45
Neural Networks (NN)	25
Convolutional Neural Network (CNN)	18

Consequently, to outline the knowledge structure of this research domain, by using the outputs from the "SCOPUS" database and the Bibexcel software, the analysis of the relevant words throughout the documents was initially performed. In this section, the words in the extracted documents and the most relevant words have been selected to present on the network.

This process causes the words that are less important to be removed and lets the network focus only on the major words. In the next step, the output obtained from the Bibexcel software is fed to the VOSviewer software. The results based on this process is given in Fig. 7.

The size of the circles in Figure 8 indicates the total count of the word. As it is evident in this figure, the words "IoT", "ML", "Satellites", "DL", and "AI" with 326, 115, 112, 99 and 96 usage frequencies, have the highest count in the total published documents. In this map, each of the used colors represents a topic cluster. As it is observed, the target words are classified into seven clusters.

The density network is shown in Figure 8. In this figure, the highest density of words in the network is shown in red. In the same way, yellow, green and blue ones have the highest density. The distance of the words also has meanings. For example, if the distance between two words is relatively small, it can be inferred that they are used mainly together in many documents. Also, if the distance between two words is considerable, these two words are used together in few documents.

Moreover, the state of communication and international scientific cooperation between the countries is shown in Figure 9. As shown in this figure, 64 countries have international scientific cooperation in this field, among which China, United Kingdom and America have the highest cooperation. Examining the co-occurrence map of the vocabulary of this field shows that there are seven major topic clusters. Cluster one has sixty-five words including AI, big data and information management. In the second cluster with sixty-three words, there are terms like IoT, ML and remote sensing.

The third cluster with fifty-one words includes satellites, orbits and satellite communication systems. In the fourth cluster, there are fifty words including global positioning system, global satellite navigation system. The fifth cluster includes things like DL, antennas and RL with forty-four words. The sixth cluster with thirty words includes things like learning systems, network security and forecasting.

Finally, the seventh cluster with twenty-three words contains data communication system, spatial lights and car-to-car communication. In Table 4, according to the output of the VOSviewer software, a total of 7 subject clusters have been extracted. In this table, one column refers to the main topic of each cluster and other research priority topics in the subset of this cluster.

5. CONCLUSIONS

There are various methods to study, analyze and classify the specifications and characteristics of a research field. In this article, we performed this using scientometric analysis in the investigation of "Using AI in satellite-based IoT".

In addition, the relationship between its thematic sub-areas and international cooperation was deduced. The review of retrieved publications in this field until 2023 showed 475 documents indexed in the SCOPUS database.

The major growth in the total number of publications in this field in recent years, shows the importance and practicality of this field technology. According to the results deduced from this study, China, India and North America are the leading countries in the research of this domain filed at the global level. Also, based on our findings, the terms including machine learning, deep learning, reinforcement learning, neural networks and convolutional neural networks have been used the most in this domain. Wang, W. has the most number of articles in the obtained results with eight published papers. With 27 published articles, IEEE Internet of Things Journal is the most chosen magazine in this research field. Computer science has the most research activity in this field with a share of 31.7%.

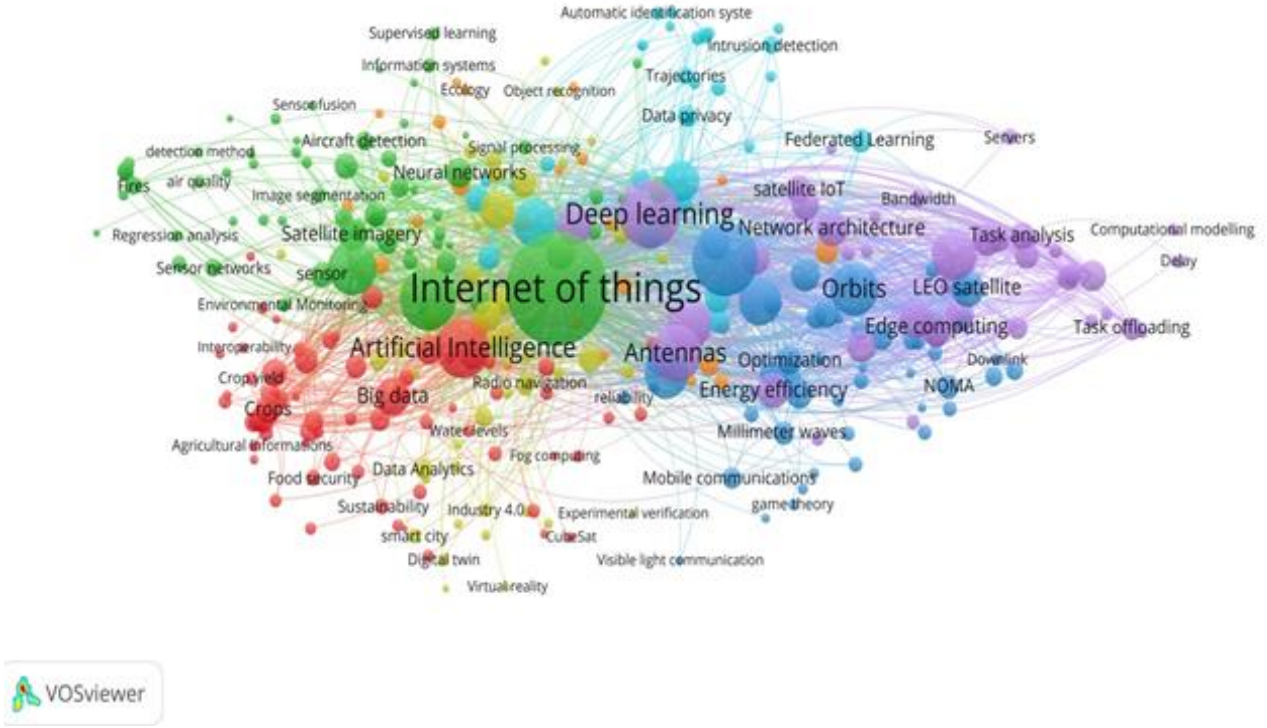

Fig. 7. Co-words network in the field of "utilizing AI in satellite-based IoT".

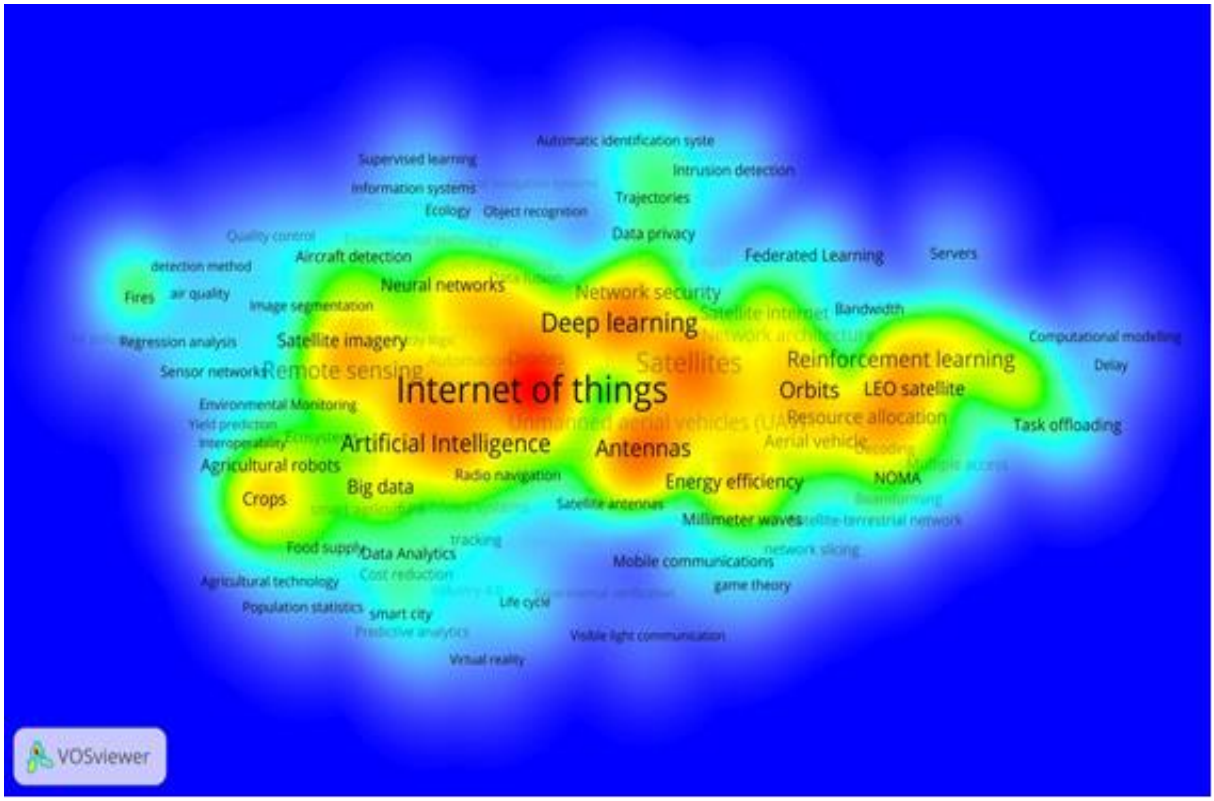

Fig. 8. Density network in the field of "utilizing AI in satellite-based IoT".

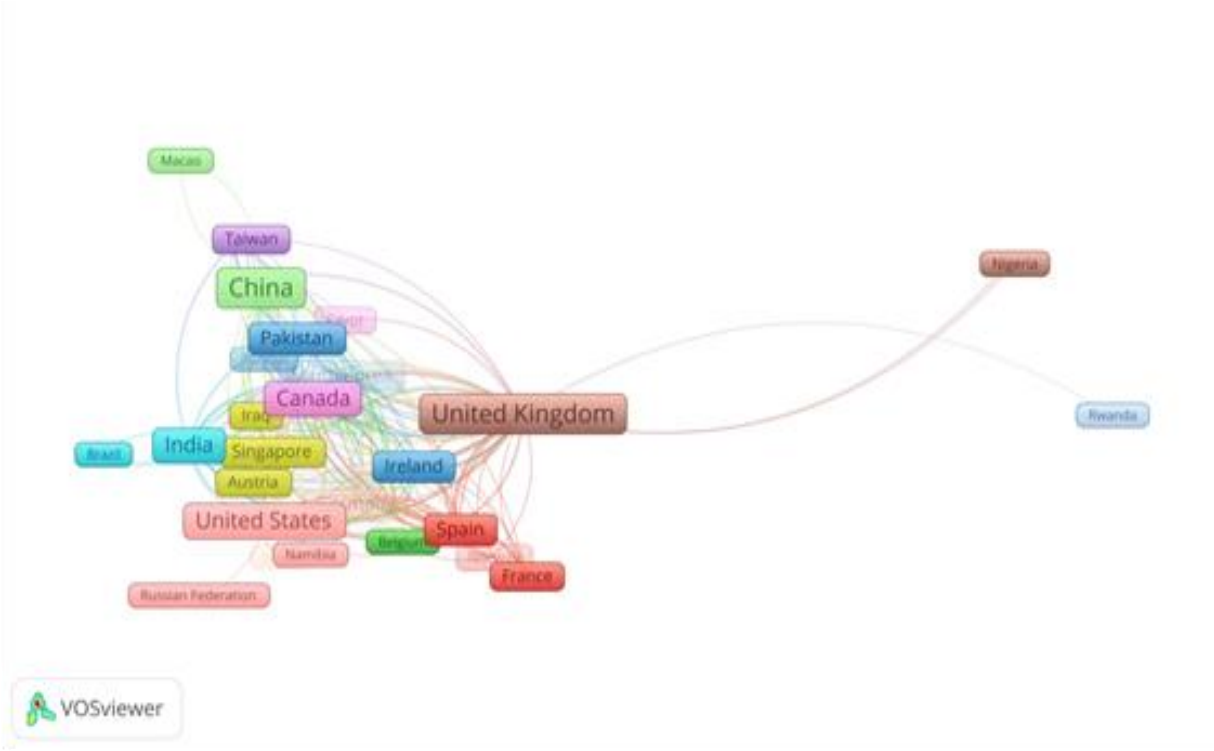

Fig. 9. International scientific cooperation among countries in "utilizing AI in satellite-based IoT".

Table 4. Classification of existing clusters in the field of "utilizing AI in satellite-based IoT" until 2023 (according to Fig.7).

number of clusters	Major issues for each cluster	Some major related topics clusters by frequency
1	Intelligence management	Artificial Intelligence, Big Data and Information Management
2	Intelligence monitoring	Remote sensing, Satellite Imagery and Satellite Remote Sensing
3	Satellite communication	Satellites, Orbits and LEO Satellite
4	Navigation systems	Global Navigation Satellite Systems and Radio Navigation
5	Resource management	Resource Allocation, Energy Efficiency and Convex Optimization
6	Security	Network Security, Cybersecurity and Data Privacy
7	Communication systems	Vehicle to Vehicle Communications, Cellular Network and Space Platforms

CONFLICT OF INTERESTS

No conflict of interest has been expressed by the authors.

REFERENCES

[1] I. Goodfellow , Y. Bengio, and A. Courville, *Deep Learning*, MIT Press, 2016.

[2] S. J. Russell and P. Norvig, *Artificial Intelligence: A Modern Approach*, 3rd ed. Pearson, 2016.

[3] S. Bi *et al.*, "A survey on artificial intelligence aided internet-of-things technologies in emerging smart libraries," *Sensors*, vol. 22, no. 8, 2022, Art. no. 2991, https://doi.org/10.3390/s22082991.

[4] Ju. H. Leel, D. P. Selvam, A. F. Molisch, and J. Kim, "Reinforcement learning empowered massive IoT access in LEO-based non-terrestrial networks," in *13th International Conference on Information and Communication Technology Convergence (ICTC)*, Jeju Island, Korea, 2022, pp. 1347-1350, https://doi.org/10.1109/ICTC55196.2022.9952919.

[5] F. Massimi, P. Ferrara, and F. Benedetto, "Deep learning methods for space situational awareness in mega-constellations satellite-based internet of things networks," *Sensors*, vol. 23, no. 1, 2022, Art. no. 124, https://doi.org/10.3390/s23010124.

[6] X. Yuan, J. Liu, H. Du, Y. Zhang, F. Li, and M. Kadoch, "Machine learning-based satellite routing for SAGIN IoT networks," *Electronics*, vol. 11, no. 6, 2022, Art. no. 862, https://doi.org/10.3390/electronics11060862.

[7] C. M. Bishop, *Pattern Recognition and Machine Learning*, 1st ed. New York: Springer, 2006.

[8] A. K. Shukla, M. Janmaijaya, A. A. Abraham, and P. K. Muhuri, "Engineering applications of artificial intelligence: A bibliometric analysis of 30 years (1988–2018)," *Engineering Applications of Artificial Intelligence*, vol. 85, pp. 517-532, 2019, https://doi.org/10.1016/j.engappai.2019.06.010.

[9] M. C. Kim and C. Chen, "A scientometric review of emerging trends and new developments in recommendation systems," *Scientometrics*, vol. 104, pp. 239-263, 2015, https://doi.org/10.1007/s11192-015-1595-5.

[10] J. P. Garcia Vazquez, R. S. Torres, and D. B. Pérez-Pérez, "Scientometric analysis of the application of artificial intelligence in agriculture," *Journal of Scientometric Research*, vol. 10, no. 1, pp. 55-62, 2021, https://doi.org/10.5530/jscires.10.1.7.

[11] M. Centenaro, C. E. Costa, F. Granelli, C. Sacchi, and L. Vangelista, "A survey on technologies, standards and open challenges in satellite IoT," *IEEE Communications Surveys & Tutorials*, vol. 23, no. 3, pp. 1693-1720, 2021, https://doi.org/10.1109/COMST.2021.3078433.

[12] R. Harikrishnan and M. M. Gaikwad, "IoT solutions for farmers on livestock management in smart city: A bibliometric survey," *Library Philosophy and Practice(e-journal)*, 2021, Art. no. 5796, https://digitalcommons.unl.edu/libphilprac/5796.

[13] B. Basumatary, M. Yuvaraj, and M. K. Verma, "Scientific communication of east Asian countries on internet of things (IoT): A performance evaluation based on scientometric tools," *Information Development*, vol. 40, no. 4, 2023, https://doi.org/10.1177/02666669221151160.

[14] M. J. Shayegan, "A bibliometric investigation into the literature of semantic reasoning in internet of things," *Internet Technology Letters*, vol. 6, no. 3, 2023, Art. no. e401, https://doi.org/10.1002/itl2.401.

[15] R. Y. Zhong *et al.*, "Prefabricated construction enabled by the internet-of-things," *Automation in*

Construction, vol. 76, pp. 59-70, 2017, https://doi.org/10.1016/j.autcon.2017.01.006.

[16] C. Çubukçu Çerasi and C. Aktürk, "A bibliometric analysis of smart cities and the internet of things," *Serbian Journal of Electrical Engineering*, vol. 20, no. 1, pp. 49-66, 2023, https://doi.org/10.2298/SJEE2301049C.

[17] N. Gupta and R. Chakravarty, "Trends in IoT research: A bibliometric and science mapping analysis of internet of things," *Library Philosophy and Practice(e-journal)*, 2021, Art. no. 5269, https://digitalcommons.unl.edu/libphilprac/5269.

[18] Y. Zhou and A. N. Ahmed, "Cryptocurrency and digital currency based on blockchain-enabled IoT: A bibliometric literature review," *Multimedia Tools and Applications*, vol. 83, pp. 35583–35606, 2023, https://doi.org/10.1007/s11042-023-16726-7.

[19] S. O. Olatinwo and T. H. Joubert, "Deep learning for resource management in internet of things networks: A bibliometric analysis and comprehensive review," *IEEE Access*, vol. 10, pp. 94691-94717, 2022, https://doi.org/10.1109/ACCESS.2022.3195898.

[20] A. Kaba and C. K. Ramaiah, "Bibliometric analysis of research output on the internet of things in the arab World," *DESIDOC Journal of Library & Information Technology*, vol. 39, no. 5, pp. 222-229, 2019.

[21] N. Rezaee, S. M. Zanjirchi, N. Jalilian, and S. M. H. Bamakan, "Internet of things empowering operations management; A systematic review based on bibliometric and content analysis," *Telematics and Informatics Reports*, vol. 11, 2023, Art. no. 100096, https://doi.org/10.1016/j.teler.2023.100096.

[22] K. Szum, "IoT-based smart cities: A bibliometric analysis and literature review," *Engineering Management in Production and Services*, vol. 13, no. 2, pp. 115-136, 2021, https://doi.org/ 10.2478/emj-2021-0017.

[23] H. X. Qin, Y. Hao, and J. G. Miao, "Analysis of research situation of wireless transmission of the internet of things based on bibliometrics," *Journal of Physics: Conference Series*, vol. 1948, 2021, Art. no. 012142, https://doi.org/10.1088/1742-6596/1948/1/012142.

[24] K. A. Darabkh, M. Al-Akhras, J. N. Zomot, and M. Atiquzzaman, "RPL routing protocol over IoT: A comprehensive survey, recent advances, insights, bibliometric analysis, recommendations, and future directions," *Journal of Network and Computer Applications*, vol. 207, 2022, Art. no. 103476, https://doi.org/10.1016/j.jnca.2022.103476.

[25] A. Patel *et al.*, "Review of artificial intelligence and internet of things technologies in land and water management research during 1991–2021: A bibliometric analysis," *Engineering Applications of Artificial Intelligence*, vol. 123, Part B, 2023, Art. no. 106335, https://doi.org/10.1016/j.engappai.2023.106335.

[26] S. Th. Konstantinidis, A. Billis, H. Wharrad, and P. D. Bamidis, "Internet of things in health trends through bibliometrics and text mining," in *Informatics for Health: Connected Citizen-Led Wellness And Population Health*, vol. 235. R. Randell, R. Cornet, C. McCowan, N. Peek, and P. J. Scott, Eds., IOS Press, 2017, pp.73-77, https://doi.org/10.3233/978-1-61499-753-5-73.

[27] X. Zhaoyuan, T. Jun, and F. Lihua, "A comparative analysis of the research on the internet of things between China-US based on bibliometric," *Journal of Library and Information Science in Agriculture*, vol. 31, no. 3, pp. 35-47, 2019, (in Chinese), https://doi.org/10.13998/j.cnki.issn1002-1248.2019.03.19-0237.

[28] J. Ruiz-Rosero, G. Ramirez-Gonzalez, J. M. Williams, H. Liu, R. Khanna, and G. Pisharody, "Internet of things: A scientometric review," *Symmetry*, vol. 9, no. 12, 2017, Art. no. 301, https://doi.org/10.3390/sym9120301.

[29] Y. Bouzembrak, M. Klüche, A. Gavai, and H. J. P. Marvin, "Internet of things in food safety: Literature review and a bibliometric analysis," *Trends in Food Science & Technology*, vol. 94, pp. 54-64, 2019, https://doi.org/10.1016/j.tifs.2019.11.002.

[30] J. R. K. Dabbakuti, R. Peesapati, and K. K. Anumandla, "Design and development of artificial intelligence enabled IoT framework for satellite based navigation services," *IEEE Transactions on Geoscience and Remote Sensing*, vol. 61, 2023, Art. no. 1001912, https://doi.org/10.1109/TGRS.2023.3328858.

[31] Z. Md Fadlullah and N. Kato, "On smart IoT remote sensing over integrated terrestrial-aerial-space networks: An asynchronous federated learning approach," *IEEE Network*, vol. 35, no. 5, pp. 129-135, 2021, https://doi.org/10.1109/MNET.101.2100125.

JSST
Journal of Space Science and Technology

P-ISSN: 2008-4560
E-ISSN: 2423-4516

Journal of Space Science and Technology

Vol. 17, Special Issue, pp. 15-21, 2024
https://doi.org/10.22034/jsst.2024.1510
Journal Homepage: https://jsstpub.com

Original Research Paper

A Correction on the Lambert Targeting Problem in the Perturbed Space Environment

Amirreza Kosari[1*], Ehsan Abbasali[2], and Majid Bakhtiari [3]

1. Faculty of New Science and Technologies, University of Tehran, Tehran, Iran
2. School of Aerospace Engineering, College of Interdisciplinary Science and Technology, University of Tehran, Tehran, Iran
3. School of Advance Technologies, Iran University of Science and Technology, Tehran, Iran

ARTICLE INFO

Article History:

Received 02 December 2024
Revised 27 December 2024
Accepted 29 December 2024
Available Online 30 December 2024

Keywords:

Lambert targeting problem correction
Shooting method
PSO optimization
Earth oblateness
Algorithm

ABSTRACT

This article introduces a novel correction algorithm designed to enhance the Lambert targeting problem (LTP) by addressing space perturbations. The proposed LTP correction (LTPC) algorithm integrates the traditional LTP with the shooting method and particle swarm optimization (PSO) to improve targeting accuracy. Following an initial solution using the LTP, the LTPC employs five sequential and iterative refinement stages to converge on a more precise result. The LTPC modifies the classical LTP to incorporate space perturbations, with Earth's oblateness being the primary perturbation considered. However, the algorithm is versatile and can be adapted to account for various types of space perturbations, broadening its applicability. The results demonstrate that the delta true anomaly, the difference between the desired arrival true anomaly and the actual arrival true anomaly, achieved by the LTPC is significantly smaller than that of the traditional LTP. This improvement highlights the LTPC's superior targeting accuracy. Notably, the LTPC achieves this enhanced precision without requiring a substantial increase in flight time or total velocity change compared to the classical LTP. This balance of accuracy and efficiency underscores the LTPC's effectiveness as a robust solution for space missions influenced by perturbations, paving the way for more reliable mission planning and execution.

*Corresponding Author's E-mail: kosari_a@ut.ac.ir

How to Cite this Article:
A. Kosari, E. Abbasali, and M. Bakhtiari, "A correction on the lambert targeting problem in the perturbed space environment," *Journal of Space Science and Technology*, Vol. 17, Special Issue, pp. 15-21, 2024, https://doi.org/10.22034/jsst.2024.1510.

1. INTRODUCTION

Lambert Targeting Problem (LTP) problem is the classical two-point boundary value problem (TPBVP) in celestial mechanics, that was first posed and solved by Johann Heinrich Lambert in 1761 [1]. It is known to have a unique solution for the fractional orbit transfer between prescribed positions in a prescribed "time of flight." Solving the problem requires determining the orbital arc (typically, solving for the initial velocity) connecting a prescribed initial position and final position, which correspond to the specified flight time. Many investigations established the LTP. A uniform solution to the Lambert problem is investigated by Kriz [2]. Lambert problem solution in the hill model of motion by Sukhanov and Prado [3]. They explain the LTP in the Lambert problem in the restricted three-body problem. Leeghim and Jaroux studied the Energy-optimal solution to the Lambert problem [4]. New solutions for the Lambert problem using regularization and Picard iteration are done by Woollands and Younes [5]. Thompson and Rostowfske express practical constraints for the applied Lambert problem [6]. Constrained multiple-revolution Lambert's problem is investigated by Zhang and Moratari. A fixed-time, multiple-revolution Lambert's problem is solved under given constraints in their study. A solution based on a dynamical approach for the multiple-revolution Lambert problem is investigated by Arlulkar and Naik [7]. Li and Han explained multiple-revolution solutions of the transverse-eccentricity-based Lambert problem [8]. The Uncertain Lambert problem with a probabilistic approach is explained by Adurthi and Majji [9]. All the mentioned research established the LTB ignoring the effects of space perturbations. But it should be noted that the effect of perturbations, however small, can be the cause of the success or failure of a space mission. Therefore, A novel correction algorithm is presented in this article to modify the Lambert targeting problem (LTP). To take into consideration space perturbations, the proposed LTPC (LTP Correction) algorithm combines the LTP with the shooting method [10], [11] and Particle Swarm Optimization (PSO) [12], [13]. Once the LTP is applied, the five consecutive iterative stages are established to modify it. The novel developed algorithm is called LTPC, which modifies LTP to regard space perturbations. The Earth's oblateness is considered a perturbation of interest [14]–[16]. This is while the proposed method can regard any space perturbations. The results indicate that the proposed LTPC has a much higher targeting accuracy, which is due to the ability to consider space perturbations

2. LAMBERT TARGETING PROBLEM (LTP)

Briefly, the Lambert Targeting problem (LTP) determines the transfer orbit between the initial orbit at the departure point $p_1(\vec{r}_d, \vec{v}_d)$ and final orbit at the arrival point $p_2(\vec{r}_a, \vec{v}_a)$ by having transfer time $t_{lambert}$ [4], [17], [18]. In fact, LTP finds the desired velocity vector $(\vec{V}_{LTP_d}, \vec{v}_{LTP_r})$ of transfer orbit at $\vec{r}_d$, $\vec{r}_a$. The orbital elements of transfer orbit are also obtained from the state vector at $(\vec{r}_a, \vec{V}_{LTP_a})$ or $(\vec{r}_a, \vec{V}_{LTP_d})$ [19]. The required total velocity changes for the deployment of a satellite equals:

$$\Delta\vec{V}_{Sat1} = \left|\vec{V}_{LTP_a} - \vec{v}_a\right| + \left|\vec{V}_{LTP_d} - \vec{v}_d\right| \quad (1)$$

One of the most critical requirements of designing a mission is trying to make it operational. LTP cannot be considered as a practical scheme in the mission design due to the following disadvantages:

- LTP cannot consider space perturbations due to the use of Kepler's equations of motion.
- Due to the accumulative trait of the perturbations, LTP is not suitable for long-term missions.

Therefore, since accurate targeting is vital in the orbital transferring and rendezvous maneuvers, the LTP is not appropriate for practical space missions.

Suppose that the Earth's oblateness is chosen as the space perturbations of interest in this research. The perturbed equations of motion due to the oblate perturbations are as follows [20]:

$$\begin{aligned}
\ddot{x} &= -\frac{\mu}{r^3}x + \frac{3J_2\mu R^2}{r^4}\left[\frac{x}{r}\left(\frac{5z^2}{r^2} - 1\right)\right] \\
\ddot{y} &= -\frac{\mu}{r^3}y + \frac{3J_2\mu R^2}{r^4}\left[\frac{y}{r}\left(\frac{5z^2}{r^2} - 1\right)\right] \\
\ddot{z} &= -\frac{\mu}{r^3}z + \frac{3J_2\mu R^2}{r^4}\left[\frac{z}{r}\left(\frac{5z^2}{r^2} - 3\right)\right]
\end{aligned} \quad (2)$$

In Eq. (2), the Earth's radius and the distance from the Earth's center to the center of the satellites are denoted by R and r, respectively. J_2 is the 2nd zonal harmonics of the Earth and zonal harmonics less than j_2 have been ignored [21]. The position and velocity vector of the satellite at the Earth-centered, Earth-coordinate frame (ECEF) is denoted by $\boldsymbol{X} = [x, y, z]$ and $\boldsymbol{V} = [\dot{x}, \dot{y}, \dot{z}]$, respectively. As an example, assume that the classic orbital elements of the initial and the final orbit are given in Table 1. The orbit's semi-major axis, eccentricity, inclination, right ascension of the ascending node, and the argument of perigee are denoted by a, e, i, Ω, ω.

Table 1. The classic orbital elements of the initial and the final orbit.

Orbit	$a(km)$	e	$i(deg)$	Ω(deg)	$\omega(deg)$
Initial	8000	0.25	25	25	8
Final	21500	0.09	25	25	8

Assume that the true anomaly of the arrival points θ_a are given in the mission profile as: $\theta_a = 60^{\circ}$. The flight time of the mission t and departure θ_d are selected as design parameters and selected by the optimization algorithm. This paper suggested the Particle Swarm Optimization (PSO) algorithm as the optimization algorithm and the Eq. (2) is selected as an objective function that could minimize the total velocity change of the maneuver and consequently the fuel consumption. The process of the PSO is fully described in section 3. The LTP is established in Fig. (1) once due to unperturbed and once to perturbed orbital equations of motion. Note that by setting the perturbation terms to zero in Eq. (2), the unperturbed equations will be obtained.

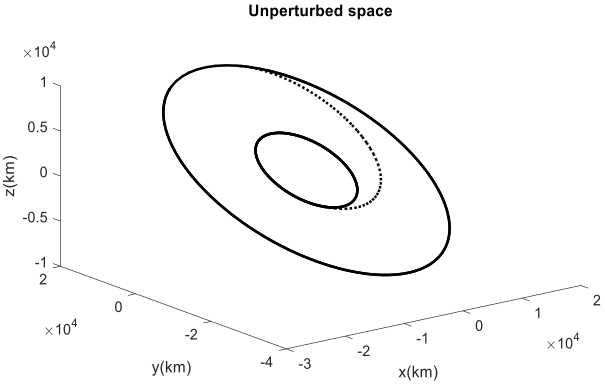

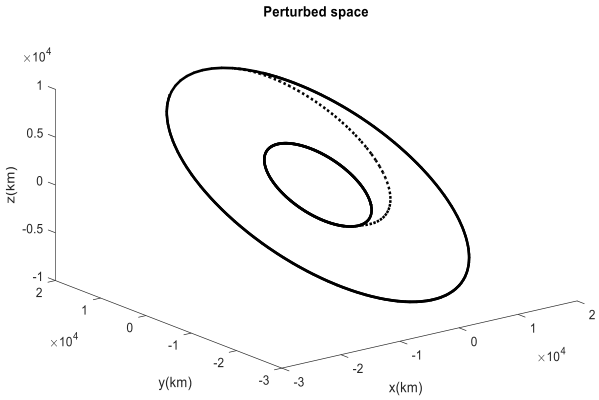

Fig. 1. The LTP maneuver once due to unperturbed and once to perturbed orbital equations of motion.

As mentioned the desired true anomaly was $\theta_a = 60^{\circ}$. However, according to Fig. 1, the effect of oblate perturbations has caused the satellite to arrive at the final orbits in $\theta_a = 69.8^{\circ}$. Therefore, according to Fig. 1, the inability of the LTP to consider perturbations has caused a significant decrease in targeting accuracy. Therefore, this paper proposed an approach to modify the LTP to consider space perturbations and accurate targeting. In section 3, the PSO optimization algorithm will be described, and section 4 will deal with the development of LTP Correction (LTPC).

3. PSO OPTIMIZATION

In computational science, particle swarm optimization (PSO) is a computational method that optimizes a problem by iteratively trying to improve a candidate solution with regard to a given measure of quality. First, a finite number of seeds is scattered randomly in the D-dimensional search space, representing the optimization problem's initial solutions. Then according to the seeds' fitness value, the member of the colonies is ranked and sorted. The i-th plant, which represents the i-th initial position, is shown by $X^{i,best}$. An $X^{i,best}$ which has the most satisfying fitness value is the best position of the colony, and is shown by X^{gbest}. Updating the speed and position of each particle is obtained from the following equations [22-26].

$$v^{i,s}[t+1] = \gamma V^{i}[t] + c_1 r_{1,s}\left(X^{i,best}[t] - X^{i}[t]\right) + c_2 r_{2,s}\left(X^{gbest}[t] - X^{i}[t]\right) \quad (3)$$

$$X^{i,s}[t+1] = X^{i}[t] + V^{i,s}[t+1] \quad (4)$$

The inertia weight $\boldsymbol{\gamma}$ may help to keep the motion of each particle in its main direction and balance the global and local search. Also, in Eqs. (3) and (4), the velocity and position of the *s*-th seed of the *i*-th member shows by $\boldsymbol{V^{i,s}}$, $\boldsymbol{X^{i,s}}$ respectively.

The cognitive coefficient $\boldsymbol{c_1}$and social coefficient $\boldsymbol{c_2}$ control the rate of convergence towards a personal best or global best location. $\boldsymbol{r_{1,s}}$ and $\boldsymbol{r_{2,s}}$ are the random numbers in the range $[\mathbf{0}, \mathbf{1}]$. The flight time of the mission $\boldsymbol{t}$ and departure $\boldsymbol{\theta_d}$ are selected as design parameters and selected by the PSO optimization algorithm.

4. LAMBERT TARGETING PROBLEM CORRECTION (LTPC)

In this article, an innovative correction algorithm is proposed to modify LTP. The proposed LTPC (LTP Correction) algorithm is developed by combining the LTP with the shooting method. The shooting method solves a two-boundary value problem by reducing it to an initial value problem system [14]. The orbital transfer mission is performed once applying the LTP. Then, the following iterative process is established to modify LTP. The newly developed algorithm is called LTPC, which modifies LTP to consider space perturbations:

1. The LTP is applied and optimized with the PSO for the satellite deployment mission.
2. The departure position vector of the LTP maneuver $\vec{r}_d$ is chosen as an initial condition.
3. The new impulse velocity vector $\vec{V}_{P_s}$ at $\vec{r}_d$ and the new flight time t_s are also selected as an initial condition by PSO, and the shooting algorithm started (starting LTP correction).
4. The transfer orbit is determined by applying the system of Eq. (2) with the selected initial conditions in the previous steps.
5. Calculate the difference between the new position and the velocity vector of the satellite $(\vec{r}_{a_N}, \vec{v}_{a_N})$ relative to the values determined by the LTP $(\vec{r}_a, \vec{v}_a)$ at the arrival point.
6. The LTP is replaced by the transfer orbit determined by the shooting algorithm (LTPC) if condition (5) is satisfied:

$$\begin{aligned} &\left|\vec{r}_{a_N} - \vec{r}_{a_{MILTP}}\right| < 2 \times 10^{-3}\ (m) \\ &\left|\vec{v}_{a_N} - \vec{v}_{a_{MILTP}}\right| < 10^{-3}\ (\frac{km}{s}) \end{aligned} \quad (5)$$

7-If the delta values do not meet condition (5), then return to step 3 and shoot again. In the results section, the correctness of the proposed algorithm will be validated.

5. RESULT

The main purpose of this article is to develop an orbital transfer that has accurate targeting and could regard space perturbation. For this reason, first, the LTP is suggested for accurate targeting. Since the LTP cannot consider space perturbations, this paper proposed a correction on the LTP that modified the LTP to regard space perturbations with accurate targeting. In this section, two cases study is investigated.

The classic orbital elements of the initial and the final orbit of these cases study are given in table 2.

Table 2. the classic orbital elements of the initial and the final orbit of the case study.

Orbit	$a(km)$	e	$i(deg)$	Ω(deg)	$\omega(deg)$
Initial	9000	0.1	20	20	10
Final	23000	0.08	20	20	10

In the first case study, it is assumed that the satellite must be deployed at $\theta_a = 150^{\circ}$. The LTP is compared with the proposed LTPC in Fig. 2.

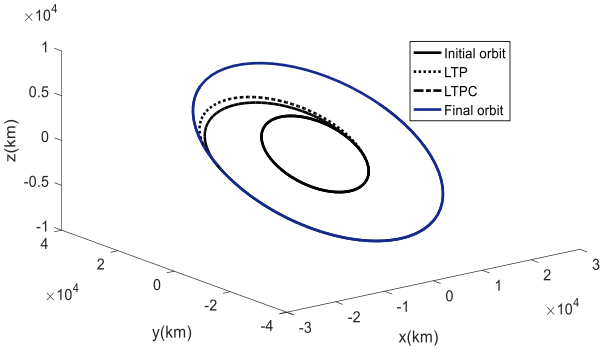

Fig. 2. The comparison between the LTP and proposed LTPC in the first case study.

The arrival true anomaly θ_a, the total velocity change ΔV_{tot} and the flight time t between the LTP and the proposed LTPC are compared in Table 3 for the first case study.

Table 3. the comparison of arrival true anomaly θ_a, the total velocity change ΔV_{tot} and the flight time t between the LTP and the proposed LTPC.

	$\theta_a(deg)$	$\Delta V_{tot}\left(\frac{km}{s}\right)$	$t(sec)$
LTP	161	2.18	10403
LTPC	153	2.21	10487

According to the table 2, the delta true anomaly between the desired true anomaly $\theta_a = 150^\circ$ and the arrival true anomaly LTP and proposed LTPC are 11° and 3°respectively. Therefore, the LTPC has accurate targeting with considering space perturbation. This holds despite the fact that the difference between the velocity change and flight time of the LTP and LTP are neglectable. In the first case study, it is assumed that the satellite must be deployed at $\theta_a = 225^\circ$. The LTP is compared with the proposed LTPC in the Fig. 3.

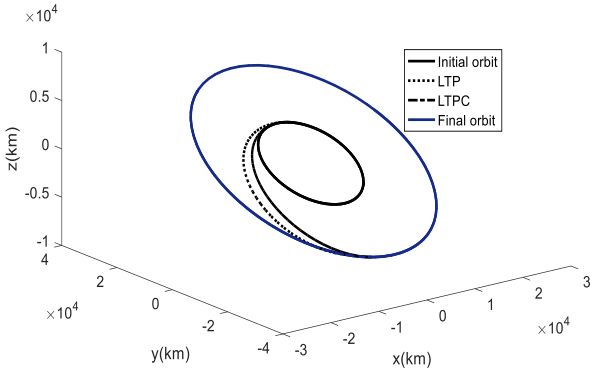

Fig. 3. The comparison between the LTP and proposed LTPC in the second case study.

The arrival true anomaly θ_a, the total velocity change ΔV_{tot} and the flight time t between the LTP and the proposed LTPC are compared in Table 4 for the first case study.

Table 4. the comparison of arrival true anomaly θ_a, the total velocity change ΔV_{tot} and the flight time t between the LTP and the proposed LTPC.

	$\theta_a(deg)$	$\Delta V_{tot}\left(\frac{km}{s}\right)$	$t(sec)$
L T P	237.4	2.32	11812
L T P C	227.5	2.35	11854

According to Table 4, the delta true anomaly between the desired true anomaly $\theta_a = 225$ and the arrival true anomaly LTP and proposed LTPC are 12.4° and 2.5°respectively. Therefore, like the first case study, the LTPC has accurate targeting considering the space perturbation and as illustrated in the first case study although the difference between the velocity change and flight time of the LTP and LTP are neglectable.

6. CONCLUSION

The primary objective of this paper was to develop an orbital transfer maneuver with high targeting accuracy, capable of accounting for all space perturbations, thus ensuring its practicality for real-world missions. The Lambert Targeting Problem (LTP) was initially proposed as an accurate orbit transfer maneuver. However, the LTP's inability to account for space perturbations significantly reduced its targeting accuracy, making it unsuitable for operational missions due to the following limitations:

Inability to account for space perturbations: The LTP relies on Kepler's equations of motion, which do not consider perturbative forces.

Unsuitability for long-term missions: The cumulative effect of perturbations over time renders the LTP ineffective for extended missions.

To address these shortcomings, this paper introduces an innovative correction algorithm, referred to as the Lambert Targeting Problem Correction (LTPC) algorithm. The LTPC combines the LTP with the shooting method to improve its performance. The orbital transfer maneuver begins with the application of the LTP, followed by five iterative stages designed to refine the solution. This process enables the LTPC to account for space perturbations effectively.

In this study, Earth's oblateness was considered the primary perturbation of interest. The results demonstrated that the LTPC achieved a significantly smaller delta true anomaly, the difference between the desired arrival true anomaly and the actual arrival true anomaly—compared to the classical LTP. Moreover, the LTPC maintained comparable flight times and total velocity change requirements to the LTP. These findings highlight the LTPC's superior targeting accuracy, attributed to its ability to incorporate space perturbations.

CONFLICT OF INTERESTS

No conflict of interest has been expressed by the authors.

REFERENCES

[1] J. J. Gray, "Johann heinrich lambert, mathematician and scientist, 1728–1777," *Historia Mathematica*, vol. 5, no. 1, pp. 13–41, 1978, https://doi.org/10.1016/0315-0860(78)90133-7.

[2] J. Kriz, "A uniform solution of the lambert problem," *Celestial Mechanics*, vol. 14, pp. 509–513, 1976, https://doi.org/10.1007/BF01229061.

[3] A. Sukhanov and A. F. B. A. Prado, "Lambert problem solution in the hill model of motion," *Celestial Mechanics and Dynamical Astronomy*, vol. 90, pp. 331–354, 2004, https://doi.org/10.1007/s10569-004-1508-z.

[4] H. Leeghim and B. A. Jaroux, "Energy-optimal solution to the lambert problem," *Journal of Guidance, Control, and Dynamics*, vol. 33, no. 3, pp. 1008–1010, 2010, https://doi.org/10.2514/1.46606.

[5] R. M. Woollands, A. Bani Younes, and J. L. Junkins, "New solutions for the perturbed lambert problem using regularization and picard iteration," *Journal of Guidance, Control, and Dynamics*, vol. 38, no. 9, pp. 1548–1562, 2015, https://doi.org/10.2514/1.G001028.

[6] B. F. Thompson and L. J. Rostowfske, "Practical constraints for the applied Lambert problem," *Journal of Guidance, Control, and Dynamics*, vol. 43, no. 5, pp. 967–974, 2020, https://doi.org/10.2514/1.G004765.

[7] P. V. Arlulkar and S. D. Naik, "Solution based on dynamical approach for multiple-revolution lambert problem," *Journal of Guidance, Control, and Dynamics*, vol. 34, no. 3, pp. 920–923, 2011, https://doi.org/10.2514/1.51723.

[8] Q. He, J. Li, and C. Han, "Multiple-revolution solutions of the transverse-eccentricity-based lambert problem," *Journal of Guidance, Control, and Dynamics*, vol. 33, no. 1, pp. 265–269, 2010, https://doi.org/10.2514/1.45041.

[9] N. Adurthi and M. Majji, "Uncertain lambert problem: A probabilistic approach," *The Journal of the Astronautical Sciences*, vol. 67, pp. 361–386, 2020, https://doi.org/10.1007/s40295-019-00205-z.

[10] Q. M. Al-Mdallal, M. I. Syam, and M. N. Anwar, "A collocation-shooting method for solving fractional boundary value problems," *Communications in Nonlinear Science and Numerical Simulation*, vol. 15, no. 12, pp. 3814–3822, 2010, https://doi.org/10.1016/j.cnsns.2010.01.020.

[11] S. N. Ha, "A nonlinear shooting method for two-point boundary value problems," *Computers & Mathematics with Applications*, vol. 42, no. 10–11, pp. 1411–1420, 2001, https://doi.org/10.1016/S0898-1221(01)00250-4.

[12] H. Hajimirsadeghi and C. Lucas, "A hybrid IWO/PSO algorithm for fast and global optimization," in *IEEE EUROCON 2009*, St. Petersburg, Russia, 2009, pp. 1964–1971, https://doi.org/10.1109/EURCON.2009.5167916.

[13] M. Bakhtiari, K. Daneshjou, and E. Abbasali, "A new approach to derive a formation flying model in the presence of a perturbing body in inclined elliptical orbit: relative hovering analysis," *Astrophysics and Space Science*, vol. 362, 2017, Art. no. 36, https://doi.org/10.1007/s10509-016-2968-9.

[14] E. Abbasali, A. Kosari, and M. Bakhtiari, "Effects of oblateness of the primaries on natural periodic orbit-attitude behaviour of satellites in three body problem," *Advances in Space Research*, vol. 68, no. 11, pp. 4379-4397, 2021, https://doi.org/10.1016/j.asr.2021.08.026.

[15] M. Bakhtiari, E. Abbasali, S. Sabzy, and A. Kosari, "Natural coupled orbit—attitude periodic motions in the perturbed-CRTBP including radiated primary and oblate secondary," *Astrodynamics*, vol. 7, pp. 229–249, 2023, https://doi.org/10.1007/s42064-022-0154-0.

[16] E. Abbasali, A. Kosari, and M. Bakhteiari, "Restricted three-body problem considering perturbations of oblate primaries," *Journal of Aerospace Science and Technology*, vol. 13, no. 2, pp. 27-35, 2020, https://doi.org/10.22034/jast.2021.128013.

[17] A. Shirazi, J. Ceberio, and J. A. Lozano, "Optimal multi-impulse space rendezvous considering limited impulse using a discretized Lambert problem combined with evolutionary algorithms," in *8th European Conference for Aeronautics and Space Sciences (Eucass)*, Madrid, Spain, 2019, pp. 1-14, https://doi.org/10.13009/EUCASS2019-215.

[18] A. Shirazi, J. Ceberio, and J. A. Lozano, "An evolutionary discretized Lambert approach for optimal long-range rendezvous considering impulse limit," *Aerospace Science and Technology*, vol. 94, 2019, Art. no. 105400, https://doi.org/10.1016/j.ast.2019.105400.

[19] D. A. Vallado, *Fundamentals of Astrodynamics and Applications*, 2nd ed. Springer Science & Business Media, 2004.

[20] H. D. Curtis, *Orbital Mechanics for Engineering Students*, 3rd ed. Elsevier Science, 2013.

[21] M. Bakhtiari, K. Daneshjou, and M. Fakoor, "Relative hovering analysis about an elliptical perturbed orbit with consideration of dynamic air drag and oblate Earth," *Aerospace Science and*

Technology, vol. 70, pp. 286–299, 2017, https://doi.org/10.1016/j.ast.2017.07.034.

[22]M. Bakhtiari, K. Daneshjou, and A. A. Mohammadi-Dehabadi, "The effects of parking orbit elements on designing of on-orbit servicing missions," *Proceedings of the Institution of Mechanical Engineers, Part G: Journal of Aerospace Engineering*, vol. 233, no. 3, pp. 793–810, 2019, https://doi.org/10.1177/0954410017740921.

[23]E. Abbasali, A. Kosari, M. Bakhtiari, "Achieving solar sail orbital maintenance with adjustable ballast masses in the ERTBP," *Advances in Space Research*, vol. 75, no. 1, pp. 1297-1309, 2025, https://doi.org/10.1016/j.asr.2024.09.064.

[24]E. Abbasali, A. Kosari, and M. Bakhtiari, "Solar sail orbital motion at the non-autonomous oblate Earth-Moon System: Family of periodic orbits," *Archive of Applied* Mechanics, vol. 94, pp. 3785-3801, 2024, https://doi.org/10.1007/s00419-024-02695-2.

[25]M. Bakhtiari and E. Abbasali, "An optimal deployment strategy for multi-plane satellite constellation using a generalized non-planar maneuver," *Astrophysics and Space Science*, vol. 369, 2024, Art. no. 26, https://doi.org/10.1007/s10509-024-04288-5.

[26]M. Bakhtiari, E. Abbasali, and K. Daneshjoo, "Minimum cost perturbed multi-impulsive maneuver methodology to accomplish an optimal deployment scheduling for a satellite constellation," *The Journal of the Astronautical Sciences*, vol. 70, 2023, Art. no. 18, https://doi.org/10.1007/s40295-023-00381-z.

JSST
Journal of Space Science and Technology

P-ISSN: 2008-4560
E-ISSN: 2423-4516

Journal of Space Science and Technology

Vol. 17, Special Issue, pp. 22-31, 2024
https://doi.org/10.22034/jsst.2024.1491
Journal Homepage: https://jsstpub.com

Original Research Paper

Design and Analysis of Plasma-Based Reconfigurable Maxwell Fish Eye Lens Antennas

Jafar Bazrafshan[1], Fatemeh Sadeghikia[2*], Mohamed Himdi [3], Ali Karami Horestani[4], and Hajar Binti Ja'afar[5]

1, 2, 4. Aerospace Research Institute, Ministry of Science, Research and Technology, Tehran, Iran
3. University of Rennes 1, Rennes, France
5. School of Electrical Engineering, College of Engineering, MARA Technological University, Malaysia

ARTICLE INFO

Article History:

Received 09 July 2024
Revised 09 October 2024
Accepted 24 November 2024
Available Online 01 December 2024

Keywords:

Maxwell fish eye (MFE) lens
Plasma dielectric material
Reconfigurable antennas
Plasma lens antenna
Reconfigurable lens
Spherical lens
Hemispherical lens

ABSTRACT

This paper investigates the feasibility of employing plasma dielectric material to develop a Maxwell Fish Eye (MFE) lens antenna, functioning as a gradient index (GRIN) lens antenna with reconfigurability. The study focuses on the design, simulation, and analysis of both spherical and hemispherical MFE plasma lenses. Using geometric optics (GO), the analytical design equations of the Maxwell Fish Eye (MFE) lens are derived. Furthermore, the refractive index profile in the radial direction of the plasma-based MFE lens is extracted using the hyperbolic function—a conventional method for MFE lenses—while accounting for the unique property of plasma dielectrics, where the refractive index is smaller than 1. A prototype of the plasma-based MFE lens is designed based on the derived equations at an operating frequency of 10 GHz, and its performance is evaluated through numerical simulations considering a layered refractive index profile for the lens. The results reveal significant improvements in radiation characteristics, with the spherical configuration achieving a 6.5 dBi gain enhancement and the hemispherical lens demonstrating a remarkable 12.8 dBi gain enhancement. Additionally, the lens provides dynamic control over radiation patterns by leveraging the tunable nature of plasma. This reconfigurability is achieved by selectively switching plasma layers ON or OFF, effectively altering the lens's refractive index distribution in real time. Moreover, based on the results of a parametric analysis, a layer thickness of t = R/10, where R is the radius of the lens, provides the best trade-off between gain enhancement and implementation simplicity. The findings demonstrate the potential of plasma-based MFE lenses to achieve advanced reconfigurability in antenna systems. Such structures offer significant advantages for modern communication systems, where adaptability and beam shaping are critical. This work establishes a foundation for future research into plasma-enabled gradient index devices for reconfigurable antenna applications in 5G, 6G, and beyond.

*Corresponding Author's E-mail: sadeghi_kia@ari.ac.ir

How to Cite this Article:
J. Bazrafshan, F. Sadeghikia, M. Himdi, A. Karami Horestani, and H. Binti Ja'afar, "Design and analysis of plasma-based reconfigurable maxwell fish eye lens antennas," *Journal of Space Science and Technology*, Vol. 17, Special Issue, pp. 22-31, 2024, https://doi.org/10.22034/jsst.2024.1491.

1. INTRODUCTION

Microwave lenses are broadly classified into two categories based on their material composition: homogeneous and non-homogeneous. While homogeneous lenses are favorable due to their simple implementation [1], inhomogeneous lenses have garnered significant attention due to features such as high gain [2], the ability to generate multiple beams [3], controllable beam direction [4], and broadband radiation characteristics [5].

Among non-homogeneous lenses, the Maxwell fish-eye (MFE) lenses with spherical or hemispherical configurations, can direct electromagnetic waves to focus radiation from a wide field of view onto a focal point. Classified as a gradient index (GRIN) lens, the refractive index of the MFE lens changes smoothly from the center toward the outer layers [6-8].

The significance of MFE lenses in antenna design lies in their potential to enhance beamforming capabilities [9], improve long-range communication [5], and enable novel antenna configurations for diverse applications [10-14]. For instance, innovative designs such as multichannel lenses with beam splitters based on the MFE lens have been proposed in [10] and [11]. Moreover, using a combination of etched planar meta-surfaces and half MFE lens antennas, good focusing has been achieved [13]. In [14], wide-angle beam scanning has been demonstrated with MFE and Gutman lenses.

Driven by the need for adaptability and versatility in modern communication systems, reconfigurable antennas have become another essential concept in the field of antenna engineering [15]. Traditional approaches often face challenges in balancing performance and flexibility, relying on switching mechanisms that compromise efficiency and design simplicity [16]. Notable innovations have emerged, including optical methods using photoconductive materials, structural alterations in antenna configurations, and the incorporation of novel materials such as ferrite and plasmas into antenna structures.

Dynamic adjustment of plasma properties to create reconfigurable antennas has been investigated in various studies [17-30]. Demostrated antennas offer the advantage of adaptability, allowing for the dynamic tailoring of radiation patterns and beam directions without the need for complex switching components [31-36]. Traditional approaches to reconfiguring MFE lenses often rely on mechanical adjustments [10,12], and [14], such as sliding or rotating the lens or repositioning the feed source. While these methods provide beam control, they lack the rapid adaptability demanded by modern communication systems. These mechanical techniques, though effective, can be slow, bulky, and less precise for rapid real-time applications. In contrast, reconfigurable materials such as plasma offer a more dynamic solution, enabling real-time modifications to the refractive index by controlling plasma properties. This allows faster beam steering, and improved precision, and leads to the way for advanced features such as adaptive beamforming.

Although many studies have been carried out on the application of plasma media in their conductive mode for instance for the realization of antennas and reflectors [19-30], there are limited studies on the applications of plasma media in their dielectric mode, especially as dielectric lens antennas [17-19]. However, it is widely acknowledged that plasma structures exhibit favorable dielectric properties at frequencies higher than the plasma frequency. At such frequencies, control over the plasma refractive index can be achieved by adjusting the plasma frequency, presenting an opportunity for the development of dielectric lenses with controllable focal lengths [17].

This study explores the integration of plasma in its dielectric mode into an MFE lens, introducing a novel reconfigurable antenna system. While MFE lenses have been extensively studied both theoretically and experimentally, designing MFE lenses made of a dielectric with a refractive index of less than one represents a new frontier. To this end, existing analytical design equations for MFE lenses need to be modified, and the refractive index distribution profile must be redefined. Therefore, a key novelty of this research is the development of updated analytical design equations for MFE lenses incorporating plasma dielectrics, addressing a significant gap in the field.

Additionally, by controlling the refractive index of plasma, the lens characteristics can be dynamically adjusted, offering a more adaptable solution compared to traditional lenses. This reconfigurability, achieved by switching the lens layers ON or OFF, represents a second major novelty of this study. This paper aims to investigate

the feasibility of realizing this plasma-based lens and evaluating its performance.

The rest of the paper is organized as follows: Background information on plasma material in the dielectric mode is provided first. Next, the analytical design equations for spherical MFE lenses based on geometrical optics are presented. Then, the structure and design equations of MFE lenses based on plasma material are outlined. The performance of the proposed lens antenna is numerically analyzed in the subsequent section, followed by a detailed discussion and analysis of the findings. Finally, the study is concluded with insights into the significance of this research.

2. PLASMA DIELECTRIC THEORY

Plasma, in its general form, constitutes an ionized inert gas confined within a dielectric container. In this study, the dielectric mode of plasma material is used in the structure of the MFE lens, i.e., the plasma frequency is smaller than the operating frequency of the antenna [17]. The plasma medium is commonly represented using the Drude or Lorentz dispersion model, and under low-pressure conditions, its complex relative permittivity is defined as [37]:

$$\epsilon_p = 1 - \frac{\omega_p^2}{\omega(\omega - j\nu)} = \epsilon' + j\epsilon'', \tag{1}$$

Where ω = 2πf is the operating angular frequency, υ is the collision frequency of the plasma, and ωp = 2πfp is the plasma angular frequency. The plasma angular frequency is defined as:

$$\omega_p = \sqrt{Ne^2/m\varepsilon_0}, \tag{2}$$

Where m and e represent the electron mass and charge, N is the plasma electron density, and ε_0 denoted the free space permittivity. Neglecting the imaginary part of the plasma permittivity, the plasma relative permittivity is expressed as:

$$\varepsilon_p = 1 - \frac{\omega_p^2}{\omega^2 + \nu^2}. \tag{3}$$

The refractive index of plasma can be calculated based on the plasma permittivity:

$$n_p = \sqrt{\varepsilon_p} \tag{4}$$

It is important to note that, unlike conventional dielectrics, the plasma permittivity in plasma dielectrics, and consequently the refractive index of plasma, are smaller than one and greater than zero. Therefore, the phase velocity of an electromagnetic (EM) wave propagating in a plasma dielectric is higher than in free space. This characteristic significantly impacts the shape or distribution of the refractive index in lenses made of plasma [17].

3. ANALYTICAL DESIGN EQUATIONS

In this section, the analytical design equations and fundamental principles of spherical MFE plasma lenses are derived using the geometric optics (GO) method. These equations will be applied in the next section to design a prototype of a plasma-based MFE lens.

Let's start by analyzing the refractive index profile in MFE lenses, which plays a critical role in directing electromagnetic waves to achieve the desired focusing properties. A common mathematical model used to describe this profile for conventional MFE lenses is the hyperbolic function as follows [9]:

$$n(r) = \frac{n_0}{1+\left(\frac{r}{R}\right)^2} \qquad 0 < r < R \tag{5}$$

In this equation, n_0 represents the refractive index at the center of the sphere, R is the radius of the lens, and r is the radial distance from the center. This equation provides a smooth decrease in the refractive index from the center to the outer layers of the lens. By adjusting the parameters n_0 and R, it becomes possible to tailor the behavior of the lens antenna system.

In the geometric optics method [38], the Eikonal equation is a simplified form of the Maxwell's equations. It provides an approximation for describing the trajectory of rays in a medium with a spatially varying refractive index, such as MFE lens. The equation is given by [39]:

$$|\nabla u(\vec{r})| = n^2(\vec{r}) \tag{6}$$

where $\vec{r}$ is the radius vector, and $n(\vec{r})$ represents the refractive index of the medium. In two dimensions (on the x-y plane), the Eikonal equation becomes:

$$\left(\frac{\partial u(x,y)}{\partial x}\right)^2 + \left(\frac{\partial u(x,y)}{\partial y}\right)^2 = n^2(x,y) \tag{7}$$

Using the method of characteristics, this equation can be transformed into a system of ordinary differential equations (ODEs):

$$\begin{cases} \frac{dx}{dt} = \frac{p_1}{n^2} \\ \frac{dy}{dt} = \frac{p_2}{n^2} \\ \frac{dp_1}{dt} = \frac{1}{n}\frac{\partial n}{\partial x} \\ \frac{dp_2}{dt} = \frac{1}{n}\frac{\partial n}{\partial y} \end{cases} \quad (8)$$

where $p_1 = \frac{\partial u}{\partial x}$ and $p_2 = \frac{\partial u}{\partial y}$. The functions *x(t)*, *y(t)*, $p_1(t)$ and $p_2(t)$ describe the ray trajectories in the system. The partial derivatives of the refractive index, given by equation (5), in the *x*-*y* plane are expressed as follows.

$$\frac{\partial n(x,y)}{\partial x} = -\frac{2n^2(x,y)}{n_0 R^2}(x - X_0) \quad (9a)$$

$$\frac{\partial n(x,y)}{\partial y} = -\frac{2n^2(x,y)}{n_0 R^2}(y - Y_0) \quad (9b)$$

The initial conditions at $t = 0$ are defined by:

$$\begin{cases} x(t) = x_0 \\ y(t) = y_0 \\ p_1(t) = cos(\alpha)\, n(x_0, y_0) \\ p_2(t) = sin(\alpha)\ n(x_0, y_0) \end{cases} \quad (10)$$

Where α is the incident angle of the beam from the feed, and (x0, y0) represents the coordinates of the feed.

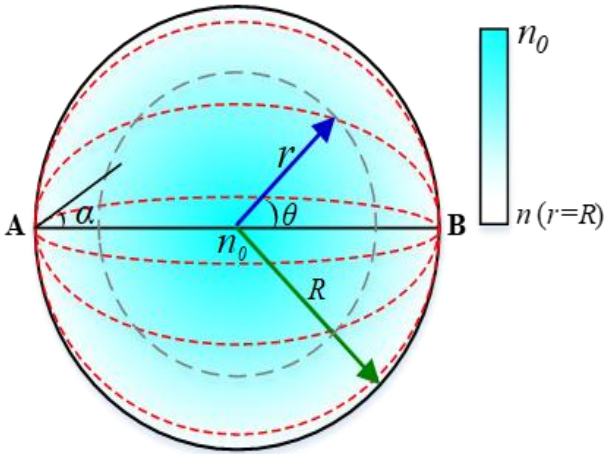

Fig. 1. Rays in a plasma-based MFE lens, with the representation of refractive index profile along the radial direction.

It's worth noting that the spherical MFE lens images a point on its surface to the opposite point, achieving diametric coverage, as illustrated in Fig. 1. The trajectory of a ray leaving point A and arriving at point B, diametrically opposite to point A, as depicted by the red dashed line in Fig. 1, is governed by the following equation [9]:

$$\theta = sin^{-1}\left(\frac{C(R^2 - r^2)}{Rr\sqrt{n_0^2 R^2 - 4C^2}}\right) \quad (11)$$

Here, *C* is a parameter that is constant for each layer, contributing to the trajectory of the ray within the lens structure.

It is noteworthy that the refractive index profile of a typical MFE lens using conventional dielectrics commonly ranges from $n_0 = 2$ at its center to $n = 1$ at the outer surface. However, since the refractive index of a plasma dielectric is always smaller than 1, it raises the question of whether it's feasible to use this type of dielectric in the MFE lens or not.

To address this, incorporating equations (3) and (5), and considering $n_0 = 1$, which represents the maximum refractive index of the plasma dielectric at the center of the lens, a design equation is extracted for the plasma MFE lens. Thus, the plasma frequency distribution profile for this lens is extracted as:

$$f_p(r) = \frac{1}{2\pi}\sqrt{(\omega^2 + \nu^2)\left(1 - \left(\frac{n_0}{1 + \left(\frac{r}{R}\right)^2}\right)^2\right)} \quad (12)$$

Using (12), it is possible to calculate the plasma frequency in different radii of a plasma MFE lens. To have a better insight into the differences between the refractive index profiles of a conventional MFE lens and the proposed plasma-based MFE lens, these two profiles are compared in Fig. 2, where both spherical lenses have a radius of $R = 100$ mm. It is evident from the figure that the range of variation in the refractive indices for the two lenses is significantly different. Additionally, while the refractive index profile in the plasma MFE lens is dependent on the operating frequency, it remains constant in the conventional MFE lens.

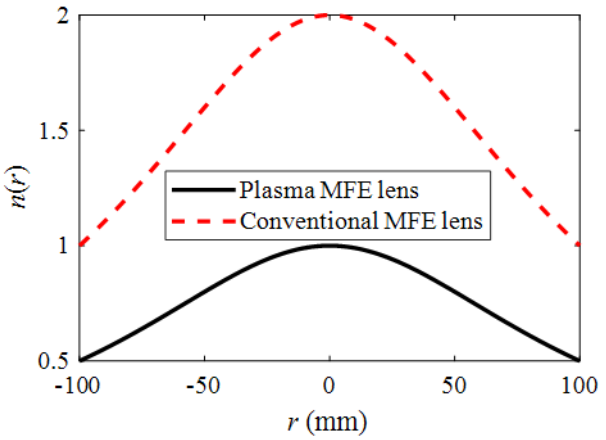

Fig. 2. Comparison of refractive index profile distributions along the radius of a conventional MFE lens and a plasma-based MFE lens at f = 10 GHz and ν = 1 GHz.

To evaluate the collimating capability of the analytically designed plasma MFE lens, Fig. 3 presents a snapshot of the propagating wave through this lens. This result is obtained by numerically solving the Eikonal equations at a frequency of f = 10 GHz for the refractive index profile shown in Fig. 2. The figure clearly illustrates that the beam is collimated after passing through the plasma MFE lens. In this simulation, the feed is a rectangular waveguide (WR90).

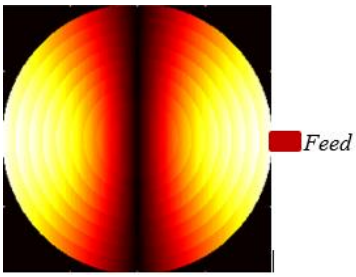

Fig. 3. Snapshot showing the analytically obtained propagating wave from the plasma MFE lens at f = 10 GHz corresponding to the refractive index profile illustrated in Fig. 2.

In the following section, the performance and feasibility of the proposed plasma MFE lens are further analyzed through full-wave electromagnetic computations.

4. DESIGN OF A PROTOTYPE AND NUMERICAL INVESTIGATION

In this section, a plasma-based MFE lens antenna is designed based on the analytical equations presented in the previous section for operation at f = 10 GHz. The performance of the designed lens is evaluated through numerical simulations, considering two configurations: a spherical lens and a hemispherical lens.

For simulation purposes, the time-domain solver of the commercial software CST Microwave Studio® is employed. Moreover, a rectangular waveguide (WR90) is placed in front of the lens to illuminate the lens. For an MFE lens, a waveguide feed offers advantages in terms of integration and compactness, particularly at higher frequencies. However, the type of feed does not significantly affect the overall performance of the lens and thus can be replaced with other feeds such as horn antennas.

Let's start with the design of the spherical MFE plasma lens which has a radius of R = 100 mm. The plasma medium is modelled as collisional, with a collision frequency of ν = 1 GHz, to provide a more realistic representation of the lens's performance. Based on these initial parameters, plasma frequency distribution is derived, as shown by the red dashed line in Fig. 4.

It's important to note that in practical applications, a stepped index profile is typically used to implement MFE lenses. Accordingly, in this study, the plasma frequency distribution is discretized along the lens radius, forming a staircase-like profile, as shown by the solid black line in Fig. 4. So, the plasma MFE lens, as depicted in Fig. 6, is divided into ten distinct spherical layers, each with a thickness of 10 mm.

To calculate the characteristics of the various layers, with each outer radius denoted by r_i (where i represents the layer number from 1 to 10), the following procedure is employed:

- An initial refractive index of n_0 = 1 is assumed at the center of the sphere.
- The refractive index $n_p(r_i)$ for each layer is calculated using Eq. (5), with results displayed in Fig. 6, comparing the continuous inhomogeneous and stepped index profiles.
- Finally, the plasma frequency for each layer, $f_p(r_i)$, is computed using Eq. (12).

Note that for simplicity, the impact of dielectric containers surrounding the spherical layers has been neglected in this feasibility study. Following the procedure, the characteristics of the plasma MFE lens are determined. In practice, a controllable DC

power supply based on an electrical dimmer can effectively adjust the plasma frequency in the layers. For instance, in [17], the plasma frequency was controllable between 2 GHz and 7.8 GHz using DC biasing. This flexibility allows for fine-tuning the refractive index of plasma, enabling dynamic control of the properties of the lens. While this method has successfully stabilized plasma states, alternative methods, such as AC or pulsed biasing, may further enhance flexibility, providing additional options for optimizing plasma performance in this application.

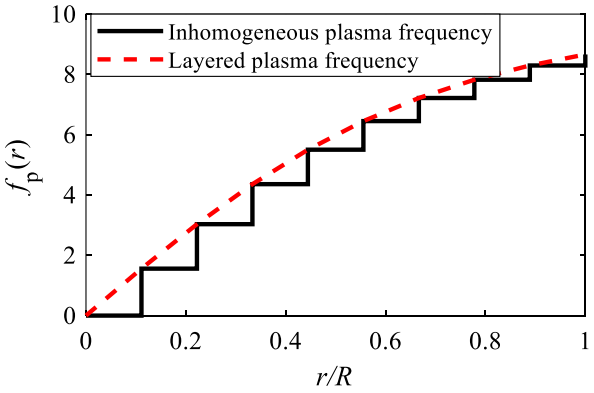

Fig. 4. Plasma frequency versus normalized radius of the plasma MFE lens.

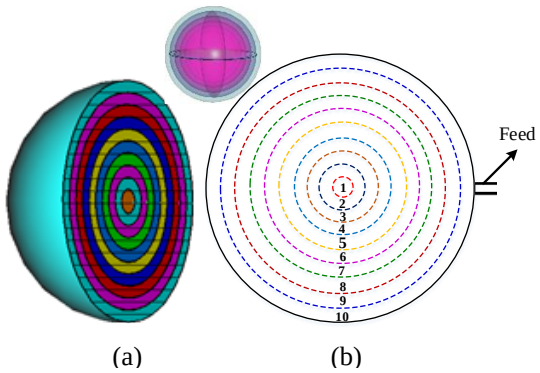

Fig. 5. (a) 3-D view, (b) side view of the ten-layer plasma MFE lens.

Table 1. Permittivity of the plasma layers in the plasma MFE lens.

Parameter	Quantity
$\varepsilon_p(r_{10})$	0.25
$\varepsilon_p(r_9)$	0.31
$\varepsilon_p(r_8)$	0.38
$\varepsilon_p(r_7)$	0.47
$\varepsilon_p(r_6)$	0.58
$\varepsilon_p(r_5)$	0.69
$\varepsilon_p(r_4)$	0.81
$\varepsilon_p(r_3)$	0.9
$\varepsilon_p(r_2)$	0.97
$\varepsilon_p(r_1)$	1

A snapshot of the magnitude of the computed electric field before and after passing through the lens is illustrated in Fig. 7. Similar to Fig. 3, this figure demonstrates the collimation of the beam after passing through the lens. Due to the reconfigurable nature of plasma, exciting the spherical MFE plasma lens increases the gain of the feed by approximately 6.5 dB, as illustrated in Fig. 8, while deactivating the lens cancels the focusing effect.

In summary, it is observed that using plasma dielectrics, a reconfigurable spherical MFE lens can be realized, although the distribution of the dielectric permittivity in the lens structure differs from conventional MFE lenses. In other words, the permittivity decreases from close to 1 at the center to 0.25 at the outer layer of the lens. Despite the significant difference in the values of refractive index or permittivity, a plasma-based MFE lens, similar to conventional MFE lenses, focuses on the radiated beam of the feed antenna.

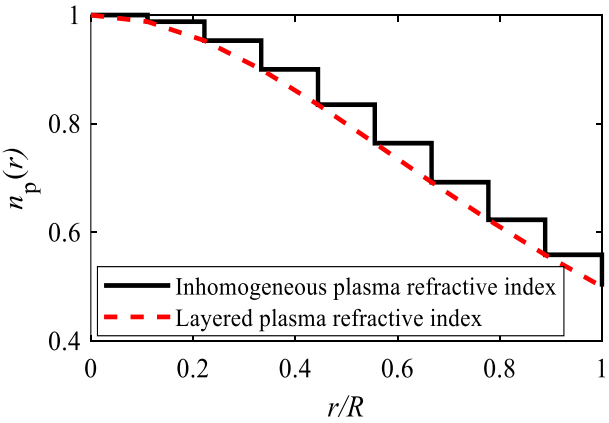

Fig. 6. Refractive index versus normalized radius of the plasma MFE lens.

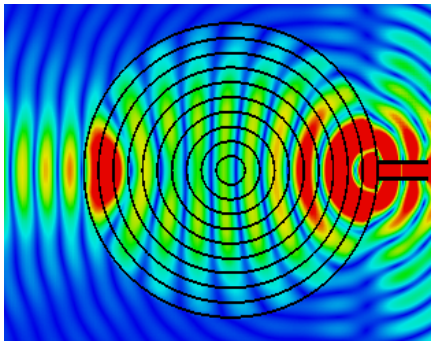

Fig. 7. Snapshot of numerical E-field distribution of the plasma MFE lens at f = 10 GHz.

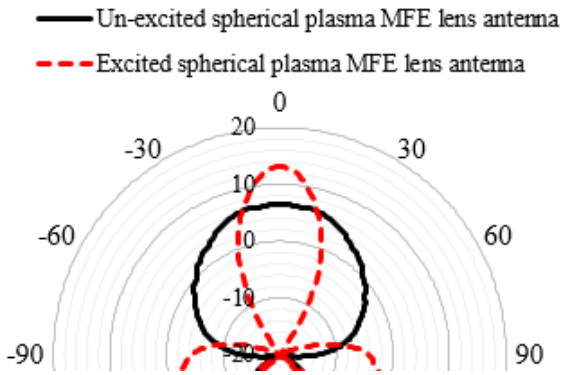

Fig. 8. Simulated gain of the spherical plasma MFE lens antenna at f = 10 GHz.

Now let us continue this section with a hemispherical plasma MFE lens. The structure comprises the waveguide feed, integrated with half of the ten-layer plasma-based spherical MFE lens designed in the previous step. The magnitude of the electric field before and after passing through the excited lens antenna, at the operating frequency of f = 10 GHz, is depicted in Fig. 9(a). Notably, by activating the plasma, the incident spherical wave transforms into a plane wave upon passing through the lens. Additionally, Fig. 9(b) presents a 3-D view of the simulated radiation pattern of this lens antenna.

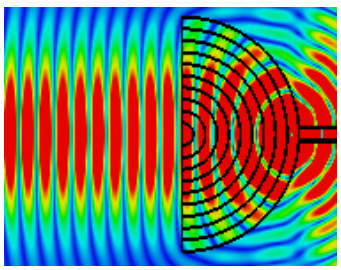

(a)

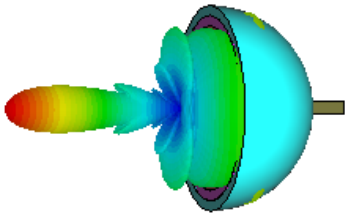

(b)

Fig. 9. (a) Magnitude of the electric field at 10 GHz before and after passing the hemispherical MFE plasma lens, (b) A 3-D view of the simulated radiation pattern of the hemispherical MFE plasma lens antenna.

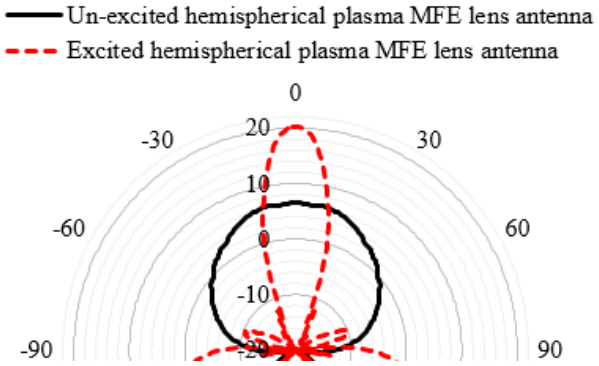

Fig. 10. Simulated gain of the hemispherical plasma MFE lens antenna at f = 10 GHz.

The simulation results reveal a gain of approximately 19.9 dBi with a half-power beamwidth (HPBW) of around 12 degrees for the lens antenna. Moreover, the proposed lens exhibits a 12.8 dBi enhancement in gain, focusing the beam effectively, as demonstrated in Fig. 10. When the plasma is deactivated, the gain of the antenna structure decreases to that of the gain of the feed. Hence, the lens antenna proves to be reconfigurable, possessing the capability to regulate radiation gain and, consequently, the beamwidth.

5. PARAMETRIC ANALYSIS

In this section, numerical simulations are conducted to evaluate the impact of varying the plasma bias characteristics on the performance of the proposed MFE lens. Furthermore, the effect of layer thickness within the lens is analyzed to determine the optimal number of layers for a constant lens radius.

First, we consider the ten-layer hemispherical plasma MFE lens designed in the previous section as the baseline antenna. The goal is to assess how

deactivating certain plasma layers affects the radiation characteristics, as the plasma layers can be independently switched ON or OFF. Concerning the layer numbering in Fig. 5(b), Fig. 11 illustrates that deactivating the inner layers leads to a reduction in radiation gain. For example, when all plasma layers are OFF, the antenna gain is 8 dBi. Activating only layer 10 increases the gain to 12.2 dBi, and further enhancement to 13.6 dBi is achieved when both layers 9 and 10 are ON. When all plasma layers are ON, the antenna achieves a maximum gain of around 19.9 dBi.

This demonstrates the ability to dynamically control the radiation characteristics by adjusting the bias of individual lens layers.

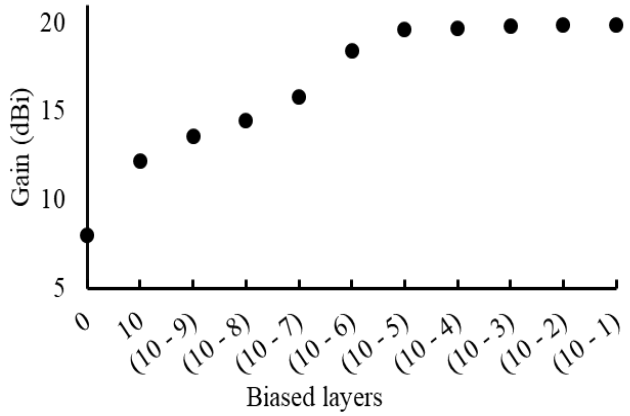

Fig. 11. Radiation gain as a function of the number of excited layers in the lens.

In the next step, the effect of layer thickness on the antenna's radiation characteristics is examined. It is evident that increasing the number of layers makes the lens behavior more like that of a truly inhomogeneous lens. However, reducing the number of layers simplifies the implementation. Therefore, a compromise must be made between optimizing radiation performance and minimizing implementation complexity.

As shown in Fig. 12, reducing the thickness of the layers increases the radiation gain. However, for thicknesses of $t = 5$ mm and $t = 10$ mm, the radiation gains are nearly identical. Therefore, selecting $t = 10$ mm can be considered the optimal layer thickness, offering a good compromise between performance and practicality.

In summary, the parametric analysis demonstrates that by controlling the plasma layers one can dynamically adjust the gain, with an optimal layer thickness of $t = R/10$ providing the best trade-off between gain and implementation simplicity.

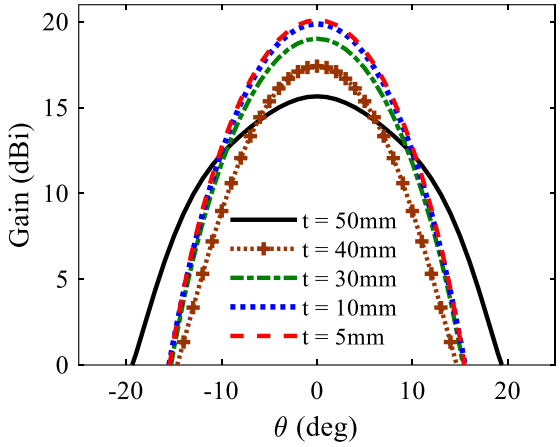

Fig. 12. Radiation gain of the lens antenna for various layer thicknesses in the plasma MFE lens.

6. CONCLUSION

This study investigated the feasibility and performance of utilizing plasma dielectric material within Maxwell Fish Eye (MFE) lens antenna structures for achieving reconfigurability. Through numerical simulations, it was demonstrated that plasma-based MFE lens antennas offer promising capabilities in dynamically tailoring radiation patterns and beam directions.

The unique refractive index profile of plasma dielectrics and their impact on MFE lens design and performance were highlighted. By incorporating plasma dielectric material, reconfigurable lens antennas capable of enhancing beam focusing and gain were shown to be feasible.

CONFLICT OF INTERESTS

No conflict of interest has been expressed by the authors.

REFERENCES

[1] L. Gunderson, "An electromagnetic analysis of a cylindrical homogeneous lens," *IEEE Transactions on Antennas and Propagation*, vol. 20, no. 4, pp. 476-479, 1972, https://doi.org/10.1109/TAP.1972.1140224.

[2] J. Liu, R. Mendis, and D. M. Mittleman, "A 2D Maxwell's fish eye lens using waveguide-based inhomogeneous artificial dielectrics," in *CLEO: 2013*, San Jose, California, USA, 2013, Art. no. CTh1k.3, Optica Publishing Group, https://doi.org/10.1364/CLEO_SI.2013.CTh1K.3.

[3] D. H. Werner, Z. Jiang, J. P. Turpin, and P. L. Werner, "Transformation optics collimating lenses for multi-beam antenna applications," in *4th IEEE International Symposium on Microwave, Antenna, Propagation and EMC Technologies for Wireless Communications*, Beijing, China, 2011, pp. 458-461, https://doi.org/10.1109/MAPE.2011.6156192.

[4] F. E. Helmy, I. I. Ibrahim, and A. M. Saleh, "Beam-steering of dielectric flat lens nanoantenna with elliptical patch based on antenna displacement for optical wireless applications," *Scientific Reports*, vol. 13, 2023, Art. no. 16030, https://doi.org/10.1038/s41598-023-43149-z.

[5] M. M. Taskhiri and S. Fakhte, "Broadband inhomogeneous lens with conical radiation pattern," *Scientific Reports*, vol. 13, 2023, Art. no. 12907, https://doi.org/10.1038/s41598-023-40024-9.

[6] H. F. Ma, B. G. Cai, T. X. Zhang, Y. Yang, W. X. Jiang, and T. J. Cui, "Three-dimensional gradient-index materials and their applications in microwave lens antennas," *IEEE Transactions on Antennas and Propagation*, vol. 61, no. 5, pp. 2561-2569, 2013, https://doi.org/10.1109/TAP.2012.2237534.

[7] J. Bor, B. Fuchs, O. Lafond, and M. Himdi, "Flat foam-based Mikaelian lens antenna for millimeter wave applications," in *44th European Microwave Conference*, Rome, Italy, 2014, pp. 1640-1643, https://doi.org/10.1109/EuMC.2014.6986768.

[8] B. Fuchs, O. Lafond, S. Rondineau, and M. Himdi, "Design and characterization of half Maxwell fish-eye lens antennas in millimeter waves," *IEEE Transactions on Microwave Theory and Techniques*, vol. 54, no. 6, pp. 2292-2300, 2006, https://doi.org/10.1109/TMTT.2006.875255.

[9] M. A. B. Abbasi, R. I. Ansari, G. G. Machado, and V. F. Fusco, "Design and analysis of Maxwell fisheye lens based beamformer," *Scientific Reports*, vol. 11, 2021, Art. no. 22739, https://doi.org/10.1038/s41598-021-02058-9.

[10] H. Lu, G. Wu, Y. Liu, and X. Lv, "A millimeter-wave fully metallic six-channel crossover based on Maxwell fish-eye lens," *IEEE Microwave and Wireless Components Letters*, vol. 30, no. 11, pp. 1041-1044, 2020, https://doi.org/10.1109/LMWC.2020.3027466.

[11] Q. Lei, R. Foster, P. S. Grant, and C. Grovenor, "Generalized Maxwell fish-eye lens as a beam splitter: A case study in realizing all-dielectric devices from transformation electromagnetics," *IEEE Transactions on Microwave Theory and Techniques*, vol. 65, no. 12, pp. 4823-4835, 2017, https://doi.org/10.1109/TMTT.2017.2727495.

[12] N. Muhamad Nadzir, M. Himdi, M. K. A. Rahim, N. A. Murad, O. Ayop, and O. Lafond, "Multi-beam luneburg lens with reduced size patch antenna," *Electronics*, vol. 12, no. 14, 32023, Art. no. 3028, https://doi.org/10.3390/electronics12143028.

[13] Y. Shi, K. Li, J. Wang, L. Li, and C. H. Liang, "An etched planar metasurface half Maxwell fish-eye lens antenna," *IEEE Transactions on Antennas and Propagation*, vol. 63, no. 8, pp. 3742-3747, 2015, https://doi.org/10.1109/TAP.2015.2438337.

[14] H. Lu, Z. Liu, Y. Zhang, K. Pang, and Y. Liu, "Partial Maxwell fish-eye lens inspired by the Gutman lens and Eaton lens for wide-angle beam scanning," *Optics Express*, vol. 29, no. 15, pp. 24194-24209, 2021, https://doi.org/10.1364/OE.426539.

[15] T. Tandel and S. Trapasiya, "Reconfigurable antenna for wireless communication: Recent developments, challenges and future," *Wireless Personal Communications*, vol. 133, no. 2, pp. 725-768, 2023, https://doi.org/10.1007/s11277-023-10785-7.

[16] S. Dubal and A. Chaudhari, "Mechanisms of reconfigurable antenna: A review," in *10th International Conference on Cloud Computing, Data Science & Engineering (Confluence)*, Noida, India, 2020, pp. 576-580, https://doi.org/10.1109/Confluence47617.2020.9057998.

[17] F. Sadeghikia, K. Zafari, M. R. Dorbin, M. Himdi, and A. K. Horestani, "Reconfigurable biconcave lens antenna based on plasma technology," *Scientific Reports*, vol. 13, 2023, Art. no. 9213, https://doi.org/10.1038/s41598-023-36332-9.

[18] M. O. Arend, F. C. C. D. Castro, C. Müller, and M. C. F. D. Castro, "Toroidal plasma lens antenna," *IEEE Antennas and Wireless Propagation Letters*, vol. 16, pp. 1155–1158, 2016, https://doi.org/10.1109/LAWP.2016.2625800.

[19] F. Sadeghikia, K. Zafari, M. Himdi, M. T. Noghani, and A. K. Horestani, "An advanced beamforming mechanism based on programmable plasma prisms," *IEEE Access*, vol. 12, pp. 182062-182072 2024, https://doi.org/10.1109/ACCESS.2024.3506821.

[20] H. Ja'afar, M. T. B. Ali, A. N. B. Dagang, H. M. Zali, and N. A. Halili, "A reconfigurable monopole antenna with fluorescent tubes using plasma windowing concepts for 4.9-GHz

application," *IEEE Transactions on Plasma Science*, vol. 43, no. 3, pp. 815-820, 2015, https://doi.org/10.1109/TPS.2015.2398878.

[21] F. Sadeghikia, M. Valipour, A. K. Horestani, M. Himdi, and T. Anderson, "Beam-steerable helical antenna using plasma reflectors," in *16th European Conference on Antennas and Propagation (EuCAP)*, Madrid, Spain, 2022, https://doi.org/10.23919/EuCAP53622.2022.9769604.

[22] F. Sadeghikia, A. K. Horestani, and M. Himdi, "Reconfigurable antennas based on plasma reflectors and cylindrical slotted waveguide," in *Plasma Science-Recent Advances, New Perspectives and Applications*, S. Singh. Ed. London, United Kingdom: IntechOpen, 2022, https://doi.org/10.5772/intechopen.108017.

[23] F. Sadeghikia, M. R. Dorbin, A. K. Horestani, M. T. Noghani, and H. Ja'afar, "Tunable inverted-F antenna using plasma technologies," *IEEE Antennas and Wireless Propagation Letters*, vol. 18, no. 4, pp. 702-706, 2019, https://doi.org/10.1109/LAWP.2019.2901354.

[24] J. Bazrafshan, F. Sadeghikia, A. K. Horestani, and M. Himdi, "A reconfigurable and steerable horn antenna using plasma dielectric slabs for controllable gain and beam steering," *Journal of Space Science and Technology*, vol. 17, no. 3, pp. 28-44, 2024, https://doi.org/10.22034/jsst.2024.1455.

[25] T. Anderson, "Antenna beam focusing and steering with refraction through a plasma," in *13th European Conference on Antennas and Propagation (EuCAP)*, Krakow, Poland, 2019, pp. 1-5.

[26] F. Sadeghikia, M. Valipour, M. T. Noghani, H. Ja'afar, and A. K. Horestani, "3D beam steering end-fire helical antenna with beamwidth control using plasma reflectors," *IEEE Transactions on Antennas and Propagation*, vol. 69, no. 5, pp. 2507–2512, https://doi.org/10.1109/TAP.2020.3031473.

[27] A. K. Horestani, M. T. Noghani, F. Sadeghikia, M. R. Dorbin, M. Valipour, and F. Martín, "Reconfigurable and frequency tunable inverted F antenna based on plasma technology," in *International Conference on Electromagnetics in Advanced Applications (ICEAA)*, Granada, Spain, 2019, pp. 1175-1177, https://doi.org/10.1109/ICEAA.2019.8879280.

[28] M. R. Dorbin, J. A. R. Mohassel, F. Sadeghikia, and H. B. Ja'afar, "Determination of the plasma density in a plasma antenna based on image analysis and LIVPD graphs," *IEEE Access*, vol. 11, pp. 120721-120727, 2023, https://doi.org/10.1109/ACCESS.2023.3327179.

[29] F. Sadeghikia and F. Hodjat Kashani, "A two element plasma antenna array," *Engineering, Technology and Applied Science Research*, vol. 3, no. 5, pp. 516–521, 2013, https://doi.org/10.48084/etasr.319.

[30] M. T. Noghani, A. K. Horestani, F. Sadeghikia, and M. R. Dorbin, "Theoretical modeling of resonant wavelength in 3-layered plasma antennas," *Waves in Random and Complex Media*, vol. 31, no. 6, pp.1587-1596, 2021, https://doi.org/10.1080/17455030.2019.1687959.

[31] M. Magarotto *et al.*, "Plasma antennas: A comprehensive review," *IEEE Access*, vol. 12, pp. 80468-80490, 2024, https://doi.org/10.1109/ACCESS.2024.3411142.

[32] S. H. Zainud Deen, H. A. E. A. Malhat, E. A. E. Refaey, and M. M. Badawy, "Genus plasma-based self-complementary reconfigurable intelligent metasurfaces," *Plasmonics*, vol. 19, pp. 2991-3001, 2024, https://doi.org/10.1007/s11468-024-02215-6.

[33] F. Sadeghikia, A. K. Horestani, M. R. Dorbin, M. T. Noghani, and H. Ja'afar, "A new feed network for the communication signal and excitation of surface-wave-driven plasma antennas," in *14th European Conference on Antennas and Propagation (EuCAP)*, Copenhagen, Denmark, 2020, pp. 1-4, https://doi.org/10.23919/EuCAP48036.2020.9135951.

[34] F. Sadeghikia, M. R. Doorbin, H. Ja'afar, A. K. Horestani, and M. T. Noghani, "An overview on the implementation of surface wave driven plasma antennas," in *IEEE Symposium on Wireless Technology & Applications (ISWTA)*, Shah Alam, Malaysia, 2021, pp. 53-57, https://doi.org/10.1109/ISWTA52208.2021.9587357.

[35] E. Koohkan, S. Jarchi, A. Ghorbani, and M. Bod, "Vortex beam generation based on plasma reflect-array surface at microwave frequencies," *IEEE Transactions on Plasma Science*, vol. 49, no. 7, pp. 2086-2092, 2021, https://doi.org/10.1109/TPS.2021.3083199.

[36] G. Mansutti, P. D. Carlo, M. Magarotto, M. A. Hannan, P. Rocca, and A. D. Capobianco, "Design of a hybrid metal-plasma transmit-array with beam-scanning capabilities," *IEEE Transactions on Plasma Science*, vol. 50, no. 3, pp. 662-669, 2022, https://doi.org/10.1109/TPS.2022.3149473.

[37] F. Sadeghikia, M. T. Noghani, and M. R. Simard, "Experimental study on the surface wave driven plasma antenna," *AEU-International Journal of Electronics and Communications*, vol. 70, no. 5, pp. 652– 656, 2016, https://doi.org/10.1016/j.aeue.2016.01.024.

[38] M. Born, and E. Wolf, *Principles of Optics: Electromagnetic Theory of Propagation, Interference and Diffraction of Light*, 6th ed. Cambridge University Press, 1980.

[39] D. S. Kulyabov, M. N. Gevorkyan, and A. V. Korolkova, "Software implementation of the Eikonal equation," in *VIII Conference Information and Telecommunication Technologies and Mathematical Modeling of High-Tech Systems*, Moscow, Russia, 2018.

JSST
Journal of Space Science and Technology

P-ISSN: 2008-4560
E-ISSN: 2423-4516

Journal of Space Science and Technology

Vol. 17, Special Issue, pp. 32-44, 2024
https://doi.org/10.22034/jsst.2024.1497
Journal Homepage: https://jsstpub.com

Original Research Paper

Detailed Algorithm for Implementing Circle Criterion in QFT Framework for Saturation Nonlinearity

Hamed Kashani*

Aerospace Research Institute, Ministry of Science, Research and Technology, Tehran, Iran

ARTICLE INFO

Article History:

Received 17 August 2024
Revised 22 September 2024
Accepted 06 October 2024
Available Online 19 October 2024

Keywords:

Robust control
Quantitative feedback theory saturation
Non-interfering architecture
Circle criterion

ABSTRACT

Controlling a spacecraft's orbit and attitude is one of the most complicated problems in control engineering. Engineers encounter uncertainty and nonlinearity due to large flexible appendages and saturated electromechanical or electrohydraulic actuators. Control design methods for dealing with such problems may involve many calculations. Matlab software automates many design methods in its control system toolbox, providing algorithms for systematically analyzing, designing, and tuning linear control systems. Many other advanced design methods must also be automated to achieve fast and accurate controller design for more complex control systems. As a sample, plant uncertainty, prevalent in space systems, requires robust consideration in the design process. Quantitative feedback theory (QFT), as a powerful method for addressing such complex issues, requires plenty of calculations that make it necessary for the method to be automated. A QFT design toolbox is developed by Tersoft company. However, this toolbox cannot treat some practical issues, such as actuator saturation in its design process. In the QFT framework, saturation can be dealt with by Horowitz architecture or noninterfering loop architecture, containing an inner loop around the saturation element in the control loop. The circle criterion is a critical constraint on the inner loop transfer function, ensuring stability. This paper presents a comprehensive algorithm for automating the process of obtaining inner loop compensator design constraints, with detailed flowcharts to facilitate software development. To verify the proposed algorithm, the boundary on the saturation loop compensator, H(s), for a hydraulic actuator is determined using computer codes implemented in the Matlab environment. Intermediate and final results are presented to follow the calculations step by step up. Finally, the validity of this boundary is checked by placing its points into the circle criterion's mathematical expression and observing if the resultant points fall outside the reference circle.

*Corresponding Author's E-mail: kashani@ari.ac.ir

How to Cite this Article:
H. Kashani, "Detailed algorithm for implementing circle criterion in QFT framework for saturation nonlinearity," *Journal of Space Science and Technology*, Vol. 17, Special Issue, pp. 32-44, 2024, https://doi.org/10.22034/jsst.2024.1497.

NOMENCLATURE

SYMBOL	DESCRIPTION
μ_1	Lower Limit Of Sector Nonlinearity
μ_2	Upper Limit Of Sector Nonlinearity
C	Plant Output
F	Prefilter Transfer Function
G	Loop Shaping Transfer Function
H	Inner Loop Compensator Transfer Function
$\mathcal{I}_C$	Imaginary Part Of Complex Number C
P	Plant Transfer Function
R	Reference Input
$\mathcal{R}_C$	Real Part Of Complex Number C
X	Input Of Saturation Element
Y	Output Of Saturation Element, Plant Input

1. INTRODUCTION

Aerospace systems are the most complex with various plant and environment nonlinearity and uncertainty complexities. Attitude and orbit control systems for uncertain plants, such as space systems with large flexible structures or their components such as nonlinear actuators, pose a quite challenging design problem in the presence of nonlinearities like actuator saturation [1-3].

One of the most powerful robust control design methods in the presence of plant uncertainty or nonlinearity is Quantitative Feedback Theory (QFT). At each frequency of interest, QFT imposes a boundary on the transfer function of the loop shaper, $G(s)$ [4]. However, in most practical problems, designing the transfer function $G(s)$ to shape the loop and determining the prefilter $F(s)$ to limit the system's frequency response within a desired boundary are not the final stages of the design process. Various practical issues, such as plant input saturation, can lead to instability and performance degradation. To address the absolute stability problem arising from saturation, the noninterfering architecture proposed in [5] can be employed. The circle criterion proves the absolute stability of this architecture.

As the stability and performance requirements impose boundaries on $G(s)$ in the first stage of design, the circle criterion determines some boundaries for $H(s)$ in the second stage of the design. Extracting the boundaries above from requirements typically involves a significant amount of calculations. Once the boundaries are determined, designing compensators that satisfy these boundaries also requires substantial effort.

The Matlab software automates many classical control design methods [6]. Terasoft company has developed a QFT toolbox that automates the boundary calculation in the first design step [7]. Furthermore, [8] proposes a method to automate compensator synthesis in the first design stage. This paper contributes to developing an algorithm for automating the calculation of absolute stability boundaries in the second design stage for saturating plant input.

In the next section, we briefly describe the suitable architecture within the QFT framework for addressing saturation in the loop. Ensuring stability under saturation using the circle criterion is introduced in section 3. The main contribution of this article is presented in section 4, which describes the algorithm for implementing the circle criterion in the QFT framework. In section 5, an illustrative example is used to examine the validity of the proposed algorithm. Finally, concluding remarks are presented in the last section of the paper.

2. LOOP ARCHITECTURE FOR TREATING SATURATION

The QFT framework has two main architectures for treating saturation to achieve the desired stability and performance. The first is based on Horowitz's opinion, which affects the design of $G(s)$ [9]. Another approach can be used to simplify the design process, consisting of two steps. In the first step, two controllers, $G(s)$ and $F(s)$, are designed using a common QFT design procedure, ignoring the saturation. In the second step, controller $H(s)$ is designed to reduce the undesired effects of plant input saturation. Fig. 1 shows this noninterfering architecture for addressing saturation in the plant input [10]. The term "noninterfering" is used because the compensator $H(s)$ is not active until the plant input saturates. According to this architecture, the loop transmission around the saturation element L_n can be written as follows.

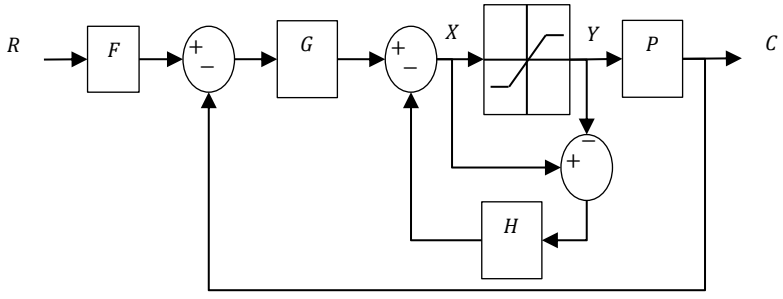

Fig. 1. Noninterfering control architecture [5].

$$L_n = -\frac{X}{Y} = \frac{L-H}{1+H} \quad (1)$$

Where, $L = GP$.

To ensure stability and achieve desired performance $H(s)$ must satisfy certain constraints [5]. In this article, only the circle criterion, a constraint associated with stability, is considered. The next section briefly explains the circle criterion, and readers can refer to reference [11] for more details.

2.1 Applying the Circle Criterion

In the scalar case, the circle criterion for a sector nonlinearity $N \in [\mu_1, \mu_2]$ with $\mu_2 > \mu_1$ states that the system presented in Fig. 1 is absolutely stable if the transfer function

$$Z(s) = \frac{1+\mu_2 L_n(s)}{1+\mu_1 L_n(s)} \quad (2)$$

is strictly positive real [11]. Strictly positive realness, at first, requires it is not identically zero. $Z(s)$ is identically zero if and only if $L_n(s) = -1/\mu_2$. This is a highly unusual scenario in practice because L_n is dynamic and depends on frequency. The second condition is that $Z(s)$ must be Hurwitz, and the third condition is expressed by Eq. (3).

$$\mathrm{Re}\left[\frac{1+\mu_2 L_n(j\omega)}{1+\mu_1 L_n(j\omega)}\right] > 0, \forall\omega \in \mathbb{R} \quad (3)$$

Now, there are three different cases depending on the sign of μ_1:

a) $0 < \mu_1 < \mu_2$,

b) $0 = \mu_1 < \mu_2$ and

c) $\mu_1 < 0 < \mu_2$.

In practice, saturation nonlinearity is typically categorized in case a, with the specific condition of $0 < \mu_1 < 1$. In this case, the third condition can be expressed as Eq. (4).

$$\mathrm{Re}\left[\frac{1+L_n(j\omega)}{\frac{1}{\mu_1}+L_n(j\omega)}\right] > 0, \forall\omega \in \mathbb{R} \quad (4)$$

Inequality (4) is equivalent to inequality (5), which can be proven by expressing $L_n = Re[L_n] + iIm[L_n]$ in inequality (4), simplifying the result, splitting the term $1/\mu_1 = 1/2\mu_1 + 1/2\mu_1$. By moving one of these terms to the right-hand side of the inequality, adding the term $(1/\mu_1^2 + 1)/4$ and finally, simplifying both sides of inequality leads to the following form of constraint.

$$\left|L_n(j\omega) + \frac{1/\mu_1 + 1}{2}\right| > \frac{1/\mu_1 - 1}{2} \quad (5)$$

Fig. 2 depicts the graphical representation of inequality (5) in the Nyquist plane and illustrates that the circle criterion necessitates that L_n does not penetrate region D. In this figure, the vectors r_1 and r_2 are equal to $1/\mu_1 + L_n\,(j\omega)$ and $1 + L_n(j\omega)$, respectively.

Although local absolute stability is guaranteed under $H(s)$ with circle criterion satisfaction, it is still possible for limit cycles to occur, especially when the plant has a high type (i.e., $n \geq 3$) [12]. To address this issue, the describing function method can be used. This paper, however, only considers local absolute stability.

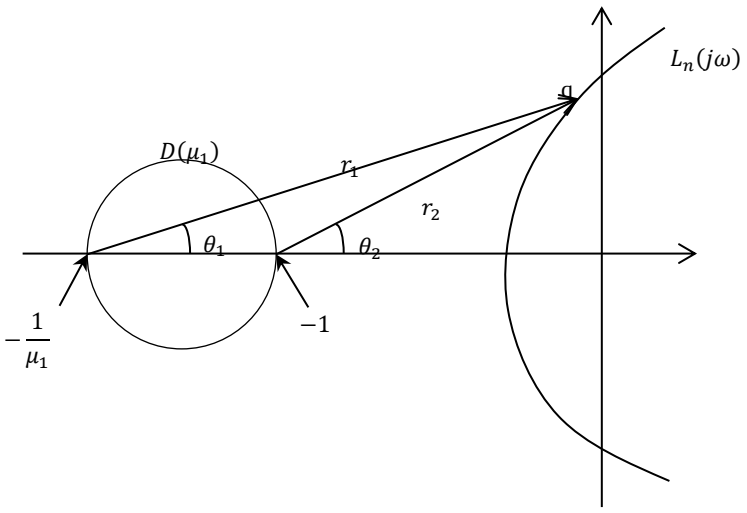

Fig. 2. Graphical representation of the circle criterion [11].

Since the other element affecting L_n, i.e., the linear loop transmission L, has already been determined; the focus now is on designing the compensator H such that L_n satisfies the circle criterion. By introducing the $\eta =$

$(1/\mu_1 + 1)/2$ and $\kappa = (1/\mu_1 - 1)/2$ and expressing L_n in terms of the real component "$\mathcal{R}$" and the imaginary component "$\mathcal{I}$", Eq. (5) may be reformulated as the following inequality.

$$\mathcal{I}_{L_n}^2 > \kappa^2 - \left(\mathcal{R}_{L_n} + \eta\right)^2 \tag{6}$$

Substituting of $\mathcal{R}_{L_n}$ and $\mathcal{I}_{L_n}$ from Eq. (1) and simplifying the resulting expression leads to inequality (7), which defines the admissible region for H in the Nyquist plane.

$$\begin{cases} \mathcal{I}_H > \mathcal{A}\mathcal{R}_H - \mathcal{B}; & \mathcal{I}_L > 0 \\ \mathcal{I}_H < \mathcal{A}\mathcal{R}_H - \mathcal{B}; & \mathcal{I}_L < 0 \end{cases} \tag{7}$$

where, $\mathcal{A} = -(1 + \mathcal{R}_L)/\mathcal{I}_L$ and $\mathcal{B} = -\left((1 + \mathcal{R}_L)(1 + \mu_1\,\mathcal{R}_L) + \mu_1\,\mathcal{I}_L^2\right)/\left(\mathcal{I}_L(1 - \mu_1)\right)$. The inequalities (7) are linear, and their parameters i.e., slope $\mathcal{A}$ and vertical intercept $\mathcal{B}$, are functions of linear loop transmission and μ_1. In plants with uncertainty, $\mathcal{A}$ and $\mathcal{B}$ may vary in certain ranges. Inequality (7) must be satisfied for all possible plant parameters. Each pair of plant parameters defines a line in the Nyquist plane, and the first and second inequalities of Eq. (7) correspond to the regions above and below the line $\mathcal{I}_H = \mathcal{A}\mathcal{R}_H - \mathcal{B}$, respectively. Fig. 3 illustrates the overall boundaries that express the constraint resulting from all possible plant parameters.

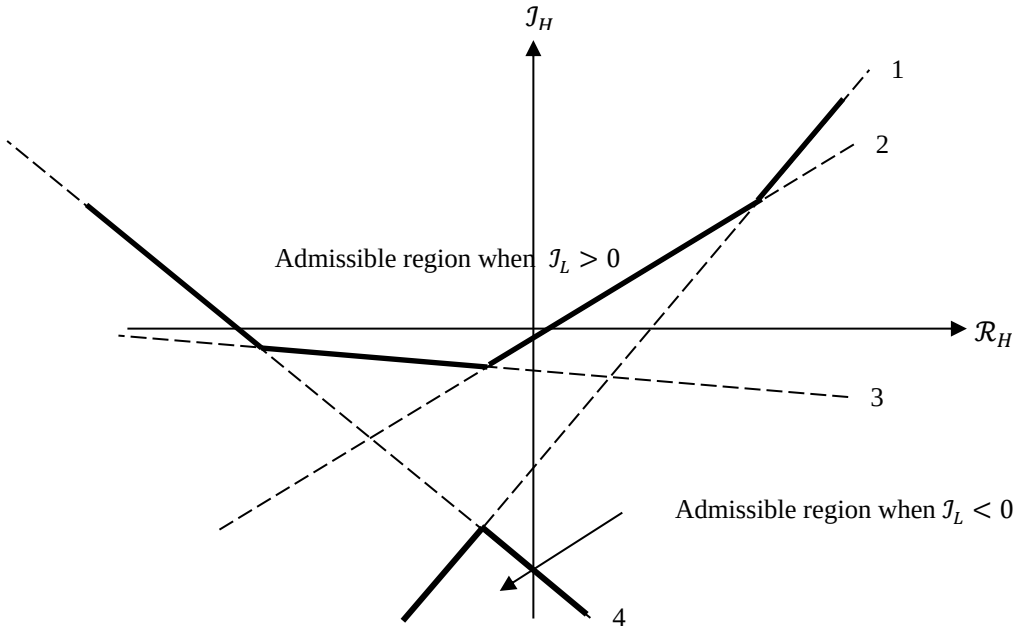

Fig. 3. Schematic representation of circle criterion constraint on H in Nyquist plane.

A common approach for compensator design in the QFT framework is to express the constraints in Nichols plane, simplifying the design process and making it more intuitive. Section 4, which is the main contribution of this paper, addresses the algorithm for mapping the constraints from Nyquist to Nichols plane.

3. ALGORITHM FOR MAPPING THE ADMISSIBLE REGION FROM THE NYQUIST TO THE NICHOLS PLANE

At first glance, the transformation of boundaries expressing the circle criterion constraint from the Nyquist plane to the Nichols plane may seem simple. However, as seen in the following paragraphs, this process has some details worth examining. Firstly, how can the overall boundary be calculated in the Nyquist plane?

3.1 Overall boundary determination in the Nyquist plane

To calculate the overall boundary that satisfies the circle criterion for all possible plant variants in the Nyquist plane, the process should start from one end of the overall boundary schematically shown in Fig. 3. Here; the left side is selected. The upper boundary begins with the steepest lines at both ends, with the most negative slope on the left and the most positive slope on the right. If the lower boundary is applicable, the signs of slopes are switched.

The algorithm starts with the sorting of slope and vertical intercept of lines in two separate row vectors

$\boldsymbol{A} = \{a_i\}_{1\times n_l}$ and $\boldsymbol{B} = \{b_j\}_{1\times n_l}$, respectively, with descending/ascending order based on upper/lower boundary slopes. Here, n_l is the number of plant variants. Next, two matrices are defined as $\boldsymbol{X} = [\infty]_{n_l\times n_l}$ and $\boldsymbol{Y} = [0]_{n_l\times n_l}$ as initial values of abscissa and ordinate of all intercepts of each line pair, these matrices will be filled with true values according to Eq. (8).

$$\begin{cases} x_{ij} = -(b_i - b_j)/(a_i - a_j) \\ y_{ij} = a_i x_{ij} + b_i \end{cases} \quad ; \quad i \neq j \tag{8}$$

Sorting the lines based on their slopes, the pair of first columns of matrices X and Y contain the intercepting points of the line with the most negative slope/most positive slope with other lines. Referring to Fig. 3, starting from $x = -\infty$ and sliding along the steepest applicable line draws the first part of the overall boundary up to the first intercepting point. The coordinate of this point is expressed by the smallest element of the first column of X and its corresponding pair in the matrix Y with the same position (i_1, j_1). The next line on the overall boundary is the one that creates the first intercept in conjunction with the line of the most negative slope. Hence, the second line on the border corresponds to i_1th column in matrices X and Y. Sliding along this line up to the next intercept. The abscissa of this point is expressed by the smallest element of the column i_1th of matrix X, which is larger than $X(i_1, j_1)$. Its ordinate is the corresponding pair in matrix Y with the same position (i_2, j_2). This process is continued until reaching the line with the most positive slope/ most negative slope and sliding along it to $x = +\infty$.

3.2 Mapping a line from the Nyquist plane onto the Nichols plane

As explained initially, Nichol's chart facilitates compensator design, especially in the QFT framework. Therefore, the transformation of the borders from the Nyquist plane to the Nichols plane is discussed here. As observed, the overall boundary of the circle criterion in the Nyquist plane is a piecewise linear function. Therefore, the first step in mapping is to understand the projection of a line from the Nyquist plane to Nichol's plane. The projection of a general line from the Nyquist plane to the Nichols plane is a U-shaped curve with an aperture of 180°. Its deepest point's ordinate is equal to the distance of the line from the origin of the Nyquist plane on dB scale. The axis of symmetry of the curve lies at an angular position that is identical to the angle of the normal to the line from the origin of the Nyquist plane concerning the real axis. Phase angle in Nichols plane usually spreads in the domain of $-360° \le \phi \le 0$ or $-180° \le \phi \le 180°$. By definition, absolute gain or modulus ρ is assumed to be positive. Taking a left-hand side plot in Fig. 4 as an example (a1), when a radial beam sweeps the Nyquist plane from $\phi = -360°$, there is no intercept with a boundary line up to $\varphi = -2\pi + \tan^{-1} a$ where a is the slope of the boundary line.

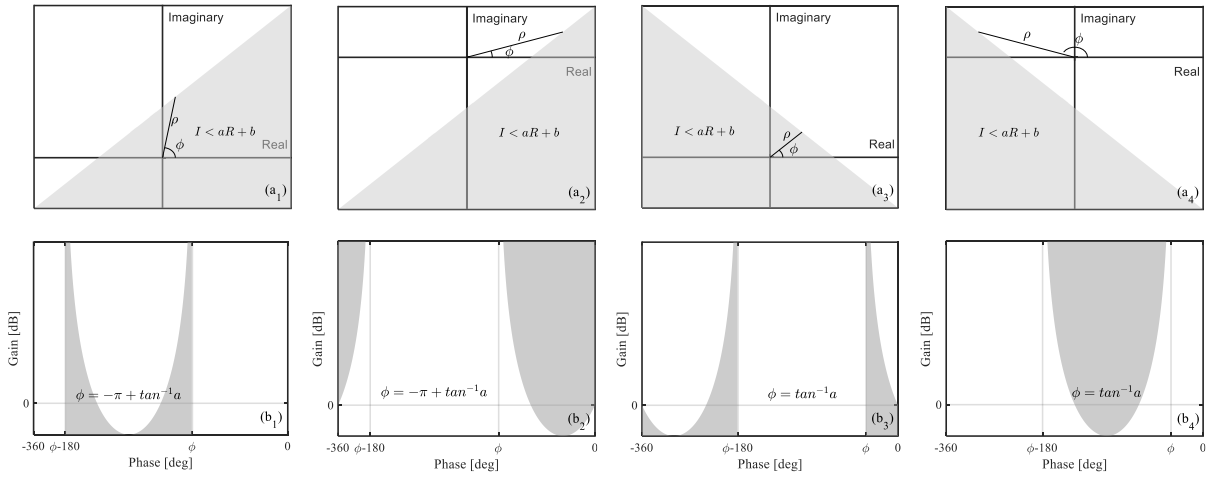

Fig. 4. Graphical representation of the mapping of a region specified by a line from the Nyquist plane to the Nichols plane for $\mathcal{I}_L < 0$.

From φ up to $\varphi + 180°$, the modulus reduces from $+\infty$ to a minimum value as described above and then increases back up to $+\infty$. This mapping is presented in the right-hand side plots of Fig. 4, for example, (b1). Therefore, in the Nichols plane, some part of the phase axis corresponding to negative modulus values will not contribute to the domain of the mapped boundary.

Depending on the sign of the slope and vertical intercept of the boundary line in the Nyquist plane, the mapped boundary in the Nichols plane shifts along the phase axis. The first row of Fig. 4 corresponds to the boundary line with positive slope and positive vertical intercept. The subsequent rows are associated with the other slope and vertical intercept sign combinations. In

these cases, mapping the boundary line from the Nyquist plane to the boundary curve in the Nichols plane can be explained as it was done for the first row. When the boundary line passes through the origin of the Nyquist plane, its projection onto the Nichols plane is a vertical line at the phase angle of $\tan^{-1} a$.

3.3 Mapping the admissible region from the Nyquist plane onto the Nichols plane

After mapping the boundary line from the Nyquist plane to the Nichols plane, the gray region above/below it that is admissible for H as imposed by the first/second part of the condition (7), associated with the linear loop transmission with a positive/negative imaginary part i.e., $\mathcal{I}_L > 0$ / $\mathcal{I}_L < 0$ should be determined on the Nichols plane. When $\mathcal{I}_L < 0$, as seen in the first row of Fig. 4, for H to be in the gray region of the plot (a1), the absolute magnitude of H should be smaller than ρ. Therefore, the admissible region for $\|H\| \triangleq 20 \log |H|$ will be below the boundary curve in the Nichols plane, as shown in plot (b1). With a positive slope and negative vertical intercept, $|H| \geq \rho$ is required for H to be in the gray region of the plot (a2), and consequently, the admissible region is above the boundary curve. Plot (b2) shows this region. The third and fourth rows of Fig. 4 can be explained similarly. When, $\mathcal{I}_L > 0$, a similar explanation is applicable.

3.4 Flowchart representation of the circle criterion implementation algorithm

This section considers the algorithm for implementing the abovementioned process, using flowcharts to provide a straightforward guide for writing computer codes. The linear design phase leads to the loop transmission $L(j\omega)$, which, for the domain of variations of system parameters in a desired frequency range, constructs a $n_\omega \times n_l$ matrix, where n_ω is the number of design frequency points. According to formulation in section 3, this matrix, together with μ_1, which is the lower limit of section nonlinearity saturation, are the inputs of the algorithm. The first step of the algorithm prepares the slope and vertical intercept of all boundary lines related to all possible plant variants the designer considers. At this step, the vectors of slopes and vertical intercepts are sorted in descending/ascending order based on the slopes vector, according to the applicability of the first/second inequalities in Eq. (7), as shown in Fig. 5.

In the next step, finding all the intersecting points is shown in the flowchart in Fig. 6. Sorted vectors of slopes and vertical intercepts are the inputs to this algorithm step. The abscissa and ordinate of intersecting points are gathered in two $n_l \times n_l$ matrices $\boldsymbol{X}$ and $\boldsymbol{Y}$, respectively. The element in the position of the ith row and jth column of these matrices indicates the coordinate of the intersecting point of line ith and line jth. The main diagonal elements are set at the right end of the real axis. A schematic representation of matrix $\boldsymbol{X}$ is shown in Fig. 7.

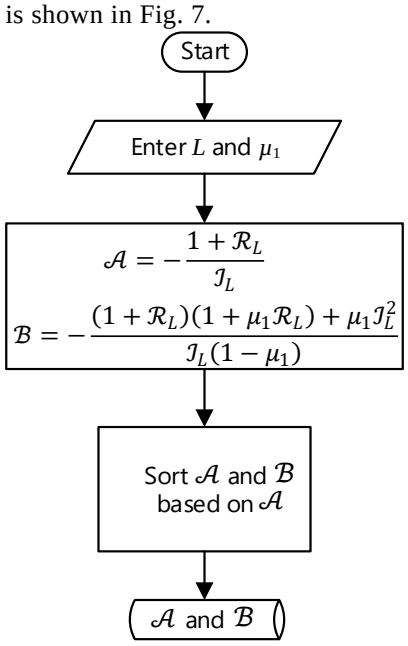

Fig. 5. Flowchart for preparing sorted vectors of the slopes and. vertical intercepts.

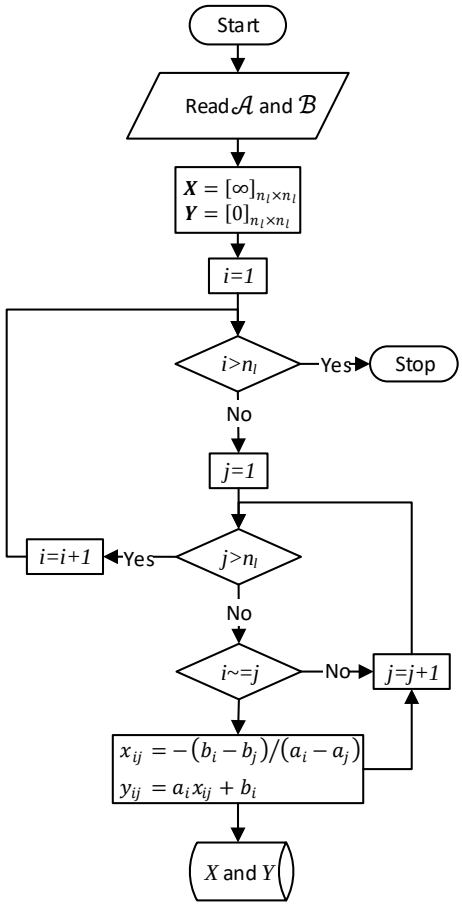

Fig. 6. Flowchart for finding all the intercept points.

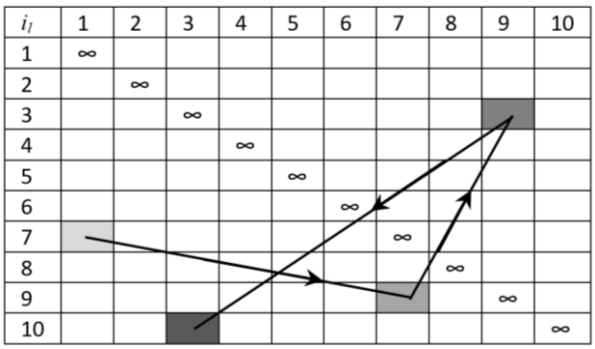

Fig. 7. Graphical representation of finding intersecting points on the overall boundary using matrix ***X*.**

The flowchart in Fig. 8 can be used to find intersection points on the overall boundary. From the left of the Nyquist plane, the most negative slope/most positive slope line begins the overall boundary. The first column of matrix ***X*** in Fig. 7 corresponds to this line. Sliding along this line up to the first intercept is associated with the smallest column element. This element is indicated by the lightest gray color in Fig. 7. The row number of this element is associated with the index of the next line, constructing the overall boundary. For the example shown in Fig. 7, row 7 is associated with the first intersection; consequently, line 7, represented by column 7, is the second constructing line of the overall boundary.

Again, sliding along this line leads to the next intersecting point on the overall boundary, shown by a slightly darker gray cell than the previous cell in schematic Fig. 7. The abscissa of this point is the smallest element of this column that is greater than the abscissa of the previous point. To satisfy this condition, the previous point's abscissa is subtracted from all elements of the recent column. Therefore, the row number of the smallest positive element in the changed-pivot column is associated with the index of the next line on the overall boundary. This process continues until the line with the most positive/negative slope is reached, as shown graphically in Fig. 7 using arrows and gradually darkening cells in the schematic representation of matrix ***X***. Fig. 8 can be used to develop the computer code.

At the end of this step, the coordinates of breakpoints on the overall boundary and the index of lines on this boundary are available. Provide the coordinate of the breaking points, the line with the most negative slope/most positive slope, and the line with the most positive slope/ most negative slope at the left and right of the overall boundary, entrance, and exit angles to and from each part of the boundary between two successive breaking point or entrance and exit angles to or from most right or most left part of the overall boundary can be calculated. The flowchart presented in Fig. 9 illustrates this process.

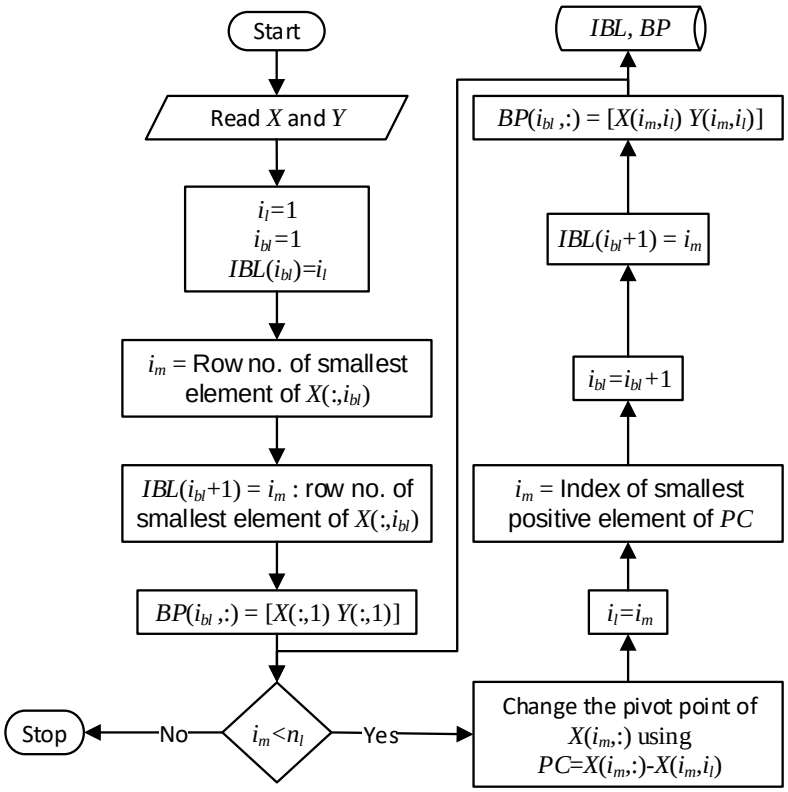

Fig. 8. Flowchart for finding intersecting points on the overall boundary using matrix ***X*.**

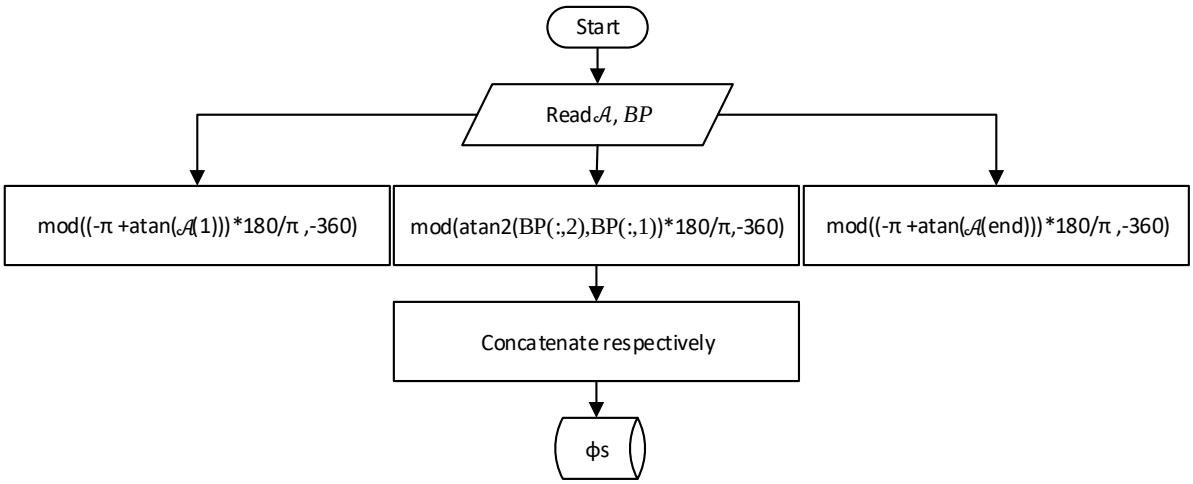

Fig. 9. Flowchart for calculating the entrance and exit angles to and from each part of the overall boundary.

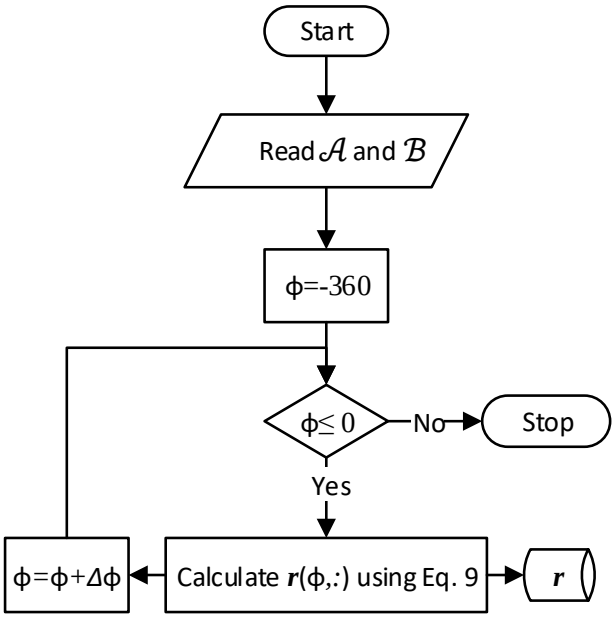

Fig. 10. Flowchart for calculating the gain associated with the lines that contribute to the overall boundary in the absolute scale.

The variable BP contains the coordinates of the breakpoints. The flowcharts in this paper use MATLAB functions and notations for brevity. The command "$\mathrm{mod}(\theta, -360)$" maps any angle θ in the range of $[-360°, 0°]$. The command "$\theta = \mathrm{atan}(y/x)$" calculates $\theta \in [-\pi/2, \pi/2]$ and the command "$\theta = \mathrm{atan2}(y, x)$" calculates $\theta \in [-\pi, \pi]$.

Up to this point, the required data for transferring the overall boundary from the Nyquist plane to the Nichols plane has been calculated. The final step is dedicated to the transformation. In this step, after transforming the boundary, it will be determined which side of the boundary is admissible for designing compensator H.

By sweeping a radial beam in the Nyquist plane from $-360°$ to $0°$, when it intersects with the overall boundary, the upper or lower limit of $|H|$, i.e., ρ, is equal to the length of the beam that can be calculated as follows.

$$\rho = \frac{\mathcal{B}(IBL)}{\sin \Phi - \mathcal{A}(IBL) \cos \Phi} \tag{9}$$

Here, Φ is the phase vector in the domain of $[-360°, 0°]$ with a desired interval of $\Delta\phi$ and $\phi \in \Phi$ in the flowchart of Fig. 10 that calculates the modulus associated with the lines contributing to the overall boundary at each phase angle ϕ. IBL is a vector that contains the indices of the lines contributing to the construction of the overall boundary.

Now, noncontributing parts of each line must be eliminated from the overall boundary in the Nichols plane. To achieve this, eight different conditions should be considered, as shown in Fig. 11. As seen in this figure, from the left-hand side, the first and third situations in the first row and the second situation in the second row have an interesting range of phase angle determined by inequalities in the reverse direction of other situations.

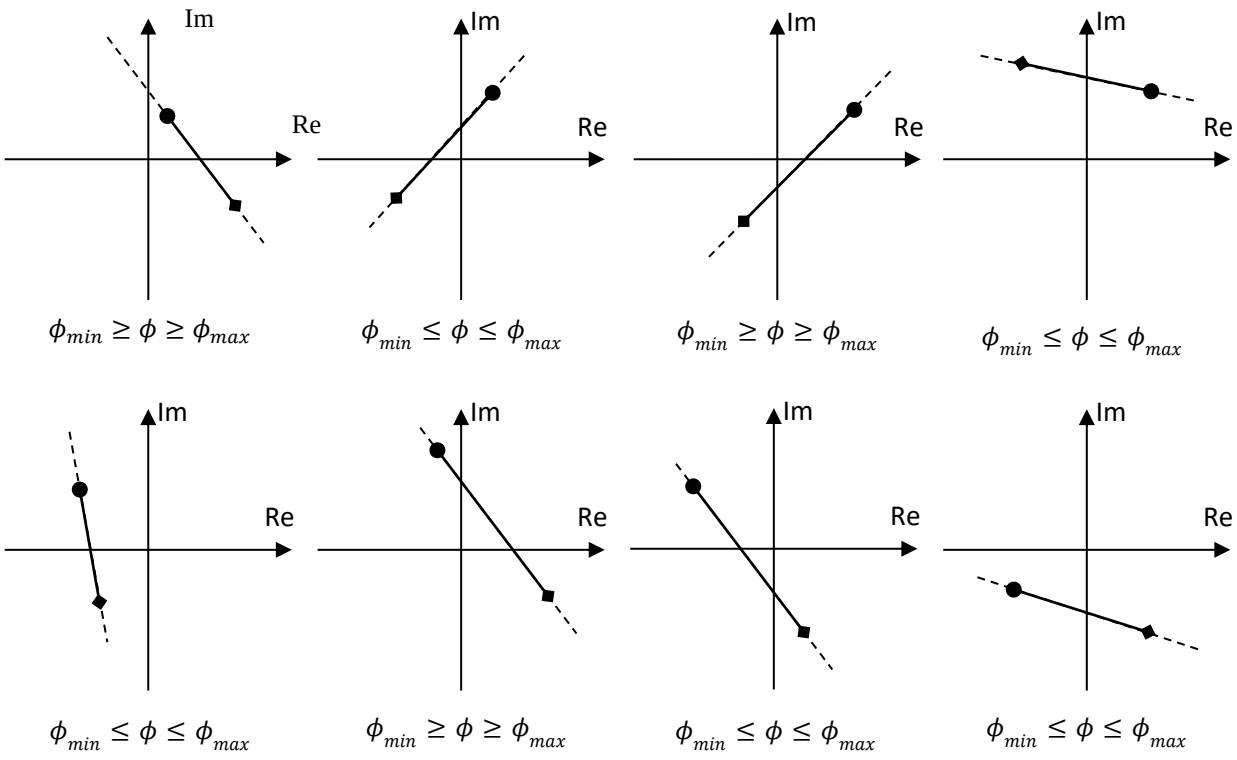

Fig. 11. Angle range of interest in the various conditions of vertical intercept and entrance and exit angles, ϕ_min and ϕ_m ax denoted by • and ■, respectively.

According to the above discussion, the flowchart in Fig. 12 provides the overall boundary of the admissible modulus of $H(j\omega)$ in the dB scale for the angle range of interest. In this flowchart, n_L is the number of lines that contribute to constructing the overall boundary, and ϕs is provided by the flowchart in Fig. 9. Here, NaN (i.e., not a number) is borrowed from Matlab software.

The final stage of the process is determining which side of the overall boundary is admissible. According to Eq.(7), if the linear loop transmission, which is the result of the first design step, has an imaginary part that satisfies $\mathcal{J}_L < 0$ by returning to Fig. 4, the admissible value for $H(j\omega)$ in the Nichols plane is $|H(j\omega)| \leq \rho$ if the vertical intercept of the associated line in the Nyquist plane is positive and vice versa. On the contrary, if the resultant loop transmission from the first design step has an imaginary part that satisfies $\mathcal{J}_L > 0$ by returning to Fig. 4, the admissible value for $H(j\omega)$ in the Nichols plane is $|H(j\omega)| \geq \rho$ if the vertical intercept of the associated line in the Nyquist plane is positive and vice versa.

After describing the algorithm, an example is solved, and its results are presented step by step to illustrate the process and validate the algorithm.

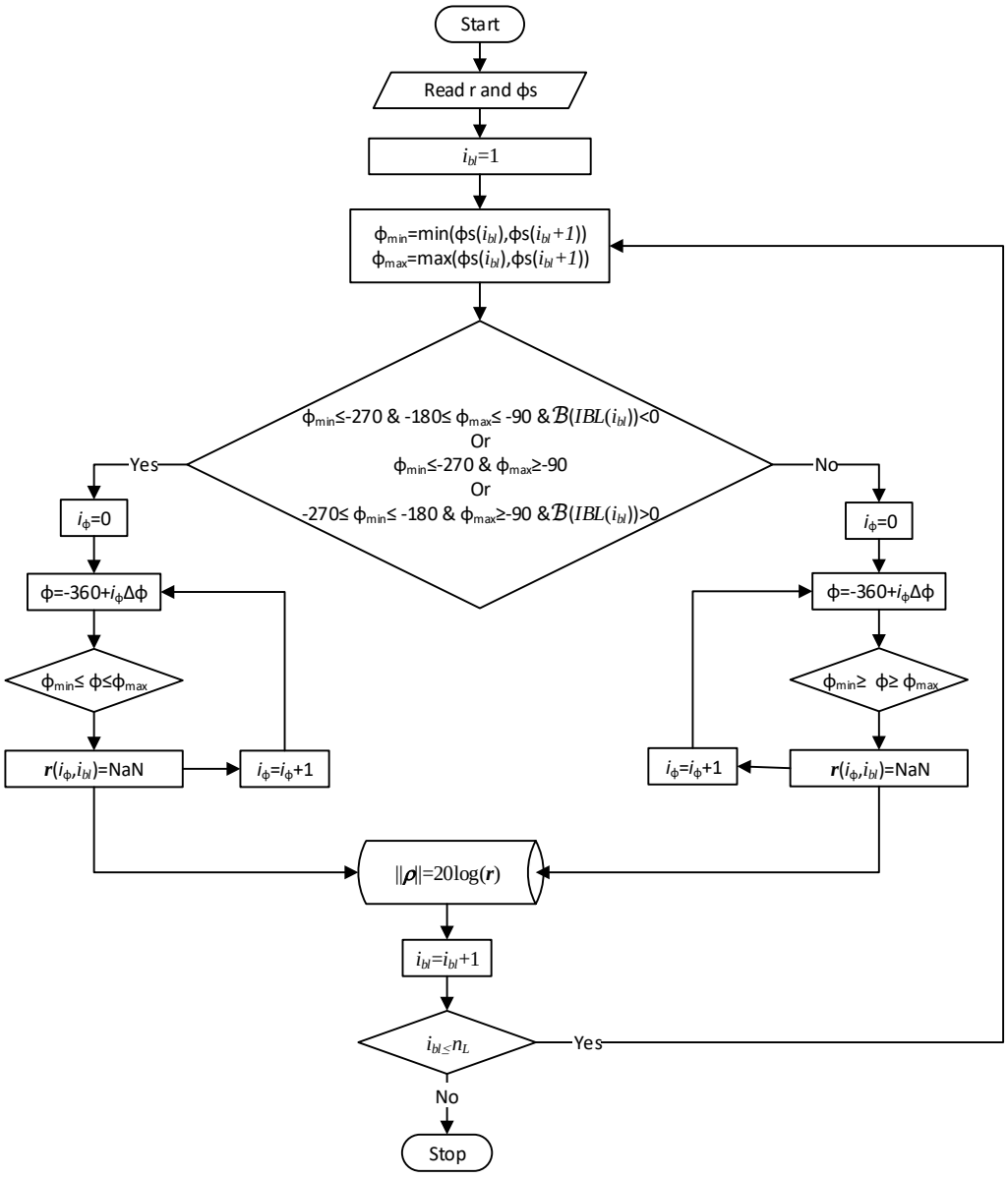

Fig. 12. Finalizing the boundary of the admissible modulus of $H(j\omega)$ for representation in the Nichols plane.

4. EXAMPLE AND ALGORITHM VERIFICATION

A wide variety of actuators, such as electromechanical, electromagnetic, and electrohydraulic types, are used is space applications. To examine the validity of the proposed algorithm, an electrohydraulic actuator is considered here. The transfer function of a hydraulic actuator, given by Eq. (10), is a customized form employed in [13], with inertial terms ignored and some differences in the numerical values of parameters. This transfer function, with actuator force as the output and the excitation voltage as the input, is used for the algorithm verification process. Saturation reflects itself in this plant as the limitation of the excitation voltage to 24 v.

$$P = \frac{K_s(A_i + A_o)}{R} \frac{(d + d_e)s + k_e}{D_3 s^3 + D_2 s^2 + D_1 s + D_0} \tag{10}$$

where,

$$\begin{aligned} D_0 &= K_p k_e \\ D_1 &= A_i^2 + A_o^2 + K_p(d + d_e) + Ck_e + k_e K_p \tau \\ D_2 &= \left(A_i^2 + A_o^2\right)\tau + \left(C + K_p \tau\right)(d + d_e) + Ck_e \tau \\ D_3 &= C(d + d_e)\tau \end{aligned} \tag{11}$$

and $A_i = 855\ mm^2$, $A_o = 428\ mm^2$, $d = 200\ Ns/m^2$, $d_e = 100\ Ns/m^2$ and R=28 Ω represente the piston's extending side area, retracting the piston, retracting side area of the piston, damping coefficient of cylinder-piston contact region, damping coefficient of load and electrical resistance of proportional valve solenoid, respectively. The other parameters vary in the range listed in Table 1.

Table 1. Nominal value and variation range of the plant parameters**.**

Parameter	Description	Nominal value	Range
k_e	Load stiffness	$5 \times 10^5 [N/m]$	[267,985000]
K_i	Flow rate sensitivity to excitation current	$1.5 \times 10^{-3} [m^3/As]$	$[1,2] \times 10^{-3}$
K_p	Flow rate sensitivity to pressure difference	$-65 \times 10^{-12}\ [m^2/sPa]$	$[-65,2650] \times 10^{-12}$
C	Flow rate sensitivity to pressure rate	10.7×10^{-15}	$[8.56,12.83] \times 10^{-15}$
τ	Solenoid time constant	$22.5\ ms$	[20,25]

As the first stage of the design process, the nominal values listed in this table are used to shape the loop using the QFT method, which results in the following transfer function for the loop transmission $L_0 = GP_0$. Details of this design stage are not presented for brevity, and readers can refer to [13] for more information.

$$L_0 = 10^7 \frac{7.2s^3+6.7\times10^2 s^2+1.7\times10^4 s+4.4\times10^4}{s^5+4\times10^4 s^4+10^6 s^3+2.6\times10^7 s^2+1.3\times10^7 s} \quad (12)$$

The degrees of the numerator and denominator of L are the same as those as L_0, but their coefficients vary depending on changes in the plant parameters. Assuming only the lower and upper limits of parameter variations listed in Table 1, there are 32 possible plant variants. H must be designed to satisfy the circle criterion for all variants. To examine the algorithm, $L_{n_\omega \times n_l}(j\omega)$ and $\mu_1 = 0.001$ are used in this example. By implementing the flowcharts shown in Fig. 5, Fig. 6, and Fig. 8 for frequencies $\omega = 0.1\ rad/s$, $\omega = 50\ rad/s$ and $\omega = 600\ rad/s$, boundaries related to each variant of the plant are obtained. These boundaries are shown as dotted lines in Fig. 13. To ensure that the circle criterion is satisfied for all plant variants, H must be designed accordingly.

The solid lines in the first row of Fig. 13 represent the overall boundary that satisfies this condition, while the downward-filled triangles along the border indicate the region of admissibility. The Nyquist plane data for the boundary is used as input for the flowcharts shown in Fig. 9, Fig. 10, and Fig. 12 to obtain the admissible region in the Nichols plane. The outputs, i.e., the boundaries on $|H|dB \triangleq \|H\|$ (represented by CCB), are presented in the second row of Fig. 13, with lower and upper limits indicated by black and gray colors, respectively.

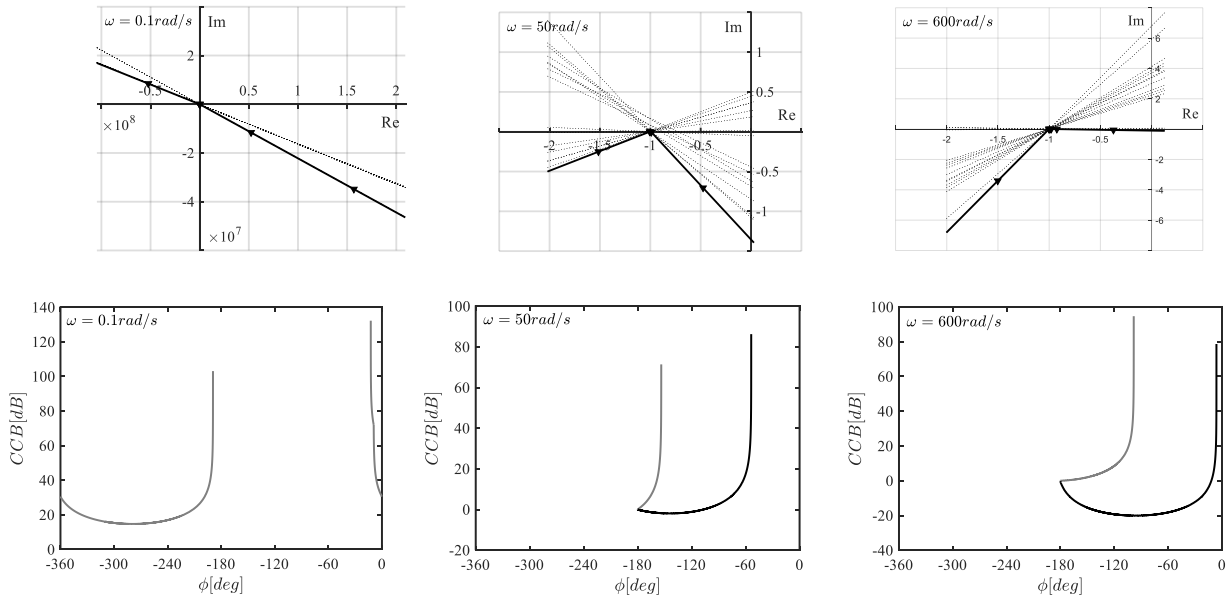

Fig. 13. Circle criterion boundaries for 3 selected frequencies, top plots: Nyquist representation, bottom plots: Nichols representation.

If $H(j\omega)$ is designed to fall within the admissible region of the Nyquist or Nichols planes, as shown in Fig. 13, then loop transmission around the saturation element, $L_n(j\omega)$, will not penetrate the circle centered at $(-(-1-1/\mu_1)/2\,,0)$ with a radius $(-1+1/\mu_1)/2$ in the Nyquist plane.

For validation, breaking points of the overall boundary in the Nyquist plane are selected as testing points and employed to generate associated points on $L_n(j\omega)$ according to Eq. (1). For all variants of plant at 16 frequencies in the band $0.1\ rad/s \le \omega \le 600\ rad/s$, $L_n(j\omega)$ scatters in the Nyquist plane, as shown in Fig. 14. In part (a) of this figure, all points associated with all plant variants at 16 frequencies are presented. However, due to scale inconsistency, the circle of criterion is not visible in this part of the figure. Part (b) of this figure presents a magnified view of part (a) in the vicinity of the circle of criterion. As seen, there is no scattering of points in the region within the circle of criterion. This region is considered the forbidden region because the transfer function of the closed-loop system becomes unstable if the loop transmission around the saturation element penetrates this region. The absence of scattering in the forbidden region indicates that the algorithm properly calculates the overall boundaries.

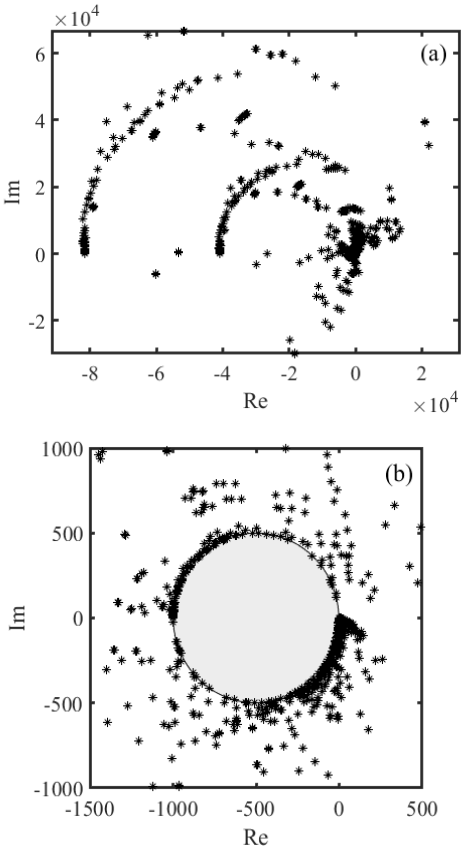

Fig. 14. Examining the algorithm by direct check using the circle of criterion in the Nyquist plane.

5. CONCLUSION

QFT is a powerful, robust tool for designing controllers in the presence of plant uncertainty and input saturation, which are prevalent in space systems and components. One approach to achieve this is using noninterfering architecture, where a robust linear controller is first designed through loop shaping and prefiltering, ignoring saturation. Then, a loop is constructed around the saturation element to mitigate its undesired effects, and robust stability depends on satisfying the circle criterion.

However, the computational cost of calculating the boundaries of the circle criterion makes automation necessary. This paper provides a detailed algorithm for implementing the circle criterion in practice, using flowcharts to facilitate computer code generation.

An example demonstrates the algorithm, with intermediate and final results provided to track the process. Finally, direct validation confirms that the calculated overall boundary satisfies the circle criterion.

CONFLICT OF INTERESTS

No conflict of interest has been expressed by the author.

REFERENCES

[1] C. Wen Hua, "QFT design for spacecraft with uncertain flexible structures," in *6th World Congress on Intelligent Control and Automation*, Dalian, China, 2006, pp. 8191-8195, https://doi.org/10.1109/WCICA.2006.1713571.

[2] M. V. Chitra, K. K. Sharma, and A. A. Kumar, "Quantitative feedback theory based robust control design for a flexible luanch vehicle," in *International Conference on Control, Communication, and Computing India (ICCC)*, Trivandrum, India, 2015, pp. 72-77, https://doi.org/10.1109/ICCC.2015.7432872.

[3] M. Garcia-Sanz, I. Eguinoa, M. Barreras, and S. Bennani, "Nondiagonal MIMO QFT controller design for Darwin-type spacecraft with large flimsy appendages," *Journal of Dynamic Systems, Measurement, and Control*, vol. 130, no. 1, 2008, Art. no. 011006, https://doi.org/10.1115/1.2807067.

[4] C. H. Houpis, S. J. Rasmussen, and M. Garcia-Sanz, *Quantitative Feedback Theory: Fundamentals and Applications*, 1st ed. Boca Raton, FL, USA: CRC Press, 1999, https://doi.org/10.4324/9780203908051.

[5] W. Wu and S. Jayasuriya, "A new QFT design methodology for feedback systems under input saturation," *Journal of Dynamic Systems, Measurement, and Control*, vol. 123, no. 2, pp. 225-232, 1999, https://doi.org/10.1115/1.1367337.

[6] "Control System Toolbox," MathWorks, R2013a, 2013.

[7] C. Borghesani, Y. Chait, and O. Yaniv, *The QFT frequency domain control design toolbox*, 3rd ed. San diego, CA: Terasoft, Inc., 2003.

[8] M. García Sanz and J. A. Osés, "Evolutionary algorithms for automatic tuning of QFT controllers," in *23rd IASTED International Conference Modelling, Identification and Control*, Grindelwald, Switzerland, 2004, Art. no. 412-094.

[9] I. Horowitz, "A synthesis theory for a class of saturating systems," *International Journal of Control*, vol. 38, no. 1, pp. 169-187, 1983, https://doi.org/10.1080/00207178308933067.

[10] W. Wu, and S. Jayasuriya, "Controller design for a nonovershooting step response with saturating nonlinearities," in *American Control Conference (Cat. No. 99CH36251)*, San Diego, CA, USA, 1999, pp. 3046-3050, https://doi.org/10.1109/ACC.1999.782321.

[11] H. Khalil, "Frequency domain analysis of feedback systems," in *Nonlinear Systems*, Prentice Hall, 2002, pp. 263-279.

[12] W. Wu and S. Jayasuriya. "Design of feedback systems with plant input rate saturation via QFT approach," *Journal of Dynamic Systems, Measurement, and Control*, vol. 128, no. 3, pp. 701-705, 2006, https://doi.org/10.1115/1.2232693.

[13] N. Niksefat and N. Sepehri, "Design and experimental evaluation of a robust force controller for an electro-hydraulic actuator via quantitative feedback theory," *Control Engineering Practice*, vol. 8, no. 12, pp. 1335-1345, 2000, https://doi.org/10.1016/S0967-0661(00)00075-7.

JSST
Journal of Space Science and Technology

P-ISSN: 2008-4560
E-ISSN: 2423-4516

Journal of Space Science and Technology

Vol. 17, Special Issue, pp. 45-58, 2024
https://doi.org/10.22034/jsst.2024.1509
Journal Homepage: https://jsstpub.com

Original Research Paper

Finite-Time Disturbance Observer Based Fractional Order Nonsingular Terminal Sliding Mode Attitude Control of Satellites

Shirkoo Piri, Jalil Beyramzad, and Esmaeel Khanmirza*

School of Mechanical Engineering, Iran University of Science and Technology, Tehran, Iran

ARTICLE INFO

Article History:

Received 30 November 2024
Revised 16 December 2024
Accepted 23 December 2024
Available Online 27 December 2024

Keywords:

Fractional order SMC
Attitude control
Satellite
Disturbance observer
Terminal sliding mode
Finite-time stability

ABSTRACT

This study presents a method for implementing rigid satellite output feedback control that considers dynamic uncertainties and external disturbances, all while avoiding the need for velocity state measurement. The dynamics of a rigid satellite are first represented using the modified Rodrigues parameter (MRP) and then transformed into Euler-Lagrangian form to provide the state-space representation of the dynamics. The availability of angular velocity data for practical applications is often limited by cost or technical limitations. Consequently, angular velocity is considered to be immeasurable. In order to minimize the need for extra mathematical calculations and the creation of separate observers to estimate uncertainties and system states, a finite time disturbance observer (third order sliding mode (TOSM) observer) was used to simultaneously estimate both uncertainties and system states. The main component of the suggested controller incorporates the fractional order nonsingular terminal sliding mode technique, which guarantees stability within a finite time and avoids chattering. The simulation results of the proposed methodology have been presented and compared with the results of techniques available in the literature, showcasing the efficacy of the method described in this study and the enhancement of the findings of previous relevant research.

*Corresponding Author's E-mail: khanmirz@iust.ac.ir

How to Cite this Article:
Sh. Piri, J. Beyramzad and E. Khanmirza, "Finite-time disturbance observer based fractional order nonsingular terminal sliding mode attitude control of satellites," *Journal of Space Science and Technology*, Vol. 17, Special Issue, pp. 45-58, 2024, https://doi.org/10.22034/jsst.2024.1509.

1. INTRODUCTION

For a spacecraft's attitude control system to be deemed appropriate for space missions, it must meet rigorous performance criteria. The challenge of managing a satellite's orientation is both significant and pragmatic. The significance of this function in many space operations, such as satellite surveillance, space station docking and installation, and spacecraft formation flying [1], is likely the reason for the interest in this function. Over the last several decades, much study has been carried out on various approaches to address the problem. The tactics include classic linear control, optimal control, model predictive control, nonlinear control approaches, and intelligent control strategies. It is important to note that most current spacecraft attitude control algorithms rely on having accurate and immediate measurement data for both attitude orientation and angular velocity [1]. Nevertheless, the availability of angular velocity data for practical purposes may be limited due to financial limitations or implementation limitations. Microsatellites, for instance, may not have the capability to gather data on angular velocity. Implementing partial state feedback attitude control systems for spacecraft is attractive due to the practical factor involved. This difficulty, which involves the lack of easily available velocity measurement data, has been extensively examined in previous research. Several methods have been proposed in the literature to develop attitude controllers that do not rely on angular velocity [1-6]. Sliding mode control (SMC) is a popular option among the several methods available for addressing issues related to the control of aeronautical systems. Many academics have used sliding mode control (SMC) for controlling uncertain systems because of its rapid dynamic response, ability to handle lumped uncertainty, and comparatively simple design approach. Despite the many benefits, using a linear sliding function in conventional sliding mode control leads to the inability to guarantee the finite-time convergence of the system's state error. However, this remains the case despite the many benefits. To bypass this limitation, researchers have developed a technique called terminal sliding mode control (TSMC). Instead of using a linear sliding function [7-9], this technique employs nonlinear sliding functions throughout the design phase. TSMC achieves enhanced accuracy and rapid convergence via meticulous parameter configuration. However, conventional TSMC exhibits two significant constraints: 1) SMC exhibits a faster convergence time compared to the current method. 2) The current method encounters a singularity problem. Numerous significant investigations have been carried out to address these shortcomings. The use of fast TSMC (FTSMC) in combination with nonsingular TSMC (NTSMC) resolved every problem. To simultaneously tackle both of these problems, a method called nonsingular fast TSMC (NFTSMC) has been developed. The NFTSMC controller has been extensively used in various systems due to its exceptional features, such as finite-time stability, singularity removal, high tracking performance, and robustness against uncertainties. These attributes have enabled the NFTSMC to effectively rival other control methods [9].

Chattering arises due to the use of a switching gain in both classic SMC and NFTSMC during the reaching phase, combined with a substantial fixed sliding gain, in order to mitigate the impact of lumped uncertainty. The system is negatively affected, hence reducing the efficacy of both control mechanisms indicated before.

Control approaches such as FTSMC or NTSMC have focused only on addressing specific vulnerabilities, disregarding the other weaknesses of the regular SMC. NFTSMC has the potential to rectify many limitations associated with traditional SMC or alternative control methods based on TSMC. However, including a high-frequency reaching control term into the control input of the aforementioned systems, such as TSMC, FTSMC, NTSMC, and NFTSMC, does not effectively reduce chattering. Consequently, several valuable control systems using high-order sliding mode control (HOSMC) have been suggested [10-11].

In recent years, there has been a significant amount of research conducted on applying control techniques based on terminal sliding mode to regulate the state of satellites [13-17]. This is due to the multiple benefits associated with these approaches.

Two challenging components of developing a control system using SMC or TSMC are understanding the boundaries of external disturbances and dynamic uncertainties, as well as creating a precise dynamic model. These factors are not predetermined for real-world systems. Several computer methods have been devised to estimate

this undisclosed model, such as different forms of neural networks and fuzzy logic systems [18]. Nevertheless, to successfully finalize the design process, controller designers need access to precise velocity data, which is often unattainable in a functioning system owing to limitations imposed by cost and space restrictions. Thus, if state feedback strategies are employed for controller design methods, the aforementioned control systems are not feasible for practical implementation. Instead, output feedback strategies must be utilized to ensure practical implementation of the designed control system.

To reduce or eliminate the chattering phenomenon, one might decrease the sliding gain of the switching element[12]. This is the core principle of the solution. Therefore, in order to account for the uncertainties, it is necessary to adjust the control signals by either fully or partially estimating the uncertainties. To address the estimated error caused by uncertainty, the switching element is now used. In order to achieve the sliding mode, the sliding gain will be adjusted to a lower value compared to the prior technique. The severity of the chattering phenomenon will decrease, depending on the precision of the estimating technique.

Several academics have recently integrated fractional calculus with various control approaches, such as TSM and NTSM controllers. Fractional-order controllers provide more flexibility in adjusting the time and frequency response of the closed-loop system. However, this is contingent upon their possessing a higher number of degrees of freedom (DOF) compared to their integer-order counterparts. Within the control world, fractional calculus is recognized as a potent tool that offers additional degrees of freedom, namely the order, which in turn allows for more flexibility in designing controllers with integer orders [19-20]. The use of fractional derivatives and integrals in sliding surfaces has several benefits, including strong resilience against uncertainties and external disturbances, enhanced reaction speed, avoidance of singularities, and rapid convergence rate [21]. Furthermore, extensive verification has shown that the fractional-order SM (FOSM) is capable of enhancing tracking and anti-disturbance performance when compared to the integer-order SM [19-21]. While these innovative controllers provide certain advantages in terms of delivering stability within a specific time frame, several studies fail to analytically analyze the stability and boundedness of the error signals after they reach the sliding surface. In other cases including a thorough stability investigation, the control rule often incorporates a fractional-order differentiator. Because the boundedness of the fractional-order differentiator has not been examined, the control law's boundedness cannot be completely ensured, unlike the fractional-order integrator. In addition, the use of FOSM controllers for spacecraft attitude control is limited, despite their many advantages. Several studies have shown that the use of a fractional-order controller (FOC) may improve the performance of control systems [19-20].

The basics of fractional order calculation, numerical calculations related to it, as well as their application in the design of fractional order control systems, have been discussed in detail in references [22-23], which can be referred to for further study.

Several model-based strategies have been proposed in the literature to estimate the uncertainty of dynamic systems, including time delay estimation method-based observer, neural networks and fuzzy logic-based observer, second-order, third-order or in general high order sliding mode observers, and extended state observer [18]. Since the TDE approach is limited to estimating the capacity of unknown inputs, an additional observer is necessary to estimate the velocities of the system. It increases the complexity of the system and contributes to the duration required for computation. The neural observer's ability to acquire knowledge and provide exceptional approximations enables it to supply estimated data with unlimited accuracy. Specifically, it must have the capability to estimate both the overall uncertainty and the velocities of the system. Consequently, the system depends on a solitary observer. Although the use of learning techniques might enhance long-term performance, the need for an online learning mechanism may impede the system's immediate performance in the face of external disruption [18-24].

The ability to implement such a system in real-world scenarios is also impeded by the intricacy of training neural network weights, which requires substantial computer resources.

Observers using fuzzy logic encounter comparable difficulties to those employing neural networks. In conclusion, it can be said that intelligent learning methods have the capability to

assess the uncertainty in the system. However, their implementation is complex due to the involvement of several weighting elements or fuzzy rules. Although traditional extended state observers possess the capability to estimate system states and uncertainty using a single observer, they suffer from inaccuracies and the estimation process is not finite time.

The second-order sliding mode (SOSM) observer is distinguished from other observers by its capability to estimate system velocities and uncertainties using finite-time error estimates [25]. This confers a competitive edge to the SOSM observer. The SOSM observer's output injection, used to estimate uncertainty, has a discontinuous term that leads to an unpleasant chattering phenomenon [18,24-26]. However, it is important to note that the velocity prediction produced using this approach is very precise and demonstrates little chattering compared to other methods. To restore the uncertainty, it is necessary to use a low-pass filter [18,24-26]. Conversely, this leads to a delay in the estimating process and a decrease in the accuracy of the SOSM observer's estimations. The third-order sliding mode (TOSM) observer, in comparison to the SOSM observer, offers improved estimation accuracy and less chattering when estimating lumped uncertainty. Furthermore, the TOSM observer retains almost all of the advantages linked to the SOSM observer. The TOSM observer has gained popularity among several experts [18,24-26] because of its significant benefits in regulating uncertain systems.

Consequently, recent studies have focused on the TOSM observer, which can provide a consistent output injection. Consequently, the compulsory filtering that was part of the SOSM observer has been eliminated. In the current study, the TOSM observer was used to determine both the velocities and uncertainties of rigid spacecraft systems, without the need for any filtering methods. Once convergence occurs, the anticipated velocity is replaced by the actual velocity signal. As a consequence, the design of the controller becomes more streamlined.

This work proposes the use of a fractional-order NTSMC as a way for accurate attitude control of rigid spacecraft, based on the acquired information from disturbance observer. The proposed approach obviates the necessity for real-time data on the system's velocity by leveraging an observer.

This proposed control approach allows us to get a control law that has desired attributes, including robustness in the presence of errors, high accuracy, non-singularity, removal of chattering, and finite-time stability, all without the need for angular velocity measurement.

2. MRP-BASED ATTITUDE DYNAMICS

The literature has extensively discussed the dynamics and kinematics of satellites, using several methodologies, each with its own advantages and disadvantages. Various methods, such as Eulerian angles, Euler-Rodrigues parameters (in Quaternion formulation), Cayley-Klein parameters, and Cayley-Rodrigues parameters, are used to describe the movement and behavior of satellites. Most control applications need parameterizations where the singularity is located at a significant distance from the origin. The assessment of attitude often uses the quaternion representation as a parameterization. When manipulating quaternions, the kinematic equations exhibit linearity concerning angular velocities, and there are no instances of singularities for any rotation of the Eigen axis in combination with an algebraic attitude matrix. Due to the use of four components in the quaternion parameterization to depict attitude motion, the quaternion components are neither minimum nor independent. Therefore, it is necessary for the quaternion to possess a norm of one [13-14].

In addition, the use of quaternion representation in the kinematic equations eliminates the possibility of singularities. However, due to the additional parameters needed for quaternions, this parameterization strategy is not minimal. Recently, the modified Rodrigues parameters (MRP) have been used in spacecraft control applications due to their ability to allow rotations of up to 360 degrees [13-14]. The Rodrigues parameters provide a concise representation in three dimensions. Regrettably, the presence of a singularity while performing 180-degree rotations makes this parameterization challenging to use for really large degrees of rotation. Employing rotations of fewer than 180 degrees in each consecutive revolution may perhaps help address this problem. The use of this portrayal of attitude yields the following advantages: The parameters enable rotations of 360 degrees and provide a basic parameterization.

Constructing observers and estimators to estimate satellite attitude is often essential. Utilizing the modified Rodrigues parameters technique, instead of the quaternion method, would streamline the mathematical control design process and reduce computational requirements. In the current work, we will use this modeling method to analyze and describe the satellite's dynamics and kinematics concerning the controller being examined.

In the event where $\sigma \in \mathcal{R}^3$ stands in for the MRP, as specified by [13-14], then we have:

$$\sigma = [\sigma_1 \quad \sigma_2 \quad \sigma_3]^T = \hat{e} \tan\frac{\theta}{4} \tag{1}$$

Where $\hat{e} = [e_1 \quad e_2 \quad e_3]$ is a rotation around the central axis and is a rotation about the Euler axis in the body frame. Here is a σ based description of the system's attitude kinematics:

$$\dot{\sigma} = \Gamma(\sigma)\omega \tag{2}$$

Where ω represents the angular velocity components expressed in a body axis frame $[x \quad y \quad z]$ relative to an inertial frame $[X \quad Y \quad Z]$ and $\Gamma(\sigma)$ equation is as follows [12-14]:

$$\Gamma(\sigma) = \frac{1}{4}[(1-\sigma^T\sigma)I_{3\times3} + 2S^*(\sigma) + 2\sigma\sigma^T] \tag{3}$$

$I_{3\times3}$ is the identity matrix, while the matrix $S^*(\sigma)$ is a skew-symmetric matrix written in the following form [15]:

$$S^*(\sigma) = \begin{bmatrix} 0 & -\sigma_3 & \sigma_2 \\ \sigma_3 & 0 & -\sigma_1 \\ -\sigma_2 & \sigma_1 & 0 \end{bmatrix} \tag{4}$$

When the control inputs $u(t) \in \mathcal{R}^3$ and the external disturbances $d(t) \in \mathcal{R}^3$ are taken into consideration, the dynamics of the rigid spacecraft may be represented as follows [13-15]:

$$J\dot{\omega} = -S^*(\omega)J\omega + u(t) + d(t) \tag{5}$$

Where $J \in \mathcal{R}^3$ refers to the matrix that represents the moment of inertia and $S^*(\omega)$ refers to the skew-symmetric matrix that represents the angular velocity. The following is a Lagrangian version of the dynamics of the spacecraft's attitude stabilization [13-15], which is derived by using Equations (2) and (5):

$$M(\sigma)\ddot{\sigma} + C(\sigma,\dot{\sigma})\dot{\sigma} = \tau + \tau_{ext} \tag{6}$$

Different components of the aforementioned equation may be written as follows:

$$M(\sigma) = \Gamma(\sigma)^{-T}J\Gamma(\sigma)^{-1} \tag{7}$$

$$C(\sigma,\dot{\sigma}) = -\Gamma(\sigma)^{-T}J\Gamma(\sigma)^{-1}\dot{\Gamma}(\sigma)\Gamma(\sigma)^{-1} - \Gamma(\sigma)^{-T}S^*(J\omega)\Gamma(\sigma)^{-1} \tag{8}$$

$$\tau = \Gamma(\eta)^{-T}u(t) \tag{9}$$

$$\tau_{ext} = \Gamma(\eta)^{-T}d(t) \tag{10}$$

The state space form of dynamic equations is often utilized in controller design for nonlinear systems. With the assumptions of $x_1 = \sigma$ and $x_2 = \dot{\sigma}$, the satellite dynamic equations may be written in the following state space form:

$$\begin{cases} \dot{x}_1 = x_2 \\ \dot{x}_2 = f(x) + g(x)u + d^* \end{cases} \tag{11}$$

Where $f(x) = M^{-1}(\sigma)C(\sigma,\dot{\sigma})\dot{\sigma}$, $g(x) = M^{-1}(\sigma)\Gamma(\sigma)^{-T}$ and $d^* = M^{-1}(\sigma)\Gamma(\sigma)^{-T}d(t)$

Whereas d^* is the unknown bounded external disturbances $|d^*| \le \delta_d$. The two functions represented by $f(x)$ and $g(x)$ are considered here, each of which may be expressed as the sum of a nominal function and an unknown but limited uncertainty:

$$\begin{cases} f(x) = f_0(x) + \Delta f(x); |\Delta f(x)| \le \delta_f \\ g(x) = g_0(x) + \Delta g(x); |\Delta g(x)| \le \delta_g \end{cases} \tag{12}$$

Using Eq. (12) in place of Eq. (11), we get:

$$\begin{cases} \dot{x}_1 = x_2 \\ \dot{x}_2 = f_0(x,t) + g_0(x,t)u + \Delta(x,t) \\ y = x \end{cases} \tag{13}$$

The system total lumped uncertainty is denoted by $\Delta(x,u,t) = \Delta f(x) + \Delta g(x)u + d^*$. With the assumption of a maximum value for the control inputs $|u| \le \delta_u$, the following may be written:

$$|\Delta(x,t)| \le |\Delta f + \Delta g\delta_u + \delta_d| \le |\delta_f + \delta_g\delta_u + \delta_d| \le \Delta_D \tag{14}$$

3. CONTROLLER DESIGN

To design the controller, we first define the sliding surface as follows:

$$s = e + \frac{1}{\lambda} sig(\dot{e})^{\eta} \quad (15)$$

Where $sig(\dot{e})^{\eta} = |\dot{e}|^{\eta} sign(\dot{e})$, and $1 < \eta < 2$. Once $s = 0$ is achieved, the sliding mode surface Eq. (18) may be expressed in the following manner:

$$0 = e + (1/\lambda) sig(\dot{e})^{\eta} \quad (16)$$

The time T_s required for the tracking error $e(t)$ to approach zero is provided in reference [27]:

$$T_s = \frac{max(e(0))^{(1-1/\eta)}}{\lambda^{(1/\eta)}(1 - 1/\eta)} \quad (17)$$

Once the appropriate sliding surface, as defined by Eq. (18), has been determined, the subsequent task is to develop a NTSMC that will guide system of Eq. (13) towards this sliding surface. As per the sliding mode design approach, the control input u is composed of two components $u = u_{eq} + u_{SMC}$. The equivalent control, denoted as u_{eq}, is derived by solving the equation $\dot{s} = 0$ for the nominal system, disregarding any errors or external disturbances. By differentiating Eqs. (15) concerning time, one obtains:

$$\dot{s} = \dot{e} + \frac{\eta}{\lambda} |\dot{e}|^{\eta-1} \ddot{e} \quad (18)$$

By rewriting Eqs. (13), $\ddot{e}$ becomes:

$$\ddot{e} = f_0(x,t) + g_0(x,t)u(t) + \Delta(x,t) - \ddot{x}_d(t) \quad (19)$$

By replacing the Eqs. (19) with Eqs. (18), we get:

$$\dot{s} = \dot{e} + \frac{\eta}{\lambda} |\dot{e}|^{\eta-1} (f_0(x,t) + g_0(x,t)u(t) + \Delta(x,t) - \ddot{x}_d(t)) \quad (20)$$

Given the constraint $\dot{s} = 0$, one can choose the appropriate control law as:

$$u_{eq} = \frac{1}{g_0(x,t)} \left(\ddot{x}_d(t) - f_0(x,t) - \frac{\lambda \dot{e}}{\eta} |\dot{e}|^{1-\eta} \right) \quad (21)$$

The switching control is constructed in the following manner:

$$u_{SW} = -\frac{1}{g_0(x,t)} (K \text{sign}(s)) \quad (22)$$

Next, the overall control u is determined:

$$u = u_{eq} + u_{SW} = \frac{1}{g_0(x,t)} \left(\ddot{x}_d(t) - f_0(x,t) - \frac{\lambda \dot{e}}{\eta} |\dot{e}|^{1-\eta} - K sign(s) \right) \quad (23)$$

3.1 Design of FO-NTSMC

For the design of FO-NTSMC, some of the main concepts of fractional order calculus are explained below.

A fractional operator is a generalization of the differential and integral operators, indicated by the fundamental operators ${}_{t_0}D_t^{\alpha}, {}_{t_0}I_t^{\alpha}$. These operators have a simple formulation as follows:

Definition 1. Function $x(t)$'s α -order Riemann-Liouville fractional integration may be expressed as

$${}_{t_0}I_t^{\alpha} x(t) = \frac{1}{\Gamma(\alpha)} \int_{t_0}^{t} (t-s)^{\alpha-1} x(s) ds \quad (24)$$

Given that $\alpha \in R^+$, t_0 represents the starting time, and $\Gamma(\alpha)$ refers to Euler's Gamma function:

$$\frac{d^{\alpha} x(t)}{dt^{\alpha}} = {}_{t_0}D_t^{\alpha} x(t) = \frac{1}{\Gamma(m-\alpha)} \frac{d^m}{dt^m} \int_{t_0}^{t} (t-s)^{m-\alpha-1} x(s) ds \quad (25)$$

That is, m is the first integer greater than α, where $m - 1 \leq \alpha < m$.

Definition 2. The function $x(t)$'s α -order Caputo fractional derivative is expressed as:

$${}_{t_0}D_t^{\alpha} x(t) = \frac{d^{\alpha} x(t)}{dt^{\alpha}} = \frac{1}{\Gamma(m-\alpha)} \int_{t_0}^{t} (t-s)^{m-\alpha-1} \frac{d^m}{ds^m} x(s) ds \quad (26)$$

Where m is first integer greater than α. For the Riemann–Liouville derivative, the following equivalence is true:

$${}_{t_0}I_t^{\alpha} \left({}_{t_0}D_t^{\alpha} x(t) \right) = x(t) - \sum_{i=1}^{m} \left[{}_{t_0}I_t^{i-\alpha} x(t) \right]_{t=t_0} \frac{(t-t_0)^{\alpha-i}}{\Gamma(\alpha - i + 1)} \quad (27)$$

Assumed that $x(t)$ is a function with integrable fractional derivative ${}_{t_0}D_t^{\alpha} x(t)$ $(m - 1 \leq \alpha < m)$.

Lemma 1 [30]**.** The operator ${}_{t_0}I_t^{\alpha}$, which represents fractional integration, is bounded and adheres to the following approximation$\| {}_{t_0}I_t^{\alpha}x\| \leq B \| x \|$.

Theorem 1 [28]: Consider $x = 0$ as a point of equilibrium for the nonautonomous fractional-order system ${}_{t_0}D_t^{\alpha} = f(x,t)$, where $f(x,t)$ fulfills the Lipschitz condition with a Lipschitz constant$l > 0$. Let us pretend that there is a Lyapunov function $V(t,x)$ that meets:

$$\alpha_1 \| x \| \leq V(t,x) \leq \alpha_2 \| x \| \text{ and } \dot{V}(t,x) \leq -\alpha_3 \| x \| \tag{28}$$

Where $\alpha \in (0,1)$ and $\alpha_i \in R^+, i = 1,2,3$. Subsequently, the system's equilibrium point attains asymptotic stability.

Theorem 2 [29]: Assume that $x = 0$ is an equilibrium point for fractional order non-autonomous system ${}_{t_0}D_t^{\alpha} = f(x,t)$, where $f(x,t)$ applies in Lipschitz conditions with Lipschitz constant $l > 0$. And there is a Lyapunov function like $V(t,x)$ that applies in the following condition:

$$\alpha_1(\| x \|) \leq V(t,x) \leq \alpha_2(\| x \|) \text{ and } {}_{t_0}D_t^{\alpha}V(t,x) \leq -\alpha_3(\| x \|) \tag{29}$$

Now, to design FO-NTSMC, we define the sliding surface as follows.

$$s = {}_{t_0}D_t^{\alpha}e + \frac{1}{\lambda}sig(\dot{e})^{\eta} \tag{30}$$

Where $\eta \in (1,2)$, λ is a specified positive constant, and ${}_{t_0}D_t^{\alpha}$ is the fractional derivative of order $\alpha \in (0,1)$. By dividing the tracking error definition by Eq. (30) and adding it to Eq. (13), we get:

$$\dot{s}(t) = {}_{t_0}D_t^{\alpha+1}e(t) + \frac{\eta}{\lambda}\ddot{e}(t)|\dot{e}|^{\eta-1} = {}_{t_0}D_t^{\alpha+1}e(t) + \frac{\eta}{\lambda}|\dot{e}|^{\eta-1}(f_0(x,t) + g_0(x,t)u + \Delta(x,t) - \ddot{x}_d) \tag{31}$$

In order to get the equivalent control set $\dot{s} = 0$, the necessary response may be accomplished by selecting the control law as $u = u_{eq} + u_{SW}$, where:

$$u_{eq} = \frac{1}{g_0(x,t)}\left(\ddot{x}_d(t) - f_0(x,t) - \frac{\lambda}{\eta}\left({}_{t_0}D_t^{\alpha+1}e(t)\right)|\dot{e}|^{1-\eta}\right) \tag{32}$$

u_{eq} Serves as the corresponding control element for operating the nominal component of the system.

$$u_{\text{SW}} = -\frac{1}{g_0(x,t)}(K_1 s + K_2 sign(s) + \Delta_D) \tag{33}$$

The robust control item u_{SW} is designed to effectively manage the lumped uncertainty $\Delta(x,t)$. The theorem presented below demonstrates that the convergence speed of surface Eq. (30) surpasses that of the integer-order terminal sliding mode control, as defined by Eq. (19).

- *Stability Analysis*

To prove the stability of the proposed control system, we first define the Lyapunov function as follows:

$$V = (1/2)s^2 \tag{34}$$

By taking the derivative of V with respect to time and using Eq. (31), we get:

$$\begin{aligned} \dot{V} &= s\dot{s} \\ &= s\left({}_{t_0}D_t^{\alpha+1}e(t) + \frac{\eta}{\lambda}|\dot{e}|^{\eta-1}(f_0(x,t) + g_0(x,t)u + \Delta(x,t) - \ddot{x}_d)\right) \\ &= s\left({}_{t_0}D_t^{\alpha+1}e(t) + \frac{\eta}{\lambda}|\dot{e}|^{\eta-1}(f_0(x,t) - \ddot{x}_d + \Delta(x,t))\right) + \frac{\eta}{\lambda}|\dot{e}|^{\eta-1}g_0(x,t)u \end{aligned} \tag{35}$$

It is possible to demonstrate that $\dot{V} \leq 0$ as long as the switching gain $|\Delta(x,t)| < \Delta_D$. By replacing the Eq. (32) and Eq. (34) with Eq. (35), we get:

$$\begin{aligned} \dot{V}(s) &= s\frac{\eta}{\lambda}|\dot{e}|^{\eta-1}\left(\Delta(x,t) - (K_1 s + K_2 sign\,(s) + \Delta_D)\right) \\ &\leq s\frac{\eta}{\lambda}|\dot{e}|^{\eta-1}\left(|\Delta(x,t)| - (K_1 s + K_2 sign\,(s) + \Delta_D)\right) \\ &\leq \frac{\eta}{\lambda}|\dot{e}|^{\eta-1}(-sK_1 s - K_2|s|) \leq 0 \end{aligned} \tag{36}$$

Therefore, according to Theorem 1 the system states will asymptotically approach $s(t) = 0$. Subsequently, we demonstrate that the discrepancy in tracking diminishes to zero within a finite time. Let t_r represent the time it takes for the system states to reach the sliding surface. This time may be approximated using Eq. (36), which specifies that $\dot{V}(s) = s\dot{s} \leq -(\eta K/\lambda)|s|$, where $K = max\{K_1, K_2\}$. By integrating $\dot{V}(t)$ with regard

to the final time $t = t_r$ and observing that $s(0) = 0$, the value of t_r can be determined as $t_r \leq |\lambda s(0)/\eta K|$. Consider $S_r = inf\{t \geq t_r : e(t) = 0\}$ as a stopping time for the states of the system. Next, we demonstrate the existence of a $t_s \in [t_r, \infty)$ that satisfies $S_r \leq t_s$. Specifically, by applying the fractional integral to both sides of Eq. (30) throughout the time interval from t_r to t, we get [27]:

$$\begin{aligned} &{}_{t_r}I_t^{\alpha}\left({}_{t_r}D_t^{\alpha}e(t)\right) \\ &= e(t) - {}_{t_r}D_t^{\alpha-1}e(t)\big|_{t=t_r}\frac{(t-t_r)^{\alpha-1}}{\Gamma(\alpha)} \\ &= -\frac{1}{\lambda_{t_r}}I_t^{\alpha}|\dot{e}(t)|^{\eta} \end{aligned} \tag{37}$$

Where ${}_{t_r}D_t^{\alpha-1}e(t)|_{t=t_r}((t-t_r)^{\alpha-1}/\Gamma(\alpha)) = 0$. By using the norm property, denoted as $\| \gamma u \| = |\gamma| \| u \|$, for $\gamma \in R$, and employing the outcome of Lemma 1, ($\| {}_{t_r}I_t^{\alpha}|\dot{e}(t)|^{\eta}\| \leq B\||\dot{e}(t)|^{\eta}\|$), we get:

$$\| e(t) \| \leq \frac{B}{\lambda}\||\dot{e}(t)|^{\eta}\| \leq \frac{B}{\lambda}\| \dot{e}(t) \|^{\eta} \tag{38}$$

Where B and λ are constants with positive values. By performing the integral of both sides of Eq. (38) with respect to the integer order from the time t_r to $t_s \in [t_r, \infty)$, we may get the following result [27]:

(39)

$$\begin{aligned} \left|\int_{t_r}^{t_s}\left(\frac{\lambda}{B}\right)^{1/\eta} ds\right| &\leq \left|\int_{t_r}^{t_s}\frac{d(\| e(s) \|)}{\| e(s) \|^{1/\eta}}\right| \Rightarrow t_s - t_r \\ &\leq \left(\frac{B}{\lambda}\right)^{1/\eta}\frac{\eta}{\eta-1}\left|\|e(t_s)\|^{1-\frac{1}{\eta}} - \|e(t_r)\|^{1-\frac{1}{\eta}}\right| \end{aligned}$$

(40)

$$t_s \leq \left(\frac{B}{\lambda}\right)^{1/\eta}\frac{\eta}{\eta-1}\|e(t_r)\|^{1-\frac{1}{\eta}} + t_r$$

Thus, it follows that the tracking error approaches zero at the finite time and so concludes the proof of stability.

Remark 1: It is important to highlight that to effectively manage significant uncertainties and external disturbances, the value of the switching item K_2 in controller Eq. (33) has to be substantial. This leads to a significant occurrence of chattering phenomena. In previous studies, many other functions have been suggested to replace the sign function to reduce chattering. Among these alternatives, we use the function $\frac{S}{\sqrt{S^2+1}}$ as a replacement for the sign function.

4. FINITE TIME DISTURBANCE OBSERVER DESIGN

For a second-order nonlinear system with a generic dynamics equation in the form of Eq. (13), the TSOM design is as follows [18,24-26]:

(41)

$$\begin{aligned} \dot{\hat{x}}_1 &= \rho_1|x_1 - \hat{x}_1|^{2/3}\text{sign}\,(x_1 - \hat{x}_1) + \hat{x}_2 \\ \dot{\hat{x}}_2 &= f_0(\hat{x}) + g_0(\hat{x})u + \rho_2|x_1 - \hat{x}_1|^{1/3}\text{sign}\,(x_1 - \hat{x}_1) - \\ \dot{\hat{\varphi}} &= -\rho_3\,\text{sign}(x_1 - \hat{x}_1) \end{aligned}$$

Where $\hat{x}$ is the estimation of x and ρ_i represents the observer's gains. The estimation error can be obtained by dividing the Eq. (13) and Eq. (41) as follows:

(42)

$$\begin{aligned} \dot{\tilde{x}}_1 &= -\rho_1|\tilde{x}_1|^{2/3}\text{sign}\,(\tilde{x}_1) + \tilde{x}_2 \\ \dot{\tilde{x}}_2 &= -\rho_2|\tilde{x}_1|^{1/3}\text{sign}\,(\tilde{x}_1) + \Delta(x,u,t) - d(x,\tilde{x},u,t) + \\ \dot{\tilde{\varphi}} &= -\rho_3\text{sign}\,(\tilde{x}_1) \end{aligned}$$

Where $\tilde{x} = x - \hat{x}$ represents the estimation error of the system states and the uncertainty estimation error function is written as follows:

(43)

$$\begin{cases} d(x,\tilde{x},u) = \{f_0(\hat{x}) + g_0(\hat{x})u\} - \{f_0(x) + g_0(x)u\} \\ \hat{\Delta}(x,\hat{x},u,t) = \Delta(x,u,t) - d(x,\tilde{x},u,t) \end{cases}$$

It is important to acknowledge that the error of estimating uncertainty is expected to be limited by $\| d(x,\tilde{x},u,t) \| \leq \Upsilon$.

Hence, the observer equation expressed in equation (21) may be restated as:

$$\begin{aligned} \dot{\tilde{x}}_1 &= -\rho_1|\tilde{x}_1|^{2/3}\text{sign}\,(\tilde{x}_1) + \tilde{x}_2 \\ \dot{\tilde{x}}_2 &= -\rho_2|\tilde{x}_1|^{1/3}\text{sign}\,(\tilde{x}_1) + \hat{\Delta}(x,\hat{x},u,t) + \hat{\varphi} \\ \dot{\hat{\varphi}} &= -\rho_3\text{sign}\,(\tilde{x}_1) \end{aligned} \tag{44}$$

The observer equation may be expressed by introducing the new variable $\hat{\varphi}_0 = \hat{\Delta}(x,\hat{x},u,t) + \hat{\varphi}$ as follow:

$$\begin{aligned} \dot{\tilde{x}}_1 &= -\rho_1|\tilde{x}_1|^{2/3}\text{sign}\,(\tilde{x}_1) + \tilde{x}_2 \\ \dot{\tilde{x}}_2 &= -\rho_2|\tilde{x}_1|^{1/3}\text{sign}\,(\tilde{x}_1) + \hat{\varphi}_0 \\ \dot{\hat{\varphi}}_0 &= -\rho_3\,\text{sign}(\tilde{x}_1) + \dot{\hat{\Delta}}(x,\hat{x},u,t) \end{aligned} \tag{45}$$

The equation provided represents the TOSM observer in its ultimate form, referred to as the

standard form of the second-order robust exact differentiator. This form ensures finite temporal stability, as shown in references [17-20]. By appropriately selecting the parameter values of the observer, the estimated errors of the states and uncertainties of the system will reach a value of zero within a limited amount of time. The settings for the TOSM observer may be chosen based on the findings of the research referenced in [17] in the following manner:

$$\begin{cases} \rho_1 = \lambda_1 L^{1/3}, \rho_2 = \lambda_2 L^{2/3}, \rho_3 = \lambda_3 L \\ \lambda_1 = 2, \lambda_2 = 2.12, \lambda_3 = 1.1 \\ L = \Lambda + \Upsilon \end{cases} \quad (46)$$

To calculate the uncertainty function of the system, it is essential to acknowledge that once the observer converges, the estimated state values will correspond to the actual state values of the system. Consequently, the error function used to estimate uncertainty will converge to zero ($\hat{x}_1 = x_1, \hat{x}_2 = x_2 \rightarrow d(x, \tilde{x}, u, t) = 0$).

Hence, the third component of the observer's equation may be expressed in the following manner:

$$\dot{\hat{\varphi}}_0 = -\rho_3 \text{sign}\,(\tilde{x}_1) + \dot{\hat{\Delta}}(x, \hat{x}, u, t) \equiv 0 \quad (47)$$

Hence, the calculation of the system's uncertainty estimation function may be determined in the following manner:

$$\hat{\Delta}(x, \hat{x}, u, t) = \int \rho_3 \text{sign}\,(\tilde{x}_1) \quad (48)$$

Given that the uncertainty function estimation in Eq. (48) has an integral component, the use of a low-pass filter is unnecessary for reconstructing the uncertainty estimation from the output injection term. The exceptional attribute of the TOSM observer enables more accurate estimations compared to conventional sliding mode-based observers.

To simulate the designed FTDO-based control system and its implementation, as well as to prove the stability, it is enough to insert the values obtained from the observer related to states and disturbance (lumped uncertainty) into the equations related to the controller design.

The issue that needs to be taken into consideration here is related to the interaction between the stability type of the observer and the controller. If the observer used in a control structure has asymptotic stability and the designed control system has finite time stability, it is possible that the control system as a whole does not have finite time stability. Therefore, after proving the stability of the observer and controller separately, the stability of the control system set should be checked once again considering the estimated values for the states and uncertainties of the system. Also, if the observer used has finite time stability, it will provide the guarantee that the estimated values of the system states will converge to the real values of the system states after a finite time and will be equivalent. Therefore, there is no need to prove the stability of the control system by placing the estimated values of the system states and uncertainties obtained from the observer [26]. In the current research, considering that the observer used is of the third-order sliding mode type and has finite time stability, therefore, re-proving the stability of the presented control system in combination with the observer will not be required, and proving the stability of the observer and controller independently of each other is sufficient.

Remark 2. One of the important points about fractional-order controllers is the challenge of their practical implementation. Given that the process of calculating fractional-order derivatives is different and more complex than natural-order derivatives, the question arises whether these methods can be implemented in practice, regardless of the results obtained from theoretical simulations. In recent years, considerable efforts have been made by researchers for this purpose, and fractional-order controllers have been successfully tested in practice in controlling various dynamic systems, and similar results have been obtained with the results obtained from theoretical simulations. As an example, we can refer to the research conducted in [13-15]. Therefore, based on the research conducted, it can be said that in the problem of controlling the attitude of satellites, the advantages of fractional-order control methods can be used in practice to improve tracking accuracy, convergence speed, and control system robustness. In this study, the simulations were designed to incorporate realistic satellite dynamics, including parametric uncertainties and external disturbances, as encountered in actual missions. The inclusion of these factors ensures that the testing conditions closely emulate practical scenarios. The proposed fractional-order sliding mode controller (FOSMC) and third-order sliding mode disturbance observer (TOSMDO) are designed to be computationally

efficient and implementable on existing satellite onboard processors. The methods primarily rely on measurable or estimable states, making them practical for real-time operations. Additionally, the robustness of FOSMC to parametric uncertainties and disturbances is advantageous for satellites operating in uncertain and varying conditions. While fractional-order controllers may introduce additional computational complexity compared to integer-order controllers, advancements in onboard computational capabilities and optimized algorithms can mitigate these concerns. Moreover, the third-order sliding mode disturbance observer relies on high-gain properties, which are sensitive to measurement noise. This challenge can be addressed by using appropriate noise-filtering techniques or sensor fusion approaches.

5. SIMULATION AND RESULTS

This segment comprises a simulation that demonstrates the functionality and effectiveness of the suggested controller. Because the outcomes of the proposed method will be juxtaposed with those of reference [14], the following simulation parameters and attitude reference signals are selected:

$$\sigma_d = 0.5[\sin(0.01t), -\cos(0.01t), \sin(0.01t)]^T$$
$$\sigma(0) = [0.7 \quad 0.5 \quad -0.3]^T$$
$$\omega(0) = [-0.001 \quad 0.001 \quad -0.001]^T \text{rad/s}$$
$$J = \begin{bmatrix} 3.06 & 1 & 0.4 \\ 1 & 3 & 1 \\ 0.4 & 1 & 3.95 \end{bmatrix}$$

For the simulation conditions to be close to reality, the uncertainty term and external disturbances are considered thoroughly, and a random term is also considered for unmodeled factors as follows:

$$d(t) = \begin{bmatrix} 0.06 - 0.04\sin(\omega_o t) + 0.05\cos(\omega_o t) \\ 0.07 + 0.05\sin(\omega_o t) - 0.04\cos(\omega_o t) \\ 0.04 - 0.03\sin(\omega_o t) + 0.03\cos(\omega_o t) \end{bmatrix} + 0.25 \times rand(3,1)(N \cdot m)$$

Where $\omega_o = \sqrt{\mu_g / \|\boldsymbol{r}\|^3}$ and $\mu_g = 3.986 \times 10^{14} (\text{m}^3/\text{s}^2)$.

The simulation results of the proposed control approach are depicted in Fig. 1–7, which are compared to the results reported in reference [14]. The tracking performance is satisfactory, as illustrated in the figures, and the control method outlined in this research surpasses the approach described in reference [14] concerning both tracking and control input performance. Fig. 1 and Fig. 2 show the position-tracking performance of the proposed control system and the position-tracking errors, and Fig. 3 and Fig. 4 show the velocity-tracking performance and the velocity-tracking errors, respectively. According to the results, it is clear that the FONTSMC control method combined with FTDO has a better performance than other used methods. The important point that can be taken from the obtained results is that the use of FTDO reduces the tracking error and improves the performance of the system. Also, according to the results, it is clear that fractional order controllers have better accuracy and convergence speed than integer order controllers.

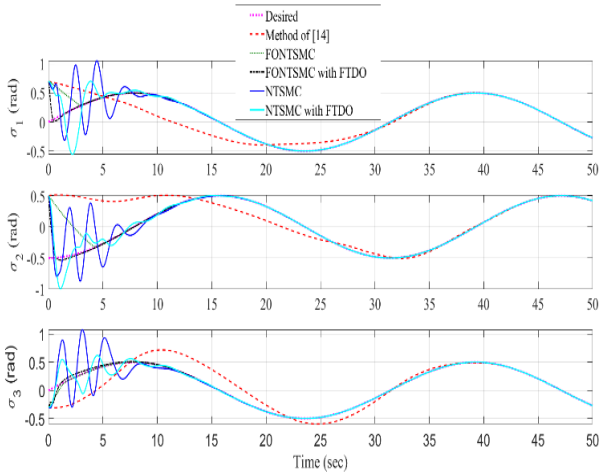

Fig. 1. Attitude tracking performance.

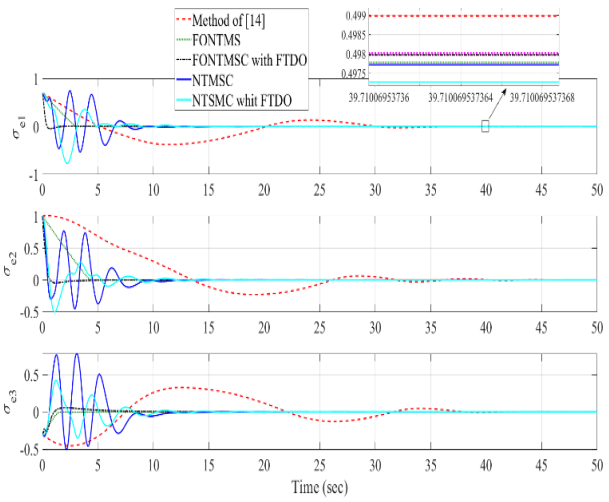

Fig. 2. Attitude tracking errors.

Figures 3 shows the results related to the time evolution of sliding surface functions and Fig. 4 shows the results related to the control inputs. Considering that the sign function in the control inputs was replaced with the function considered in Remark 1, the obtained results show that the obtained control inputs do not have chattering. Also, according to the results, it is clear that the control inputs related to a controller that uses the disturbance observer have a smaller domain, which is due to the accurate estimation of uncertainties and external disturbances entering the system and using the estimated values in the function of control inputs. The coefficient of the sign function for the stability of the control system is chosen in such a way that its value is greater than the system uncertainty function, which in the case of not using a disturbance observer, usually a large value is chosen as a precaution, which causes an increase in chattering and the range of control signals.

Therefore, the obtained results show the advantage of using disturbance observers in reducing the chattering phenomenon. The control inputs obtained in [14], although after reaching the stable state, have very small values, which are comparable in size to the control inputs obtained from the proposed control method, as can be seen in the obtained results, these signals have chattering that may damage the performance of the system drives in the long run.

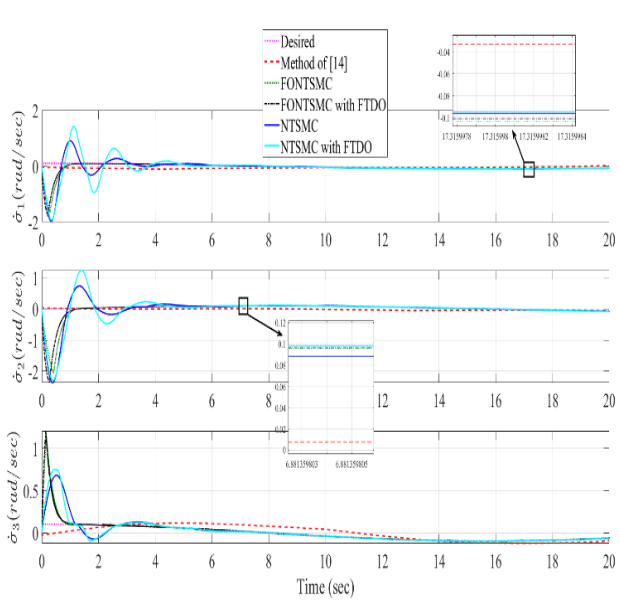

Fig. 3. Angular velocity tracking performance.

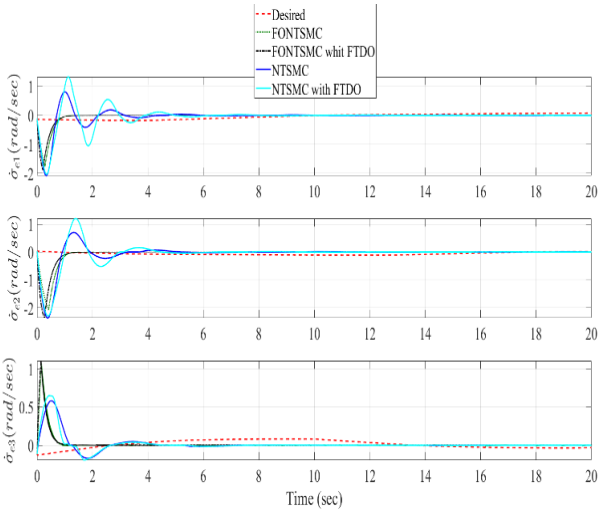

Fig. 4. Angular velocity tracking errors.

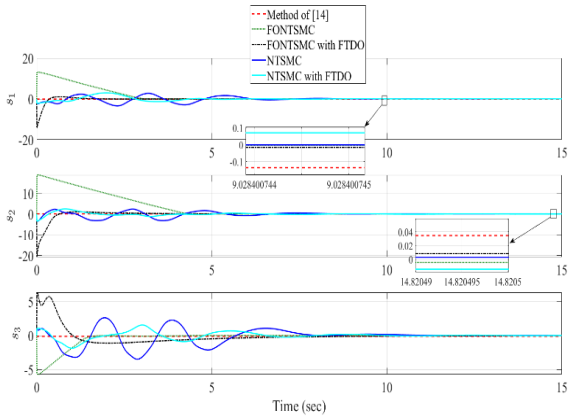

Fig. 5. Sliding surfaces.

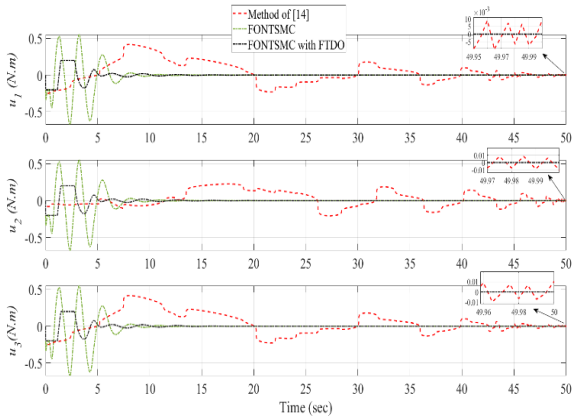

Fig. 6. Control inputs.

Figures 7 shows the performance results of the finite time disturbance observer in estimating system velocities. According to the obtained results, it is clear that the used observer has been able to estimate the states related to the velocities of the

system with high accuracy and reach convergence after a finite time.

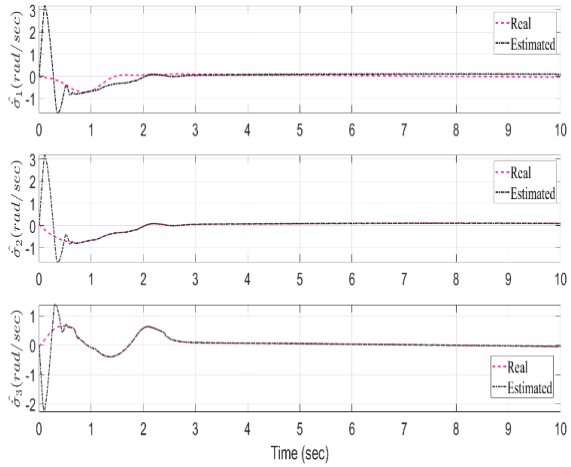

Fig. 7. FTDO observer performance in state estimation.

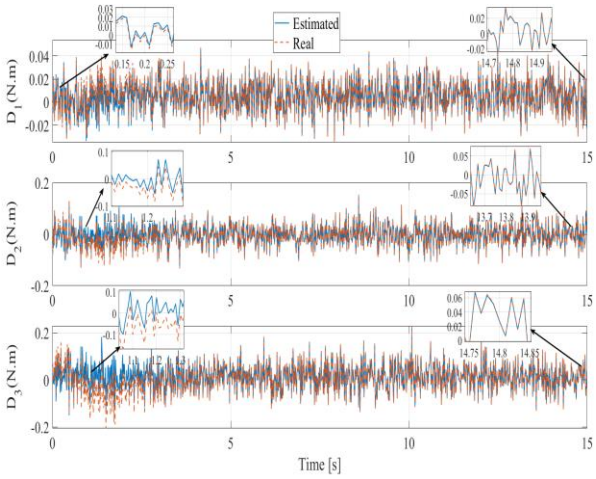

Fig. 8. FTDO observer performance in disturbance estimation.

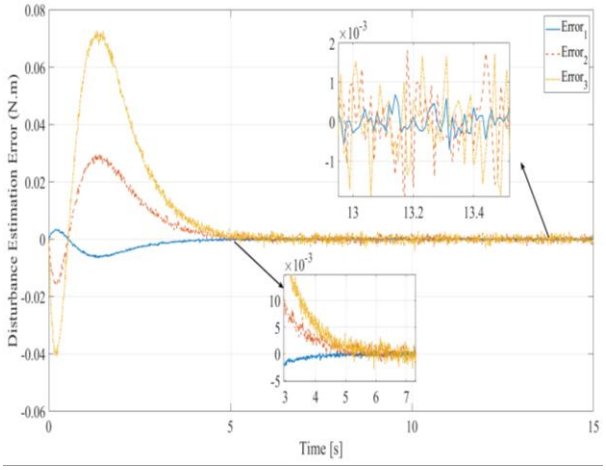

Fig. 9. FTDO observer's disturbance estimation errors.

Figures 8 and 9 show the performance of the designed disturbance observer in estimating the disturbance and uncertainty function and the estimation errors, respectively. As is clear from the figures, the observer has been able to estimate the external disturbances and uncertainty function with very high accuracy even in the presence of random noise. The steady-state error of the designed observer is of the order of 10^{-3}, which is considered to be very high accuracy. As previously stated, being resistant to noise was one of the important features of high-order sliding mode observers, and its objective performance can be seen here. This accurate estimation performance in the controller structure improves the tracking accuracy and also makes the control signals smoother and eliminates the chattering phenomenon.

6. CONCLUSIONS

This paper proposes a finite-time stable, fast convergent, and chattering-free attitude control system that does not need angular velocity data. For building an attitude controller, we utilized fractional order NTSMC in conjunction with FTDO (TOSM observer). The simulation results demonstrate the efficacy of the suggested strategy for rigid spacecraft attitude control. The obtained results indicate a very positive effect of using the proposed observer in improving the quality of control input signals as well as improving the accuracy of controller tracking due to the use of fractional order derivatives. The proposed methods have been developed with practical satellite operations in mind and tested under realistic conditions. We are confident that with appropriate engineering adaptations, the performance demonstrated in simulations can be realized in domestic satellite design and projects. To further validate the practical applicability of the proposed methods, future work will involve hardware-in-the-loop (HIL) simulations and real-world testing using small satellite platforms. These tests will provide additional insights into the implementation challenges and fine-tuning required for real missions.

CONFLICT OF INTERESTS

No conflict of interest has been expressed by the authors.

REFERENCES

[1] N. Nazari, H. Moladavoudi, and J. Beyramzad, "Finite time sliding mode control for agile rigid satellite with CMG actuators using fast high-order sliding mode observer," *Aerospace Systems*, vol. 7, pp. 363-383, 2024, https://doi.org/10.1007/s42401-024-00283-4.

[2] Y. Guo, B. Huang, J. H. Guo, A. J. Li, and C. Q. Wang, "Velocity-free sliding mode control for spacecraft with input saturation," *Acta Astronautica*, vol. 154, pp. 1-8, 2019, https://doi.org/10.1016/j.actaastro.2018.10.045.

[3] K. Zhang, G. R. Duan, and M. D. Ma, "Dynamic output feedback sliding mode control for spacecraft hovering without velocity measurements," *Journal of the Franklin Institute*, vol. 356, no. 4, pp. 1991-2014, 2019, https://doi.org/10.1016/j.jfranklin.2019.01.030.

[4] L. Yuan, G. Ma, C. Li, and B. Jiang, "Finite-time attitude tracking control for spacecraft without angular velocity measurements," *Journal of Systems Engineering and Electronics*, vol. 28, no. 6, pp. 1174-1185, 2017, https://doi.org/10.21629/JSEE.2017.06.15.

[5] Q. Hu and B. Jiang, "Continuous finite-time attitude control for rigid spacecraft based on angular velocity observer," *IEEE Transactions on Aerospace and Electronic Systems*, vol. 54, no. 3, pp. 1082-1092, 2017, https://doi.org/10.1109/TAES.2017.2773340.

[6] M. Malekzadeh and H. Sadeghian, "Attitude control of spacecraft simulator without angular velocity measurement," *Control Engineering Practice*, vol. 84, pp. 72-81, 2019, https://doi.org/10.1016/j.conengprac.2018.11.011.

[7] Y. Shtessel, C. Edwards, L. Fridman, and A. Levant, *Sliding Mode Control and Observation*, New York: Springer, 2014, https://doi.org/10.1007/978-0-8176-4893-0.

[8] J. Liu and X. Wang, *Advanced Sliding Mode Control for Mechanical Systems: Design, Analysis and MATLAB Simulation*, Berlin: Springer, 2012, https://doi.org/10.1007/978-3-642-20907-9.

[9] V. Shahbahrami, M. Azimi, and A. Alikhani, "Attitude and vibration control of a flexible spacecraft using hybrid adaptive super-twisting non-singular terminal sliding mode control," *Journal of Space Science and Technology*, vol. 16, no. 4, pp. 1-13, 2021, https://doi.org/10.30699/jsst.2023.1365.

[10] V. Utkin, A. Poznyak, Y. Orlov, and A. Polyakov, "Conventional and high order sliding mode control," *Journal of the Franklin Institute*, vol. 357, no. 15, pp. 10244-10261, 2020, https://doi.org/10.1016/j.jfranklin.2020.06.018.

[11] L. Fridman, J. A. Moreno, B. Bandyopadhyay, S. Kamal, and A. Chalanga, "Continuous nested algorithms: The fifth generation of sliding mode controllers," in *Recent Advances in Sliding Modes: From Control to Intelligent Mechatronics*: *Studies in Systems, Decision and Control 24*, X. Yu, and M. ÖnderEfe, Eds. Cham: Springer, 2015, pp. 5-35, https://doi.org/10.1007/978-3-319-18290-2_2.

[12] F. Shokouhi and A. H. Davaie Markazi, "A new continuous approximation of sign function for sliding mode control," in *6th International Conference on Robotics and Mechatronics (ICRoM 2018)*, Tehran, Iran, 2018.

[13] M. Navabi and M. R. Hosseini, "Investigation in to the effect of kinematic of the space craft attitude control using feedback linearization method," *Journal of Space Science and Technology*, vol. 11, no. 1, pp. 59-71, 2018.

[14] Y. Guo, B. Huang, S. M. Song, A. J. Li, and C. Q. Wang, "Robust saturated finite-time attitude control for spacecraft using integral sliding mode," *Journal of Guidance, Control, and Dynamics*, vol. 42, no. 2, pp. 440-446, 2019, https://doi.org/10.2514/1.G003520.

[15] M. Navabi and N. Safaei Hashekvaei, "Kinematic modelling without singularity and nonlinear control of satellite attitude using direct adaptive and fuzzy PD control methods," *Journal of Space Science and Technology*, vol. 14, no. 2, pp. 77-88, 2021, https://doi.org/10.22034/jsst.2021.1248.

[16] H. Yadegari, J. Beyramzad, and E. Khanmirza, "Magnetorquers-based satellite attitude control using interval type-II fuzzy terminal sliding mode control with time delay estimation," *Advances in Space Research*, vol. 69, no. 8, pp. 3204-3225, 2022, https://doi.org/10.1016/j.asr.2022.01.018.

[17] P. M. Tiwari, S. Janardhanan, and M. Nabi, "Attitude control using higher order sliding mode," *Aerospace Science and Technology*, vol. 54, pp. 108-113, 2016, https://doi.org/10.1016/j.ast.2016.04.012.

[18] M. Javaheripour, A. R. Vali, V. Behnam Gol, and F. Allahverdizadeh, "Design of an nonlinear extended state observer to estimate unmeasurable information on the problem of flying objects guidance," *Journal of Space Science and Technology*, vol. 15, no. 3, pp. 67-78, 2022, https://doi.org/10.30699/jsst.2022.1352.

[19] M. Alipour, M. Malekzadeh, and A. Ariaei, "Practical fractional-order nonsingular terminal sliding mode control of spacecraft," *ISA Transactions*, vol. 128, Part A, pp. 162-173, 2022, https://doi.org/10.1016/j.isatra.2021.10.022.

[20] Z. Ismail, R. Varatharajoo, and Y.C. Chak, "A fractional-order sliding mode control for nominal and underactuated satellite attitude controls," *Advances in Space Research*, vol. 66, no. 2, pp. 321-334, 2020, https://doi.org/10.1016/j.asr.2020.02.022.

[21] G. Zhao, "Fractional-order fast terminal sliding mode control for a class of dynamical systems," *Mathematical Problems in Engineering*, vol. 2013, no. 1, 2013, Art. no. 384921, https://doi.org/10.1155/2013/384921.

[22] C. A. Monje, Y. Q. Chen, B. M. Vinagre, D. Xue, and V. Feliu-Batlle, *Fractional-Order Systems and Controls: Fundamentals and Applications*, Springer, London, 2010.

[23] D. Xue, *Fractional-Order Control Systems: Fundamentals and Numerical Implementations*, Walter de Gruyter, 2017.

[24] V. C. Nguyen, A. T. Vo, and H. J. Kang, "A finite-time fault-tolerant control using non-singular fast terminal sliding mode control and third-order sliding mode observer for robotic manipulators," *IEEE Access*, vol. 9, pp. 31225-31235, 2021, https://doi.org/10.1109/ACCESS.2021.3059897.

[25] M. Van, H. J. Kang, Y. S. Suh, and K. S. Shin, "Output feedback tracking control of uncertain robot manipulators via higher-order sliding-mode observer and fuzzy compensator," *Journal of Mechanical Science and Technology*, vol. 27, pp. 2487-2496, 2013, https://doi.org/10.1007/s12206-013-0636-3.

[26] M. Van, P. Franciosa, and D. Ceglarek, "Fault diagnosis and fault-tolerant control of uncertain robot manipulators using high-order sliding mode," *Mathematical Problems in Engineering*, vol. 2016, no. 1, 2016, Art. no. 7926280, https://doi.org/10.1155/2016/7926280.

[27] T. M. Duc, N. V. Hoa, and T. P. Dao, "Adaptive fuzzy fractional-order nonsingular terminal sliding mode control for a class of second-order nonlinear systems," *Journal of Computational and Nonlinear Dynamics*, vol. 13, no. 3, 2018, Art. no. 31004, https://doi.org/10.1115/1.4038642.

[28] Y. Li, Y. Q. Chen, and I. Podlubny, "Mittag–Leffler stability of fractional order nonlinear dynamic systems," *Automatica*, vol. 45, no. 8, pp. 1965-1969, 2009, https://doi.org/10.1016/j.automatica.2009.04.003.

[29] D. Cao and J. Fei, "Adaptive fractional fuzzy sliding mode control for three-phase active power filter," *IEEE Access*, vol. 4, pp. 6645-6651, 2016, https://doi.org/10.1109/ACCESS.2016.2586958.

[30] A. A. Kilbas, H. M. Srivastava, and J. J. Trujillo, *Theory and Applications of Fractional Differential Equations*, 1st ed, Elsevie, 2006.

[31] G. Sun, L. Wu, Z. Kuang, Z. Ma, and J. Liu, "Practical tracking control of linear motor via fractional-order sliding mode," *Automatica*, vol. 94, pp. 221-235, 2018, https://doi.org/10.1016/j.automatica.2018.02.011.

[32] J. Fei and H. Wang, "Experimental investigation of recurrent neural network fractional-order sliding mode control of active power filter," *IEEE Transactions on Circuits and Systems II: Express Briefs*, vol. 67, no. 11, pp. 2522-2526, 2019, https://doi.org/10.1109/TCSII.2019.2953223.

[33] C. Izaguirre-Espinosa, A. J. Muñoz-Vázquez, A. Sánchez-Orta, V. Parra-Vega, and P. Castillo, "Attitude control of quadrotors based on fractional sliding modes: Theory and experiments," *IET Control Theory & Applications*, vol. 10, no. 7, pp. 825-832, 2016, https://doi.org/10.1049/iet-cta.2015.1048.

[34] H. P. Ren, X. Wang, J. T. Fan, and O. Kaynak, "Fractional order sliding mode control of a pneumatic position servo system," *Journal of the Franklin Institute*, vol. 356, no. 12, pp. 6160-6174, 2019, https://doi.org/10.1016/j.jfranklin.2019.05.024.

[35] S. Li, H. Lu, J. Li, T. Zheng, and Y. He, "Fractional-order sliding mode controller based on ESO for a buck converter with mismatched disturbances: Design and experiments," *IEEE Transactions on Industrial Electronics (Early Access)*, pp. 1-12, 2025, https://doi.org/10.1109/TIE.2024.3525110.

JSST
Journal of Space Science and Technology

P-ISSN: 2008-4560
E-ISSN: 2423-4516

Journal of Space Science and Technology

Vol. 17, Special Issue, pp. 59-65, 2024
https://doi.org/10.22034/jsst.2024.1518
Journal Homepage: https://jsstpub.com

Original Research Paper

Designing an Adaptive Velocity Obstacle Avoidance System for Autonomous Mars Rover Navigation in Dynamic Terrains

Karim Ahmadi Dastgerdi[1*], Seyedeh Marziyeh Salehi Ghahfarokhi[2], and Sadegh Ahmadi Dastgerdi [3]

1. School of Architecture, Technology and Engineering, University of Brighton, Brighton, UK
2. University of Brighton, Brighton, UK
3. Basir Andishan Bina Tadbir, Tehran, Iran

ARTICLE INFO

Article History:

Received 06 November 2024
Revised 16 December 2024
Accepted 16 December 2024
Available Online 16 December 2024

Keywords:

Adaptive cone
Autonomous navigation
Collision avoidance
Mars rover
Obstacle avoidance
Space vehicle

ABSTRACT

Over the past decade, various velocity obstacle-based methodologies have been developed for collision avoidance in dynamic environments. However, these methods are often limited to handling only a few obstacles, sequential encounters, or lack of safety guarantees in complex, unstructured terrains. This paper proposes an adaptive collision avoidance strategy using the velocity obstacle method, designed to enable autonomous Mars rovers to safely navigate dynamic and uncertain terrains while avoiding multiple obstacles simultaneously. The strategy constructs an adaptive velocity cone, accounting for dynamic obstacles and terrain features, ensuring continuous safety while guiding the rover to its waypoint. We implement the strategy in simulated Mars exploration scenarios that represent challenging multi-obstacle tasks. The simulation results demonstrate that our approach enhances performance by increasing safety distances, making it highly suitable for autonomous planetary exploration, where collision avoidance is critical for mission success.

* Corresponding Author's E-mail: k.ahmadidastgerdi@Brighton.ac.uk

How to Cite this Article:
K. Ahmadi Dastgerdi, S. M. Salehi Ghahfarokhi, and S. Ahmadi Dastgerdi, "Designing an adaptive velocity obstacle avoidance system for autonomous Mars rover navigation in dynamic terrains," *Journal of Space Science and Technology*, Vol. 17, Special Issue, pp. 59-65, 2024, https://doi.org/10.22034/jsst.2024.1518.

1. INTRODUCTION

Autonomous systems play a pivotal role in modern applications, facilitating automation and efficient operation in dynamic and uncertain environments. These systems operate through loops that govern control and decision-making processes. The inner loop focuses on implementing a controller to ensure system stability and achieve desired performance, while the outer loop is dedicated to path planning and guidance algorithms that determine feasible paths and direct the system effectively.

In recent years, control strategies for dynamic systems operating in uncertain environments have evolved significantly. These approaches, discussed in [1–3], address challenges such as external disturbances, modeling inaccuracies, and unknown conditions. In Refs. [4, 5] adaptive control strategies for satellites are developed. The controllability of dynamic systems under various uncertainties has also been extensively studied [6]. A predictive controller is for spacecraft is introduced in Ref. [7]. For outer-loop controllers, advancements have been made in optimizing path planning and guidance to enhance efficiency and robustness, as highlighted in [8,9].

Collision avoidance is a crucial aspect of autonomous Mars Rover (MR) navigation, enabling safe exploration of unstructured and challenging Martian terrains. It minimizes the risk of damage to sensitive equipment and scientific instruments, safeguards mission success, optimizes energy consumption—a critical factor for power-limited rovers—and ensures continuous data collection, maximizing the scientific value of the mission. While many studies have explored path-planning methods [10, 11], integrating collision decision-making and reactive obstacle avoidance in dynamic and uncertain environments remains relatively underexplored.

High-speed ships present a parallel case, where collision avoidance algorithms have been developed to address dynamic movement and decision-making challenges [12–14]. Insights from these maritime systems have potential applications in MR navigation, highlighting the interdisciplinary nature of the field and the transferability of advancements across domains.

For planetary navigation, methodologies addressing static and semi-dynamic obstacles have been developed [15]. Traditional methods like artificial potential fields (APFs) [16] and optimization-based techniques often struggle in multi-obstacle scenarios. APF methods, for instance, are susceptible to local minima traps and offer limited solutions constrained by predefined cost functions. Similarly, control barrier functions [17, 18] provide theoretical safety guarantees but are computationally intensive and difficult to implement for adaptive planetary navigation.

Multi-vehicle collision avoidance strategies, as demonstrated in [19–22], are typically tailored for structured environments, limiting their applicability to the unpredictable Martian landscape. Recent approaches, such as model predictive control (MPC) [23] and machine learning techniques [24], have shown promise in generating efficient collision-free paths. However, these methods rely heavily on computation and training data, posing challenges for resource-constrained Mars missions.

Reactive collision avoidance algorithms like constant bias and constant angle methods [25] are widely used in robotics and vehicle navigation but require precise tuning of avoidance angles. Improper tuning can lead to inefficiencies or unsafe maneuvers, making them less suitable for dynamic, multi-obstacle scenarios.

The velocity obstacle (VO) algorithm, commonly used in robotics, identifies unsafe velocities leading to collisions. Variants of VO have been applied successfully in underwater [26], aerial [27], and ground robotics [28]. However, conventional VO methods struggle in scenarios with multiple dynamic obstacles due to static cone formulations. Dynamic changes in velocity cone intersections during maneuvers can compromise safety and efficiency.

To address these limitations, we propose an adaptive velocity obstacle (AVO) algorithm combined with a line-of-sight (LOS) guidance law for MR navigation. The LOS guidance ensures the rover remains on course toward its target waypoint, while the AVO algorithm dynamically constructs adaptive velocity cones based on nearby obstacle motions to ensure safety. The proposed system seamlessly switches between target-reaching and collision-avoidance modes, guided by risk assessments involving metrics like the distance to the closest point of approach (DCPA) and time to the closest point of approach (TCPA).

Simulations validate the proposed method, demonstrating its superior performance in handling multi-obstacle scenario compared to existing VO approaches. The remainder of the paper introduces the MR dynamic model and reviews the conventional VO algorithm. It then presents the main results and analyzes the proposed method's performance through simulated scenarios, concluding with key findings and future research directions.

1. 1. Mars Rover Dynamics

We consider the dynamics of an MR as follows:

$$\begin{aligned} \dot{x}(t) &= v_r \cos(\psi(t)), \\ \dot{y}(t) &= v_r \sin(\psi(t)), \\ \dot{\psi}(t) &= -c\psi(t) + c\tau(t), \end{aligned} \tag{1}$$

where the states $(x, y, \psi) \in \mathbb{R}^2 \times \mathbb{S}^1$ represent the position and heading angle of the rover, and $\tau \in \mathbb{R}$ is the input steering command. The position of the rover is denoted as $p_r(t) = [x(t), y(t)]^\top$, $\psi(t)$ represents the heading angle, v_r is the constant velocity, and c is a system parameter. Let $\mathbb{R}$ denote the set of real numbers, $\mathbb{S}^1$ represent the set of real numbers modulo 2π, and $|\cdot|$ denote the Euclidean norm. The notation $\arg\min$ is used to identify the argument of the minimum value of a function. For example, for $x \in \Omega$, $\arg\min_x f(x)$ identifies the points x where $f(x)$ achieves its minimum value.

This dynamic model captures the motion of an MR traversing challenging terrains at a constant velocity. The rover's behavior is modeled as a simplified system suitable for analyzing collision avoidance and path-planning strategies. Figure 1 illustrates an example of a Mars exploration rover used in simulation studies.

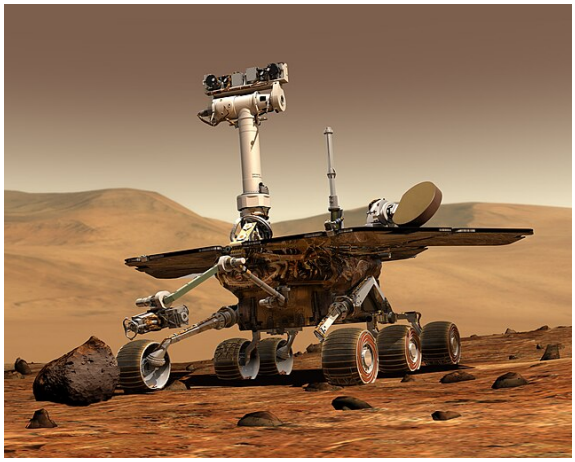

Fig. 1. Illustration of a Mars Exploration Rover.

2. VELOCITY OBSTACLE (VO) METHOD FOR COLLISION AVOIDANCE

The velocity obstacle (VO) method identifies a set of velocities that would lead to a future collision between a MR and an obstacle. By ensuring the MR's velocity remains outside this set, it can effectively avoid collisions [29]. While the obstacle can have any shape, for simplicity, it is assumed to be circular with radius R_o.

The dynamics of a moving obstacle are defined as:

$$\begin{aligned} \dot{x}_m(t) &= v_o \cos(\psi_m), \\ \dot{y}_m(t) &= v_o \sin(\psi_m), \\ \psi_m &= \gamma, \end{aligned} \tag{2}$$

where $(x_m, y_m, \psi_m) \in \mathbb{R}^2 \times \mathbb{S}^1$ represents the obstacle's position and heading, and γ is a constant heading angle. The instantaneous position of the moving obstacle is given by $p_m(t) = [x_m(t), y_m(t)]^\top$, ψ_m is its constant heading angle, and v_o is its constant velocity.

The velocity cone, which geometrically represents the collision region between the MR and a moving obstacle with radius R_o, is illustrated in Figure 2. The edges of the velocity cone are defined by the angles:

$$\psi_v = \psi_d \pm \beta, \tag{3}$$

where ψ_d is the desired heading angle towards the waypoint, and β is the avoidance angle from the obstacle. For a starboard maneuver, $\psi_v = \psi_d + \beta$, and for a port-side maneuver, $\psi_v = \psi_d - \beta$.

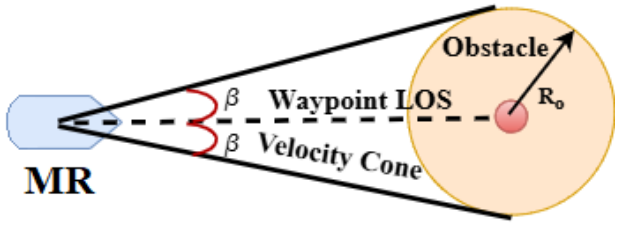

Fig. 2. Velocity cone from the MR to the obstacle.

2. 1. DCPA and TCPA Calculations ([13])

The Distance at Closest Point of Approach (DCPA) is the minimum distance between the MR and the obstacle at their Closest Point of Approach (CPA). The Time to Closest Point of Approach (TCPA) is the time taken for either the MR or the obstacle to reach this CPA, where they are at their minimum distance from each other.

Mathematically, the DCPA and TCPA are given as:

$$\text{DCPA} = \|D\| \sin(\phi), \tag{4}$$

$$\text{TCPA} = \frac{v_r^\top D}{\|v_r\|^2 |\cos(\phi)|}, \tag{5}$$

where:

- $\phi = \cos^{-1}\left(\frac{v_r^\top D}{\|v_r\| \|D\|}\right)$,

- $v_r = [\dot{x} - \dot{x}_m, \dot{y} - \dot{y}_m]^\top$ is the relative velocity,
- $D = [x - x_m, y - y_m]^\top$ is the relative position vector.

3. ADAPTIVE VELOCITY OBSTACLE AVOIDANCE

The Adaptive Velocity Obstacle (AVO) collision avoidance method is integrated with the Line of Sight (LOS) based goal-reaching guidance law. Consequently, the control system for the MR operates in two modes: 1) Target Reaching Mode and 2) Collision Avoidance Mode. The transitions between these modes are determined by decision-making processes based on risk assessment, as discussed in Section **3. 3.** We assume that a sequence of waypoints is provided by the mission planner.

3. 1. Target Reaching Mode

In this subsection, the guidance law for waypoint reaching is described.

Target Reaching Guidance Law

To reach the waypoint $p_t := (x_t, y_t)$, we define the desired guidance law (heading angle) for equation (3) as:

$$\psi_d(t) = \text{atan2}\left((y_t - y), (x_t - x)\right). \tag{6}$$

We define the heading track error as $e(t) = \psi(t) - \psi_d(t)$. Thus, the error dynamics become:

$$\dot{e}(t) = -c\psi(t) + c\tau(t) - \dot{\psi}_d(t). \tag{7}$$

We propose the control law:

$$\tau(t) = \frac{1}{c}\dot{\psi}_d(t) + \psi_d(t), \tag{8}$$

to ensure the asymptotic stability of the heading track error dynamics (7).

3. 2. Obstacle Avoidance Mode

In this mode, the MR avoids multiple dynamic obstacles as follows.

We consider M dynamic obstacles, where the i-th obstacle is represented by the obstacle dynamics in equation (2), with subscripts such as $(x_{mi}, y_{mi}, \psi_{mi}, p_{mi})$ for $i = 1, \ldots, M$. The minimum allowable distance around the obstacle p_{mi} is denoted as C_s, representing the smallest acceptable bound on the DCPA.

We observe that there always exists a change of variables that aligns the waypoint LOS with the x-axis. We now define a criterion for constructing a circle $C(t)$, shown in Figure 3, as follows. Initially, we assume that the circle $C(t)$ with radius $R(t)$ encompasses all dynamic obstacles.

(1) Compute $d_{mi}(t) = \|p_s(t) - p_{mi}(t)\|$. If $d_{mi}(t) < d_{safe} = C_s$, the i-th obstacle $p_{mi}(t)$ is inside $C(t)$;
(2) Compute $d_{mij}(t) = \|p_{mi}(t) - p_{mj}(t)\|, i \neq j$. If $d_{mij}(t) \leq 2d_{safe}$, the j-th obstacle $p_{mj}(t)$ is inside $C(t)$;
(3) Calculate $(TCPA_k, CPA_k)$ according to equation (4) for all $k = 1, \ldots, M$. If $\|p_s(t) - CPA_k\| < d_{safe}$, the k-th obstacle $p_{mk}(t)$ is inside $C(t)$;
(4) If the minimum k exists such that $\|p_s(t) - CPA_k\|$ is minimized at $(CPA_d, TCPA_d)$, compute the new future position of the k-th obstacle $p_{mkl} : (x_{mk}(TCPA_d), y_{mk}(TCPA_d))$ at $TCPA_d$. If $\|p_s(t) - p_{mkl}\| < d_{safe}$, then the l-th obstacle $p_{ml}(t)$ is inside $C(t)$.

After these steps, if there are Q obstacles inside the circle $C(t)$, the radius $R(t)$ is given by:

$$R(t) = \max\{W(t), H(t)\},$$

where $H(t) = \max\{|y_{mq}(t)|\} + C_s$, and $W(t) = \max\{|x_{mq}(t) - x_{mc}(t)|\} + C_s$, with $q = 1, \ldots, Q$, and $p_{mc}(t) : (x_{mc}(t), y_{mc}(t))$ is the CPA_d of the q-th obstacle at which $\arg\min_{k=1,\ldots,M} \|p_s(t) - CPA_q\|$ exists.

In Figure 3, we consider $Q = 3$, and obstacle 3's CPA, $p_{m3c}(t)$, has the minimum distance to the MR $p_s(t)$. Therefore, $p_{m3c}(t) : (x_{m3c}(t), y_{m3c}(t))$ is CPA_d, with $H(t) = |y_{m2}(t)| + C_s$, $W(t) = |x_{m1}(t) - x_{m3c}(t)| + C_s$, and $d_s(t) = \|p_s(t) - p_{m3c}(t)\|$ being the distance between $p_{m3c}(t)$ and the MR $p_s(t)$. The radius of the circle is $R(t) = \max\{W(t), H(t)\}$.

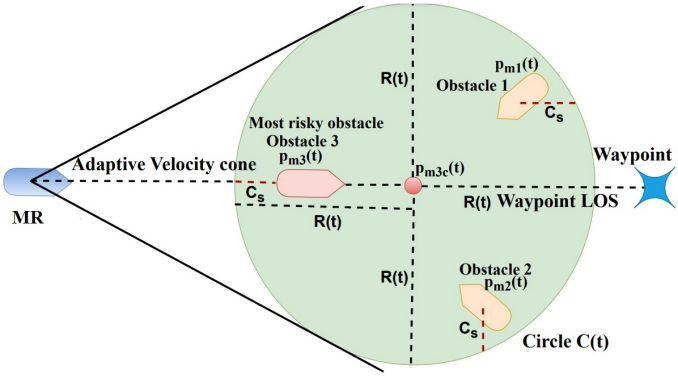

Fig. 3. Illustration of the adaptive velocity cone with multiple obstacles present.

Once the construction of circle $C(t)$ is complete, the desired heading angle to avoid multiple obstacles is

calculated from the edges of the circle as follows.

Obstacle Avoidance Guidance Law

To avoid multiple dynamic obstacles, the desired guidance law (heading angle) for equation (3) is defined as:

$$\psi_{dc}(t) = \text{atan2}\left((y_t - y),(x_t - x)\right) \pm \text{atan2}\left(R(t), d_s(t)\right). \tag{9}$$

We define the heading track error as $e(t) = \psi(t) - \psi_{dc}(t)$. Thus, the error dynamics become:

$$\dot{e}(t) = -c\psi(t) + c\tau(t) - \dot{\psi}_{dc}(t). \tag{10}$$

We propose the control law:

$$\tau(t) = \frac{1}{c}\dot{\psi}_{dc}(t) + \psi_{dc}(t),$$

to ensure the asymptotic stability of the heading track error dynamics (10).

3. 3. Decision Making Based on Risk Assessment

The control switches from target-reaching mode to obstacle avoidance mode if both of the following conditions are satisfied:

1. The waypoint LOS intersects with the adaptive velocity cone, causing the obstruction flag to be raised to one.
2. The risk index (RI) flag is one. The flag of the risk index (RI_{Flag}) is determined as:

$$\text{RI}_{\text{Flag}} = \begin{cases} 0, & \text{if RI} < C_{\text{t}}, \\ 1, & \text{if RI} \geq C_{\text{t}}. \end{cases} \tag{11}$$

where the risk index RI for DCPA, TCPA, and obstacle distance $\|D\|$ is defined as:

$$\text{RI} = \frac{1}{3}\left(F(\text{DCPA}) + F(\text{TCPA}) + F(\|\text{D}\|)\right), \tag{12}$$

with C_t being the threshold value of the risk index, and $F(\cdot)$ as defined in equation (13).

$$F(\zeta) = \begin{cases} 1, & \zeta \in [0, d_1], \\ 1 - 2\left(\frac{\zeta - d_1}{d_2 - d_1}\right)^2, & \zeta \in (d_1, \frac{d_1+d_2}{2}], \\ 2\left(\frac{\zeta - d_2}{d_2 - d_1}\right)^2, & \zeta \in (\frac{d_1+d_2}{2}, d_2], \\ 0, & \zeta \in (d_2, \infty). \end{cases} \tag{13}$$

where ζ represents DCPA, TCPA, or obstacle distance ($\|D\|$), and d_1, d_2 are tuning parameters for these metrics.

We define an additional flag called the "collision avoidance flag" (C_{Flag}). If the vehicle reaches the target, the mode switches to target-reaching mode and the collision avoidance mode is temporarily halted. We describe the switching logic as follows:

$$\text{C}_{\text{Flag}} = \begin{cases} 0, & \text{if no collision is detected}, \\ 1, & \text{if collision is detected}. \end{cases} \tag{14}$$

4. RESULTS AND DISCUSSION

In this section, we provide an overview of the simulation outcomes resulting from the implementation of the proposed algorithm in complex scenarios.

For the scenario, the MR begins at the coordinates $p_s(0) = [0,0]^\top$, with an initial heading angle of zero degrees ($\psi(0) = 0^\circ$) and a velocity $v_s = 0.16$ kilometers per hour. The designated waypoint is located at $p_t = (50,0)$ meter (m), and the velocity of all three dynamic obstacles is $v_o = 0.1$ kilometers per hour. The risk assessment parameters are set as follows: $C_{\text{t}} = 0.35$, DCPA $\in [10,25]$ meter, TCPA $\in [2,4]$ minutes, and obstacle distance $\|D\| \in [10,25]$ m.

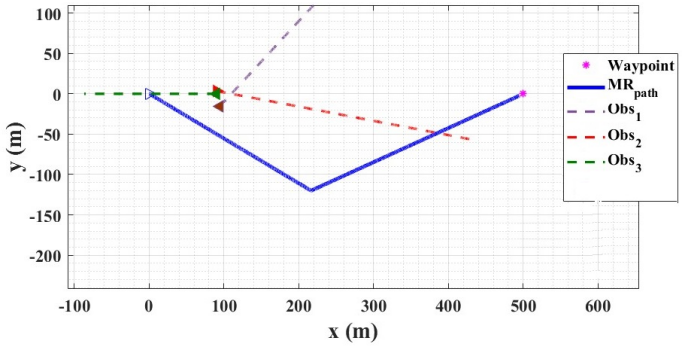

Fig. 4. Path of the MR and three dynamic obstacles.

4. 1. Discussion

Figure 4 illustrates the MR's trajectory for a specific scenario, using the proposed AVO algorithms. The results show that the MR successfully reaches the waypoint. Figure 5 provides the distances between the MR and obstacles using AVO methods. It is evident that the AVO algorithm successfully navigates the MR to the waypoint while avoiding all three obstacles.

Finally, Figure 6 shows the MR's heading angle and the corresponding control commands. These results demonstrate the effectiveness of the proposed algorithm in space vechicels collision avoidance.

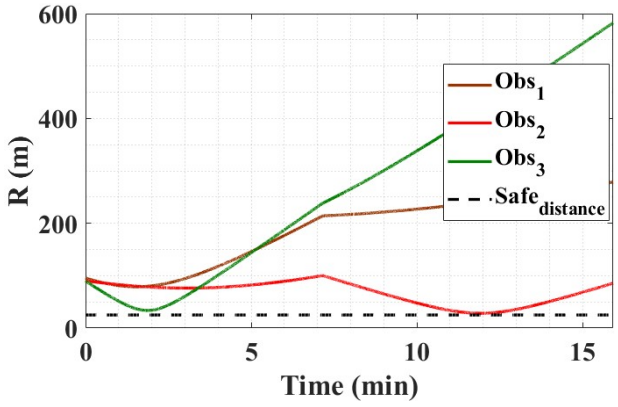

Fig. 5. Obstacles' distance.

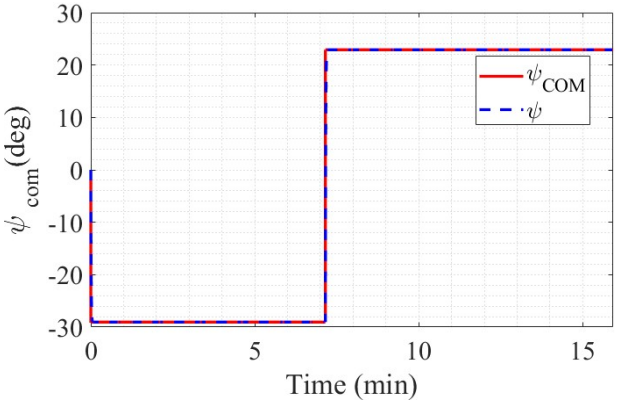

Fig. 6. MR heading angle and control command.

5. CONCLUSION

In this paper, we presented an adaptive velocity obstacle algorithm combined with a LOS guidance law for safe multi-vessel encounters while reaching a waypoint. We constructed an adaptive velocity cone from the MR to the unsafe set (circle) of multiple dynamic obstacles, utilizing the time to closest point of approach (TCPA) and distance to closest point of approach (DCPA) of each obstacle relative to the Mars rover. Future research will focus on extending the algorithm to account for MR and obstacle dynamics under disturbances and uncertainties, as well as formally characterizing the conditions under which the proposed method can be considered probabilistically safe.

CONFLICT OF INTERESTS

No conflict of interest has been expressed by the authors.

REFERENCES

[1] K. Ahmadi, D. Asadi, A. Merheb, S. Y. Nabavi-Chashmi, and O. Tutsoy, "Active fault-tolerant control of quadrotor UAVs with nonlinear observer-based sliding mode control validated through hardware in the loop experiments," *Control Engineering Practice*, vol. 137, 2023, Art. no. 105557, https://doi.org/10.1016/j.conengprac.2023.105557.

[2] K. Ahmadi, D. Asadi, S. Y. Nabavi-Chashmi, and O. Tutsoy, "Modified adaptive discrete-time incremental nonlinear dynamic inversion control for quad-rotors in the presence of motor faults," *Mechanical Systems and Signal Processing*, vol. 188, 2023, Art. no. 109989, https://doi.org/10.1016/j.ymssp.2022.109989.

[3] K. Ahmadi Dastgerdi, F. Pazooki, and J. Roshanian, "Model reference adaptive control of a small satellite in the presence of parameter uncertainties," *Scientia Iranica*, vol. 27, no. 6, pp. 2933-2944, 2020, (in Persian), https://doi.org/10.24200/sci.2019.50455.1704.

[4] M. Navabi and H. Ghanbari, "Attitude control of spacecraft using L1 Aadaptive control in the presence of actuator and disturbances," *Journal of Space Science and Technology*, vol. 13, no. 2, pp. 79-86, 2020, (in Persian), https://doi.org/10.30699/jsst.2020.2110.

[5] M. Navabi and N. Safaei Hashekvaei, "Kinematic modelling without singularity and nonlinear control of satellite attitude using direct adaptive and fuzzy PD control methods," *Journal of Space Science and Technology*, vol. 14, no. 2, pp. 77-88, 2021, (in Persian), https://doi.org/10.22034/jsst.2021.1248.

[6] D. Asadi, K. Ahmadi, S.Y. Nabavi Chashmi, and O. Tutsoy, "Controlability of multi-rotors under motor fault effect," *Artibilim: Adana Alparslan Turkes Bilim ve Teknoloji Universitesi Fen Bilimleri Dergisi*, vol. 4, no. 2, pp. 24-43, 2021.

[7] M. Navabi and P. Zarei, "Attitude nonlinear predictive control of an under actuated spacecraft," *Journal of Space Science and Technology*, vol. 14, no. 4, pp. 77-83, 2021, (in Persian), https://doi.org/10.22034/jsst.2021.1304.

[8] K. A. Dastgerdi, B. Singh, W. Naeem, and N. Athanasopoulos, "Adaptive velocity obstacle avoidance for multi-vessel encounters," in *UKACC 14th International Conference on Control (CONTROL)*, Winchester, United Kingdom, 2024, pp. 90-95, https://doi.org/10.1109/CONTROL60310.2024.10532047.

[9] S. Y. Nabavi Chashmi, D. Asadi, and K. Ahmadi Dastgerdi, "Safe land system architecture design of multi-rotors considering engine failure," *International Journal of Aeronautics and Astronautics*, vol. 3, no. 1, pp. 7-19, 2022, https://doi.org/10.55212/ijaa.1032693.

[10] T. I. Fossen and K. Y. Pettersen, "On uniform semiglobal exponential stability (USGES) of proportional line-of-sight guidance laws,"

Automatica, vol. 50, no. 11, pp. 2912-2917, 2014, https://doi.org/10.1016/j.automatica.2014.10.018.

[11] R. Polvara, S. Sharma, J. Wan, A. Manning, and R. Sutton, "Obstacle avoidance approaches for autonomous navigation of unmanned surface vehicles," *Journal of Navigation*, vol. 71, no. 1, pp. 241-256, 2018, https://doi.org/10.1017/S0373463317000753.

[12] K. A. Dastgerdi, B. Singh, W. Naeem, N. Athanasopoulos, and B. Lecallard, "Uncertainty aware path planning and collision avoidance for marine vehicles," *IFAC-PapersOnLine*, vol. 58, no. 20, pp. 235-240, 2024, https://doi.org/10.1016/j.ifacol.2024.10.060.

[13] K. A. Dastgerdi, B. Singh, N. Athanasopoulos, W. Naeem, and B. Lecallard, "Geometric path planning for high speed marine craft," *IFAC-PapersOnLine*, vol. 56, no. 2, pp. 5729-5734, 2023, https://doi.org/10.1016/j.ifacol.2023.10.525.

[14] P. Sarhadi, W. Naeem, and N. Athanasopoulos, "An integrated risk assessment and collision avoidance methodology for an autonomous catamaran with fuzzy weighting functions," in *UKACC 13th International Conference on Control (CONTROL)*, Plymouth, United Kingdom, 2022, pp. 228-234, https://doi.org/10.1109/Control55989.2022.9781453.

[15] Z. Liu, Y. Zhang, X. Yu, and C. Yuan, "Unmanned surface vehicles: An overview of developments and challenges," *Annual Reviews in Control*, vol. 41, pp. 71-93, 2016, https://doi.org/10.1016/j.arcontrol.2016.04.018.

[16] Z. Zhu, Y. Yin, and H. Lyu, "Automatic collision avoidance algorithm based on route-plan-guided artificial potential field method," *Ocean Engineering*, vol. 271, 2023, Art. no. 113737, https://doi.org/10.1016/j.oceaneng.2023.113737.

[17] M. Srinivasan and S. Coogan, "Control of mobile robots using barrier functions under temporal logic specifications," *IEEE Transactions on Robotics*, vol. 37, no. 2, pp. 363-374, 2021, https://doi.org/10.1109/TRO.2020.3031254.

[18] A. Singletary, K. Klingebiel, J. Bourne, A. Browning, P. Tokumaru, and A. Ames, "Comparative analysis of control barrier functions and artificial potential fields for obstacle avoidance," in *International Conference on Intelligent Robots and Systems (IROS)*, Prague, Czech Republic, 2021, pp. 8129-8136, https://doi.org/10.1109/IROS51168.2021.9636670.

[19] M. Hoy, A. S. Matveev, and A. V. Savkin, "Algorithms for collision-free navigation of mobile robots in complex cluttered environments: A survey," *Robotica*, vol. 33, no. 3, pp. 463-497, 2015, https://doi.org/10.1017/S0263574714000289.

[20] K. D. Do, "Synchronization motion tracking control of multiple underactuated ships with collision avoidance," *IEEE Transactions on Industrial Electronics*, vol. 63, no. 5, pp. 2976-2989, 2016, https://doi.org/10.1109/TIE.2016.2523453.

[21] M. Kamel, J. Alonso Mora, R. Siegwart, and J. Nieto, "Robust collision avoidance for multiple micro aerial vehicles using nonlinear model predictive control," in *International Conference on Intelligent Robots and Systems (IROS)*, Vancouver, BC, Canada, 2017, pp. 236-243, https://doi.org/10.1109/IROS.2017.8202163.

[22] Y. T. Kang, W. J. Chen, D. Q. Zhu, and J. H. Wang, "Collision avoidance path planning in multi-ship encounter situations," *Journal of Marine Science and Technology*, vol. 26, 1026-1037, 2021, https://doi.org/10.1007/s00773-021-00796-z.

[23] Z. Du, V. Reppa, and R. R. Negenborn, "MPC-based COLREGS compliant collision avoidance for a multi-vessel ship-towing system," in *European Control Conference (ECC)*, Delft, Netherlands, 2021, pp. 1857-1862, https://doi.org/10.23919/ECC54610.2021.9655091.

[24] P. Sarhadi, W. Naeem, and N. Athanasopoulos, "A survey of recent machine learning solutions for ship collision avoidance and mission planning," *IFAC-PapersOnLine*, vol. 55, no. 31, pp. 257-268, 2022, https://doi.org/10.1016/j.ifacol.2022.10.440.

[25] S. Campbell, W. Naeem, and G. W. Irwin, "A review on improving the autonomy of unmanned surface vehicles through intelligent collision avoidance manoeuvres," *Annual Reviews in Control*, vol. 36, no. 2, pp. 267-283, 2012, https://doi.org/10.1016/j.arcontrol.2012.09.008.

[26] W. Zhang, S. Wei, Y. Teng, J. Zhang, X. Wang, and Z. Yan, "Dynamic obstacle avoidance for unmanned underwater vehicles based on an improved velocity obstacle method," *Sensors*, vol. 17, no. 12, 2017, Art. no. 2742, https://doi.org/10.3390/s17122742.

[27] G. A. Mercado Velasco, C. Borst, J. Ellerbroek, M. M. van Paassen, and M. Mulder, "The use of intent information in conflict detection and resolution models based on dynamic velocity obstacles," *IEEE Transactions on Intelligent Transportation Systems*, vol. 16, no. 4, pp. 2297-2302, 2015, https://doi.org/10.1109/TITS.2014.2376031.

[28] Z. Gyenes and E. G. Szadeczky Kardoss, "Motion planning for mobile robots using the safety velocity obstacles method," in *19th International Carpathian Control Conference (ICCC)*, Szilvasvarad, Hungary, 2018, pp. 389-394, https://doi.org/10.1109/CarpathianCC.2018.8473397.

[29] P. Fiorini and Z. Shiller, "Motion planning in dynamic environments using velocity obstacles," *International Journal of Robotics Research*, vol. 17, no. 7, pp. 760-772, 1998, https://doi.org/10.1177/027836499801700706.